# Interactions and Collective Behavior of Attractive Colloidal Rods and Microspheres Grafted with Filamentous Bacteriophage

A Dissertation

Presented to

The Faculty of the Graduate School of Arts and Sciences

Brandeis University

Department of Physics

Dr. Seth Fraden, Advisor

In Partial Fulfillment

of the Requirements for the Degree

Doctor of Philosophy

by

Fei Huang

May, 2009

This dissertation, directed and approved by Fei Huang's committee, has been accepted and approved by the Graduate Faculty of Brandeis University in partial fulfillment of the requirements for the degree of:

**DOCTOR OF PHILOSOPHY**

Adam B. Jaffe, Dean of Arts and Sciences

Dissertation Committee:

Dr. Seth Fraden, Chair

Dr. Michael Hagan

Dr. Nolan T. Flynn

# Acknowledgments

Many people have given me a great deal of help during the course of my study at Brandeis. First and foremost, I am grateful to Prof. Seth Fraden for his support and guidance both as a friend and as a mentor. I admire his enthusiasm about science, his keen ability to quickly dissect problems and point me in the right direction, and his candor about my weaknesses.

I would like to thank my collaborators, particularly Prof. Zvonimir Dogic, Prof. Michael Hagan and Prof. Nolan Flynn, from whom I have learned tremendously. My sincere thanks also go to many colleagues in and outside the physics department: Dr. Kirstin Purdy for introducing me to fd virus and the initial development of M13-C7C phage; Dr. Feng Wang and Dr. Larry Friedman from the Gelles lab for teaching me all the tricks of biochemical synthesis; Andrew Ward and Karim Addas for building and maintaining the optical tweezers; Dr. Hector Gonzalez and Dr. Yanwei Jia for their genuine advices when I was in doubt; Edward Barry, Seila Selimovic and Roy Rotstein for numerous stimulating and enjoyable discussions.

I wish to express my deep gratitude to my friends here in the U.S. and family on the other side of the ocean, for all their patience and unconditional support.

# Abstract

## Interactions and Collective Behavior of Attractive Colloidal Rods and Microspheres Grafted with Filamentous Bacteriophage

A dissertation presented to the Faculty of
the Graduate School of Arts and Sciences of
Brandeis University, Waltham, Massachusetts

by Fei Huang

Interactions and collective behavior are investigated for two systems of attractive colloidal rods and colloidal stars. Attractive colloidal rods are constructed by grafting the temperature-sensitive polymer poly(N-isopropylacrylamide) (PNIPAM) to the surface of the semi-flexible filamentous fd virus. The phase diagram of fd-PNIPAM system becomes independent of ionic strength at high salt concentration and low temperature, i.e., the rods are sterically stabilized by the polymer. However, the network of rods undergoes a sol-gel transition as the temperature is raised. The viscoelastic moduli of fd and fd-PNIPAM suspensions are compared as a function of temperature, and the effect of ionic strength on the gelling behavior of fd-PNIPAM solution is measured. For all fluidlike and solidlike samples, the frequency-dependant linear viscoelastic moduli can be scaled onto universal master curves.

Colloidal stars are constructed by grafting to 1 $\mu$m polystyrene beads a dense brush of 1 $\mu$m long and 10 nm wide semi-flexible filamentous viruses. The pair interaction potentials of colloidal stars are measured using an experimental implementation of umbrella sampling, a technique originally developed in computer simulations in order to probe rare events. The influence of ionic strength and grafting density on the interaction is measured. Good agreements are found between the measured interactions and theoretical predictions based upon the osmotic pressure of counterions.

This thesis is partially based on the following publications:

- F. Huang, R. Rotstein, K. E. Kasza, N. T. Flynn and S. Fraden. Phase behavior and rheology of attractive rod-like particles. *Soft Matter*, DOI:10.1039/b823522h - Chapter 2.

- F. Huang, K. Addas, A. Ward, N. T. Flynn, E. Velasco, M. F. Hagan, Z. Dogic, and S. Fraden. Pair Potential of Charged Colloidal Stars. *Phys. Rev. Lett.*, **102**, 108302 (2009) - Chapter 3.

- F. Huang, S. Lin, N. Ribeck, and S. Fraden. Electric-field-induced chaining of colloidal particles. In preparation. - Chapter 5.

# Contents

# List of Figures

# Chapter 1

# Introduction

## 1.1 Outline

The main purpose of the work described in this thesis is to construct novel hybrid colloids and elucidate the nature of the engineered interactions as well as the collective behavior of these particles.

In the Section 1.2.1, we describe the Onsager theory for the isotropic-nematic phase transition of hard rodlike particles. In the Section 1.3, we introduce our primary experimental system of bacteriophage fd and M13. We demonstrate that the rodlike phage particle can be functionalized on only one end through phage display.

In Chapter 2 we investigate the effect of attraction on the phase behavior and rheology of colloidal rod-like particles. Colloidal "sticky" rods are synthsized by grafting the temperature-sensitive polymer poly(N-isopropylacrylamide) (PNIPAM) to the surface of the semi-flexible filamentous fd virus. Theory predicts the addition of attractive interaction enhances the isotropic-nematic phase separation by widening the $I$-$N$ coexistence. In our experiment with PNIPAM-coated fd rods, however, a sol-gel transition is observed. We attribute this result to the kinetic arrest of attractive

rods, which have not reached their thermodynamic equilibrium. We quantitatively characterize the gelation with rheology, and found that the suspension of PNIPAM-coated fd is rheologically similar to simple polymeric melts. This observation led us to believe the contacts between the colloidal rods are essentially identical to those in a polymer melt.

Chapter 3 describes the construction of colloidal stars from micro-sized polystyrene beads and genetically engineered filamentous viruses. We develop a new experimental protocol based on the computer simulation method known as umbrella sampling to extract the pair interaction potentials of colloidal stars. The new method enables one to measure potentials of the order of hundreds of $k_{\mathrm{B}}T$, an energy much greater than previously measured with other techniques, e.g. line tweezers. The measured interactions between pairs of stars are all purely repulsive, in good agreements with theoretical model based upon the osmotic pressure of counterions.

Chapter 4 reports on the failed attempts on synthesizing rod-coil particle. Streptavidin-coated polystyrene beads and plasmid DNA are respectively utilized to make rod-coil by grafting to genetically engineered M13 virus. Explanations for why reactions don't work are given. A new scheme of synthesis is proposed at the end.

Chapter 5 continues the study of the influence of attraction, now on dilute suspensions of micron-sized polystyrene (PS) spheres. Linear chains of PS spheres form when high frequency AC electric fields are applied to the solution. The E-field induces dipole-dipole attraction between the spheres while the Coulumbic repulsion acts to keep them apart. Digital video microscopy reals the kinetics of chain formation and the thermo-equilibrium between chains. The chain length distribution in equilibrium is measured as well as modeled by a statistical theory based on the law of mass action. A Langevin dynamics simulation further verifies the experimental and theoretical results.

An appendix is included detailing the protocols for the production of the bacteriophage used in the above experiments .

## 1.2 Theoretical Background

### 1.2.1 The Onsager virial expansion of the free energy

Solutions of rodlike particles undergo a transition from an isotropic phase to an anisotropic phase above a critical concentration. To describe this phase transition Onsager developed a microscopic theory based on the second virial expansion of the free energy [61]. The excess Helmholtz free energy for a dilute suspension of rods can be written in the form

$$\begin{aligned} \frac{\Delta F}{N k_{\mathrm{B}} T} &= \frac{F(\text{solution}) - F(\text{solvent})}{N k_{\mathrm{B}} T} \\ &= \frac{\mu_0}{k_{\mathrm{B}} T} - 1 + \ln c + \sigma(f) + bc\rho(f) \end{aligned} \tag{1.1}$$

Here $\mu_0$ and $c$ are the standard chemical potential and the number concentration of the solute respectively. $\sigma$ is the orientational entropy term, minimized by an isotropic distribution function.

$$\sigma = \int f(\mathbf{\Omega}) \ln(4\pi f(\mathbf{\Omega})) d\mathbf{\Omega} \tag{1.2}$$

Where $f(\mathbf{\Omega})$ is the orientational distribution function with the normalization

$$\int f(\mathbf{\Omega}) d\mathbf{\Omega} = 1 \tag{1.3}$$

The last term of Eq. (1.1), $bc\rho(f)$, represents the entropy of packing, which is mini-

mized by a perfectly aligned configuration.

$$b\rho(f) = -\frac{1}{2}\beta_1\rho(f) = -\frac{1}{2}\int\int \beta_1(\mathbf{\Omega},\mathbf{\Omega}')f(\mathbf{\Omega})f(\mathbf{\Omega}')d\mathbf{\Omega}d\mathbf{\Omega}' \tag{1.4}$$

Where $b = -\frac{1}{2}\beta_1$ is the second virial coefficient, and $-\beta_1 = -\frac{1}{V}\int(e^{-w_{12}/k_\mathrm{B}T}-1)d\mathbf{r_1}d\mathbf{r_2}$ corresponds to the volume denied to particle 2 by the presence of particle 1. For a pair of spherical particles of radius r, the excluded volume is simply a sphere of radius 2r, or 8 times the volume of one particle. For long rods with high aspect ratios ($L \gg D$) and an angle $\gamma$ between their axes, the excluded volume is

$$-\beta_1 = 2L^2D\sin\gamma \tag{1.5}$$

Then we obtain

$$\frac{\Delta F}{Nk_\mathrm{B}T} = \frac{\mu_0}{k_\mathrm{B}T} - 1 + \ln c + \int f(\mathbf{\Omega})\ln(4\pi f(\mathbf{\Omega}))d\mathbf{\Omega} + cL^2D\int\int(\sin\gamma)f(\mathbf{\Omega})f(\mathbf{\Omega}')d\mathbf{\Omega}d\mathbf{\Omega} \tag{1.6}$$

The above free energy functional, a function of a function, needs to be minimized to find the orientational distribution function $f(\mathbf{\Omega})$. This is achieved by assuming a trial function for $f(\mathbf{\Omega})$ and minimize the free energy with respect to a free parameter in the guessed distribution function. A convenient trial function is

$$f(\theta) = \frac{\alpha}{4\pi}\frac{\cosh(\alpha\cos(\theta))}{\sinh\alpha} \tag{1.7}$$

From the free energy, we can derive the osmotic pressure $\Pi = (-\frac{\partial F}{\partial V})_{N,T}$ and the chemical potential $\mu = (\frac{\partial F}{\partial N})_{V,T}$. Furthermore, the concentrations for the coexisting isotropic and nematic phases can be calculated by the following equilibrium conditions

$$\Pi_n = \Pi_i \tag{1.8}$$

$$\mu_n = \mu_i \tag{1.9}$$

which correspond to

$$c_n + bc_n^2\rho = c_i + bc_i^2 \tag{1.10}$$
$$\ln c_n + \sigma + 2bc_n\rho = \ln c_i + 2bc_i \tag{1.11}$$

Finally the coexisting concentrations are

$$bc_i = 3.340, \qquad bc_a = 4.486 \tag{1.12}$$

**The effect of charge on rod-like particles**

The electrostatic interaction between two rod-like polyelectrolytes can be written approximately in the form [61, 68]

$$\frac{w}{k_{\mathrm{B}}T} = \frac{Ae^{-\kappa x}}{\sin\gamma} \tag{1.13}$$

Where $x$ is the shortest distance between the center lines of the polyion cylinders, $\kappa^{-1}$ is the Debye screening length and $\gamma$ is the angle between the rods. Onsager demonstrated the effect of charge on a rod-like particle can be modelled as an increase of its excluded volume. The effective diameter of the particle is introduced as a function of charge.

$$D_{\mathrm{eff}} = D(1 + \frac{\ln A' + C + \ln 2 - 1/2}{\kappa D}) \tag{1.14}$$

Here $A' = Ae^{-\kappa D}$ and $C = 0.577215665...$ denotes Euler's constant. Thus the free energy in the isotropic phase can be expressed as

$$\frac{\Delta F}{Nk_{\mathrm{B}}T} = \frac{\mu_0}{k_{\mathrm{B}}T} - 1 + \ln c + \frac{\pi}{4}L^2 D_{\mathrm{eff}} \cdot c \tag{1.15}$$

As can be seen from Eq. 1.13, the charged rods have a lower energy when their axes are perpendicular rather than parallel. This twist effect is accounted for explicitly in the free energy for the nematic phase by having an additional term, which scales as $h = \kappa^{-1}/D_{\text{eff}}$, the ratio of the Debye screening length and the effective diameter [76].

$$\frac{\Delta F}{N k_{\text{B}} T} = \frac{\mu_0}{k_{\text{B}} T} - 1 + \ln c + \sigma + \frac{\pi}{4} L^2 D_{\text{eff}} \cdot c \cdot (\rho(f) + h\eta(f)) \tag{1.16}$$

Where

$$\sigma = \langle \ln(4\pi f) \rangle_{nem} \tag{1.17}$$

$$\rho(f) = \frac{4}{\pi} \langle \langle \sin\gamma \rangle \rangle_{nem} \tag{1.18}$$

$$\eta(f) = \frac{4}{\pi} \langle \langle -\sin\gamma \ln(\sin\gamma) \rangle \rangle_{nem} - [\ln 2 - 1/2]\rho(f) \tag{1.19}$$

## 1.3 Genetically Engineered M13-C7C Phages as Building Blocks for Hybrid Materials

Filamentous bacteriophage fd and M13 are rodlike semiflexible charged polymers of length $L = 880$ nm, diameter $D = 6.6$ nm, molecular weight $1.64 \times 10^7$ dalton, and surface charge density $7e^-$/nm at $p$H $= 8.2$. The phage genome of a single-stranded DNA resides in a cylindrical capsid consisting of approximately 2700 copies of major coat pVIII proteins, about 5 copies each of minor coat pIII and pVI proteins at the infective end of the bacteriophage, and about 5 copies each of minor coat pVII and pIX proteins at the other end.

Controlled modification of the M13 capsid protein is achieved through making use of the Ph.D.-C7C Phage Display Peptide Library (New England Biolabs, Beverly, MA), a combinatorial library of random 7-mers flanked by a a pair of cysteine residues

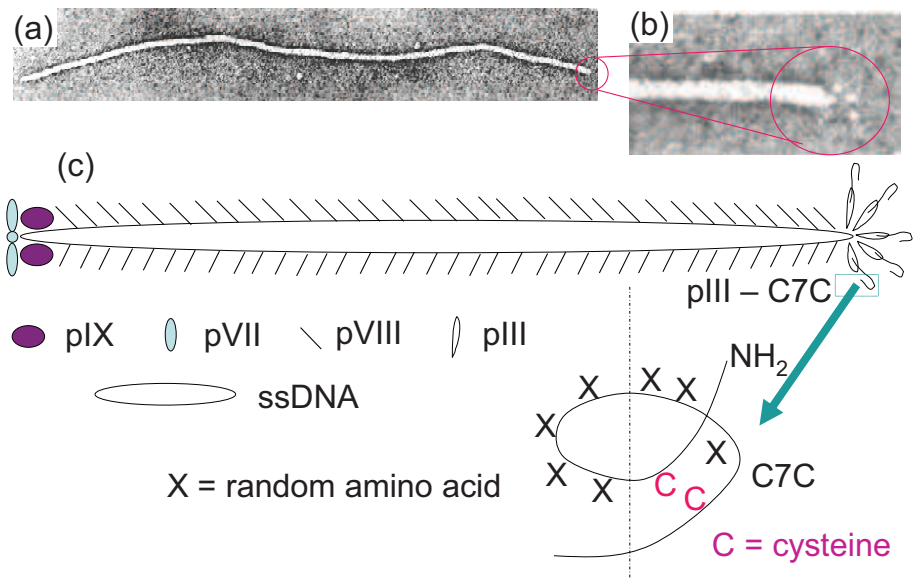


Figure 1.1: (a) Electron micrograph of M13 virus. (b) Five copies of PIII proteins uniquely located on one end. (c) Schematic of M13-C7C, which has a pair of cysteines displayed on the N-terminus end of protein PIII.

fused to the N-terminus of a minor coat protein (pIII) of M13 phage (M13-C7C). Under nonreducing condition the cysteines spontaneously form a disulfide bridge, resulting in phage display of cyclized peptides. Although M13-C7C phage shares nearly the same physical characteristics with wild-type M13 phages, altering the pIII proteins allows for the creation of unique binding sites on only one end of the phage.

M13-C7C bacteriophage is grown and purified as described in appendix A. To ensure the presence of the peptide inserts (Ala-Cys-Xxx-Xxx-Xxx-Xxx-Xxx-Xxx-Xxx-Cys-Gly-Gly-Gly-Ser), the resulting phages are DNA sequenced after amplification. Concentrations of phage particles were measured using absorption spectrophotometry. The optical density of M13 is $A_{269\,\mathrm{nm}}^{1\,\mathrm{mg/ml}} = 3.84$ for a path length of 1 cm.

# Chapter 2

# Phase Behavior and Rheology of Attractive Rod-Like Particles

## 2.1 Introduction

The phase behavior of a fluid of rod-like particles interacting through short range repulsion has been well described at the second virial coefficient level by Onsager [61] who demonstrated that this system exhibits an isotropic-nematic ($I$-$N$) phase transition. Examples of colloidal liquid crystals range from minerals [15] to viruses [18], with theory agreeing with experimental results in many cases. Attempts have been made to explore the influence of attractive interactions on the $I$-$N$ transition both theoretically and experimentally. One approach to introduce attractions has been through "depletion attraction" [3] in which rods and polymers are mixed resulting in an attractive potential of mean force. Several theoretical works have incorporated depletion attraction into the Onsager theory [84, 47] and a simulation has also been performed [10]. These studies predict a widening of the biphasic $I$-$N$ gap. These results are in qualitative agreement with the measured $I$-$N$ transition in mixtures

of boehmite rods and polystyrene polymers and mixtures of charged semiflexible fd virus and dextran polymers [12, 81, 19]. For the case of direct interparticle attraction, theory also predicts that the width of the $I$-$N$ coexistence increases abruptly with increasing attraction [24, 73]. However, in experiments with the semiflexible polymer, PBG, experiments show that a gel phase supersedes the $I$-$N$ [55].

In this work, we consider the effect of direct attractions on the phase behavior of colloidal rod-like particles. As a model colloidal rod we use aqueous suspensions of filamentous semiflexible bacteriophage fd. Suspensions of fd have been previously shown to exhibit an $I$-$N$ transition in agreement with theoretical predictions for semiflexible rods interacting with a salt dependent effective hard rod diameter $D_{\text{eff}}$ [78]. Although fd forms a cholesteric phase, the difference in free energy between the cholesteric and nematic phases is much smaller than that between the isotropic and nematic phases. Hence we refer to the cholesteric phase as the nematic phase in this paper.

We have developed a temperature sensitive aqueous suspension of colloidal rods. Specifically, thermosensitive poly(N-isopropylacrylamide) polymers (PNIPAM) are covalently linked to the virus major coat protein pVIII. Solutions of PNIPAM have a lower critical solution temperature (LCST) in water. Below its LCST of 32°C, PNIPAM is readily soluble in water, while above its LCST the polymer sheds much of its bound water and becomes hydrophobic, which leads to collapse of the coil, attraction between polymers, and phase separation [16, 70]. The fd virus has been shown to have a robust thermal stability up to 90°C [85]. Previously mixtures of fd and PNIPAM have been used to investigate melting of lamellar phases [2]. Here we explore the behavior of suspensions of fd-PNIPAM particles as a function of temperature. A reversible sol-gel transition is found for both the isotropic and nematic phase and is studied in detail with dynamic light scattering (DLS) and rheometry. As the system can be driven reversibly from a fluidic state to a gel state, fd-PNIPAM suspensions

are a versatile model system to study the fundamental properties of entangled and crosslinked networks of semiflexible polymers.

## 2.2 Materials and Methods

### 2.2.1 Preparation of fd-PNIPAM complexes

Bacteriophage fd is a rodlike semiflexible polymer of length $L = 880$ nm, diameter $D = 6.6$ nm, molecular weight $1.64 \times 10^7$ dalton, surface charge density $7e^-$/nm at $p$H = 8.2 and persistence length between 1 and 2 $\mu$m [25, 43]. There are approximately 2700 major coat proteins helically wrapped around the phage genome of a single-stranded DNA. The fd virus is grown and purified as described elsewhere [52]. The virus concentration is determined by UV absorption at 269 nm using an extinction coefficient of 3.84 cm$^2$/mg on a spectrophotometer (Cary-50, Varian, Palo Alto, CA).

About 30 mg NHS-terminated PNIPAM with molecular weight of $10,000$ g/mol (Polymer Source Inc., Quebec, Canada) is mixed with 800 $\mu$l of 24 mg/ml fd solution for 1 h in 20 mM phosphate buffer at $p$H = 8.0. The reaction product is centrifuged repeatedly to remove the excess polymers. The PNIPAM-bound fd virus is stored in 5 mM phosphate buffer at 4°C for future use. Using a differential refractometer (Brookhaven Instruments, Holtsville, NY) at $\lambda = 620$ nm, the refractive index increment, $(dn/dc)$, is measured to estimate the degree of polymer coverage of the fd virus [31]. There are $336 \pm 60$ polymer chains grafted on each virus, which corresponds to a grafting density of $N/\pi DL = 0.02$ PNIPAM/nm$^2$, a nearly complete coverage of the rod by the polymer.

### 2.2.2 Dynamic light scattering

In a homodyne light scattering experiment, the time correlation function of the scattered light intensity is acquired,

$$G_I(q,t) = \frac{\langle I(q,0)I(q,t)\rangle}{\langle I(q)\rangle^2} \tag{2.1}$$

This can be related to the correlation function of the electric field by the Siegert relation [9],

$$G_E(q,t) = \sqrt{G_I(q,t)^2 - 1} \tag{2.2}$$

where

$$G_E(q,t) = \frac{\langle E^*(q,0)E(q,t)\rangle}{\langle I(q,t)\rangle} \tag{2.3}$$

An effective diffusion coefficient can be defined by the first cumulant

$$D_{\text{eff}}(q) = \Gamma(q)/q^2 \tag{2.4}$$

where

$$\Gamma = -\frac{d}{dt}[\ln G_E(q,t)]_{t\to 0} \tag{2.5}$$

Here the $D_{\text{eff}}(q)$ reflects the different types of motion associated with the rod-like fd-PNIPAM particle, including translation, rotation and bending motion.

A light scattering apparatus (ALV, Langen, Germany) consisting of a computer controlled goniometer table with focusing and detector optics, a power stabilized 22 mW HeNe laser ($\lambda = 633$ nm), and an avalanche photodiode detector connected to an $8 \times 8$ bit multiple tau digital correlator with 288 channels was used to measure the

correlation function. The temperature of the sample cell in the goniometer system is controlled to within ±0.1°C.

To remove dusts and air bubbles in the fd-PNIPAM solution, the sample was passed through a 0.45 $\mu$m filter and centrifuged at 3000 rpm for 15 min before each measurement. The correlation function of the scattered light intensity was measured at a scattering angle of 90°. The particle concentration ranges from $2c^*$ to $4c^*$ with the critical concentration $c^* = 1$ particle/$L^3$ or 0.04 mg/ml.

### 2.2.3 Rheological characterization of fd-PNIPAM suspensions

The rheological measurements were carried out on a stress-controlled rheometer (TA Instruments, New Castle, DE) using a stainless steel cone/plate tool (2° cone angle, 20 mm cone diameter). The gap is set at 70 $\mu$m at the center of the tool. The torque range is 3 nN·m to 200 mN·m, and the torque resolution is 0.1 nN·m. The temperature control is achieved by using a Peltier plate, with a range of −20°C to 200°C and an accuracy of ±0.1°C.

The storage and loss moduli, $G'(\omega)$ and $G''(\omega)$, respectively, are measured as a function of frequency by applying a small amplitude oscillatory stress at a strain amplitude $\gamma = 0.03$. A strain sweep is conducted prior to the frequency sweep to ensure the operation is within the linear viscoelastic regime.

## 2.3 Results and Discussion

Onsager [61] first predicted that there is an $I$-$N$ phase transition in suspensions of hard rods when the number density of rods $c$ reaches $\frac{1}{4}c\pi L^2 D = 4$, where $L$ and $D$ are the length and diameter of rod, respectively. Since the fd virus is charged, it's necessary to account for the electrostatic repulsion by substituting the bare di-

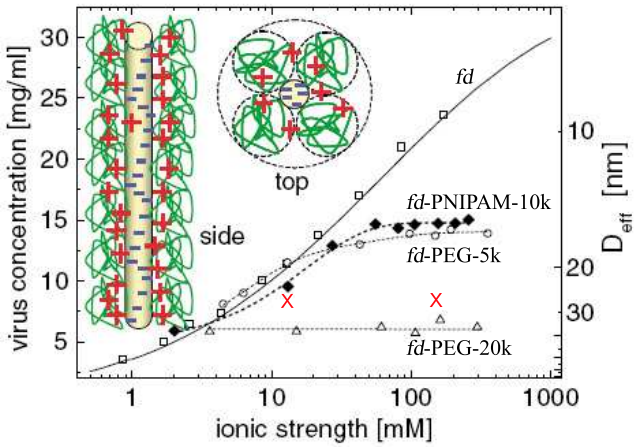


Figure 2.1: (Color online) Isotropic-nematic coexistence concentration of PNIPAM-coated fd virus as a function of ionic strength (solid symbol). The lines indicate the highest concentration for which the isotropic phase is stable. Plotted in addition for comparison is data on wild-type fd, fd-PEG-5k and fd-PEG-20k [17]. As the salt concentration increases, the fd-PNIPAM system transitions from an electrostatically-stabilized suspension to a sterically-stabilized suspension. This is schematically demonstrated by the cartoon of fd-PNIPAM particle with $D_{\rm eff}^{\rm electrostatic} < D_{\rm eff}^{\rm polymer}$. The cross symbol denotes two conditions for which the rheological properties of fd-PNIPAM were measured.

ameter $D$ with an effective diameter $D_{\rm eff}$, which is larger than $D$ by an amount roughly proportional to the Debye screening length. As the solution ionic strength increases, $D_{\rm eff}$ decreases and eventually approaches $D$. Fig. 2.1 presents the $I$-$N$ coexisting concentrations, $c$, as a function of ionic strength for fd [78], showing that $c$ rises with increasing ionic strength and, in fact, $c \propto 1/D_{\rm eff}$. Fig. 2.1 also shows co-existence concentrations for fd to which different polymers (PEG [17], PNIPAM) have been covalently grafted to its surface. The polymer grafted particles are denoted as fd-PEG [17] and fd-PNIPAM, respectively. All measurements are made at room temperature under conditions for which water is a good solvent for both the PEG and PNIPAM polymers. The $I$-$N$ co-existence concentrations of both fd-PEG and fd-PNIPAM are independent of ionic strength at high ionic strength. The physical picture is that the electrostatic effective diameter $D_{\rm eff}$ decreases with increasing ionic

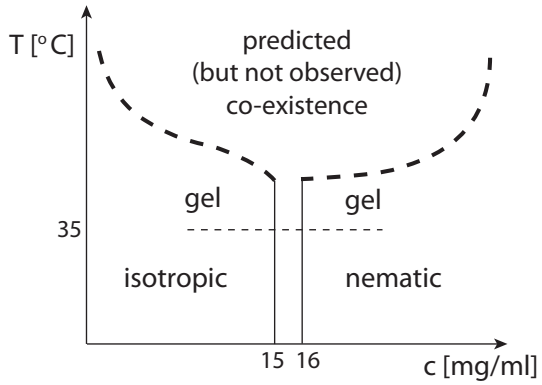


Figure 2.2: Predicted phase diagram for attractive fd-PNIPAM at 155 mM ionic strength [24, 73]. The solid and light dashed lines indicate what is observed, a narrow isotropic-nematic co-existence that does not vary with temperature. Above 35°C the samples gel irrespective of phase. The heavy dash line indicates what we expect qualitatively but did not observe, a sudden widening of co-existence region with increased attraction between rods.

strength. However, there is also a diameter associated with the polymer diameter, $D_{\text{poly}}$, which is independent of ionic strength (at least for the range of salt concentration in this experiment). Once $D_{\text{eff}} < D + 2D_{\text{poly}}$ the interparticle interactions are dominated by steric repulsion of the grafted polymer and not electrostatic repulsion. For fd-PNIPAM the transition from electrostatic to polymer stabilized interactions occurs at $D_{\text{eff}} \sim 17$ nm. Since the bare fd diameter $D = 7$ nm, the grafted PNIPAM has a corresponding diameter $D_{\text{poly}} = 5$ nm, which is comparable to the literature value of the diameter of gyration of PNIPAM in dilute solute of $D_{\text{g}} = 6.4$ nm [44].

We study the phase behavior of fd-PNIPAM in response to temperature changes. We prepare samples in the isotropic (9.6 mg/ml) and nematic (21 mg/ml) phases at an ionic strength $I = 155$ mM. At room temperature, both isotropic and nematic samples are transparent viscous fluids. The nematic sample exhibits birefringence under cross polarizers whereas the isotropic sample does not. As the temperature is increased to $T = 40$°C, the samples rapidly turn into viscoelastic gels. These behaviors can be observed by simply tilting the vial, and observing the formation of

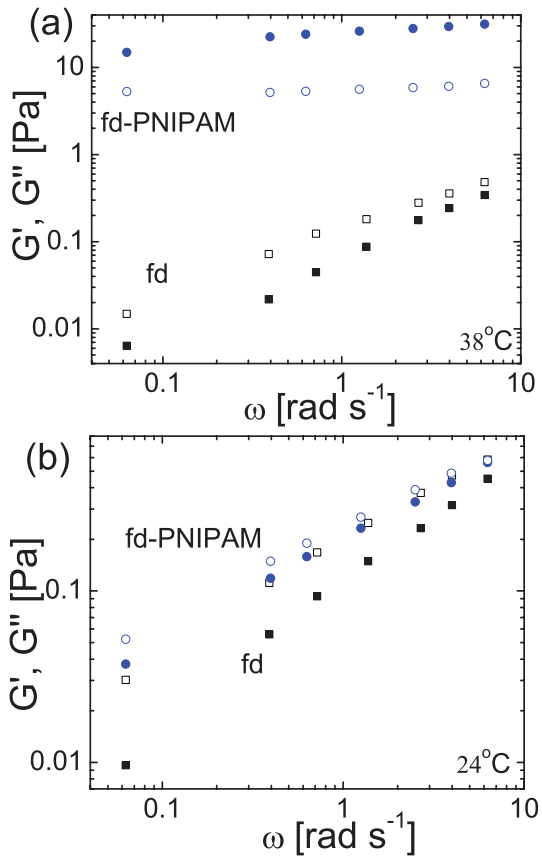


Figure 2.3: Storage modulus (solid symbol) and loss modulus (open symbol) of fd (squares) and fd-PNIPAM (circles) suspensions at two different temperatures. (a) $T = 38°$C, (b) $T = 24°$C. The concentration of the samples are about 8 mg/ml. The solution ionic strength is 155 mM.

a weight-bearing gel. As the temperature returns to room temperature, the samples flow like fluids again. The entire process can be repeated multiple times, which indicates a reversible sol-gel transition. This observation can be interpreted as the result of increased hydrophobic attraction among monomers along the PNIPAM chain leading to the collapse of PNIPAM coils into globules at elevated temperature and thus leading to an attraction between the fd-PNIPAM rods [27].

We load the above mentioned samples into glass capillaries that are subsequently sealed with a flame. The samples are placed in a heated block at 40°C, and monitored

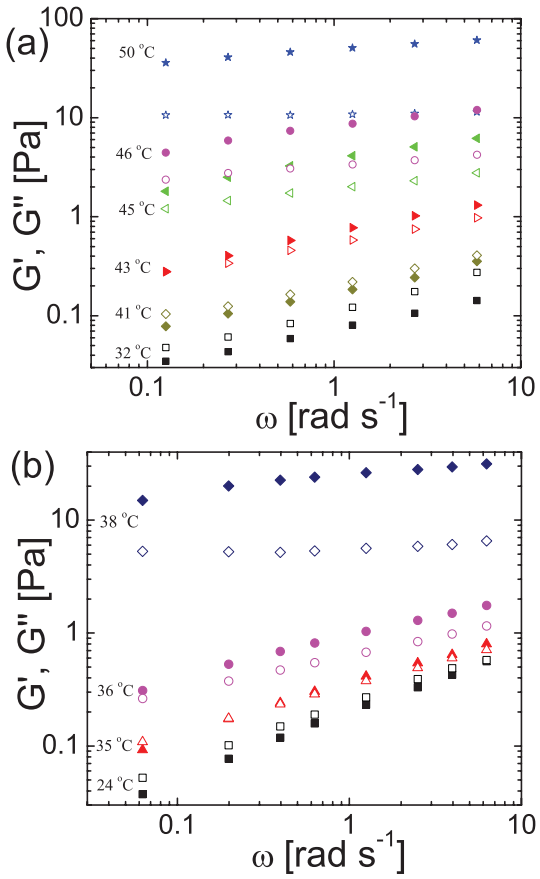


Figure 2.4: Storage modulus (solid symbol) and loss modulus (open symbol) of fd-PNIPAM solution as a function of temperature. Ionic strength $I$ = (a) 13 mM, (b) 155 mM. The concentration of the samples are about 8 mg/ml.

with polarizing microscopy for up to a week. No phase separation was observed for either the isotropic or nematic samples, which remain in their respective phases. This is qualitatively different from theory, which predicts that increased attraction leads to enhanced phase separation [47, 24, 73]. We speculate that the "sticky" rods at high temperature could be kinetically arrested in a non-equilibrium state and therefore do not phase separate during the course of the experiment. As shown in Fig. 2.2, an increase of temperature, or equivalently attraction, did not induce the solution of rods to phase separate. Instead, with increasing temperature, a gel phase forms at a temperature that is presumably below that at which the phase diagram opens up

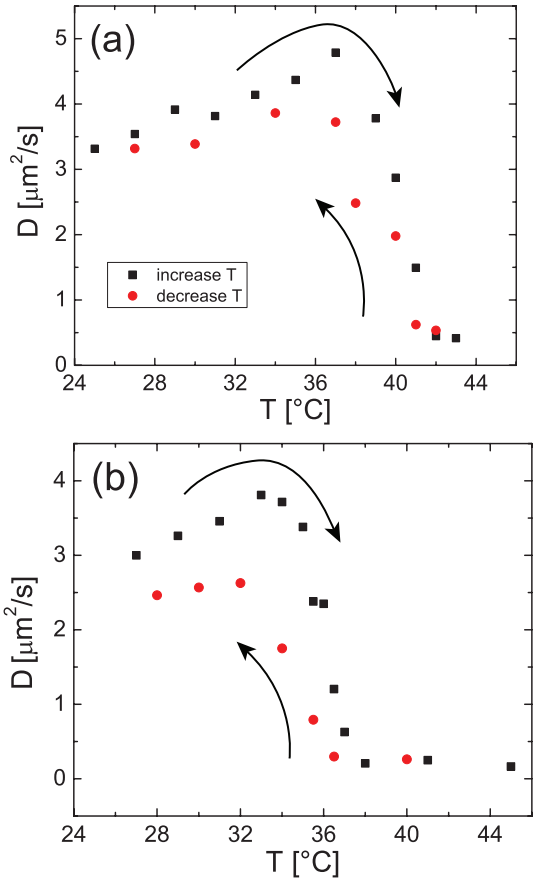


Figure 2.5: Diffusion coefficients of fd-PNIPAM at 0.l5 mg/ml as functions of temperature. Ionic strength $I$ = (a) 13 mM, (b) 155 mM. These values are determined from the first cumulant of $G_E(q,t)$ using Eq. (2.4).

into a dense nematic coexisting with a dilute isotropic.

We employ rheometry to characterize the gelation of the fd-PNIPAM suspension. Fig. 2.3 shows $G'(\omega)$ and $G''(\omega)$ for bare fd and fd-PNIPAM solutions measured at two different temperatures. Temperature change has little effect on the storage and loss moduli of the bare fd suspension. By fitting the data to a power law, we have for fd $G'(\omega) \propto \omega^{0.9}$ and $G''(\omega) \propto \omega^{0.7}$. The frequency exponents are consistent with those measured with microrheology [71]. In contrast, fd-PNIPAM becomes solid-like at 38°C with $G'$ about five times greater than $G''$. The linear moduli are nearly

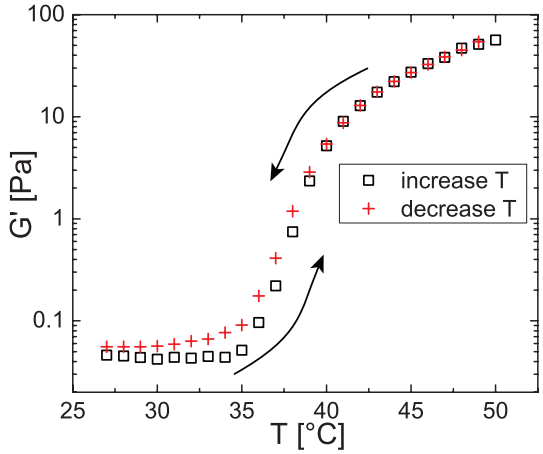


Figure 2.6: Reversibility of temperature-induced sol-gel transition. Measurements are made for fd-PNIPAM suspension at 8.4 mg/ml and $I = 13$ mM with increasing and decreasing temperature. The sample is oscillatorily probed at 1 Hz and the rate of temperature change is approximately 1°C/10 min in both directions.

independent of frequency: $G'(\omega) \propto \omega^{0.14}$ and $G''(\omega) \propto \omega^{0.05}$.

We investigate the effect of ionic strength on the gelation of the fd-PNIPAM network. Fig. 2.4 illustrates the frequency-dependent viscoelastic moduli as a function of temperature. Parts (a) and (b) represent data taken near the gel point $T = T_c$ from samples under low and high salt conditions, respectively. For $T < T_c$, the suspension shows characteristics typical of a viscous fluid. The gel point is identified as the temperature at which $G'(\omega)$ and $G''(\omega)$ assume the same power law dependence on oscillation frequency [86]. As the temperature increases beyond $T = T_c$, both $G'(\omega)$ and $G''(\omega)$ increase dramatically for the fd-PNIPAM sample and the suspension is clearly gel-like with $G'(\omega)$ weakly dependent on $\omega$.

The data in Fig. 2.4 shows the high and low salt suspensions reach the gel point at different temperatures with the same power law slope. The sample at low ionic strength solidifies at $T_c = 41$°C, which is significantly greater than the 35°C gelling temperature for the sample at high ionic strength. However, both suspensions exhibit the same power law exponent $n = 0.40 \pm 0.02$ at the gel point.

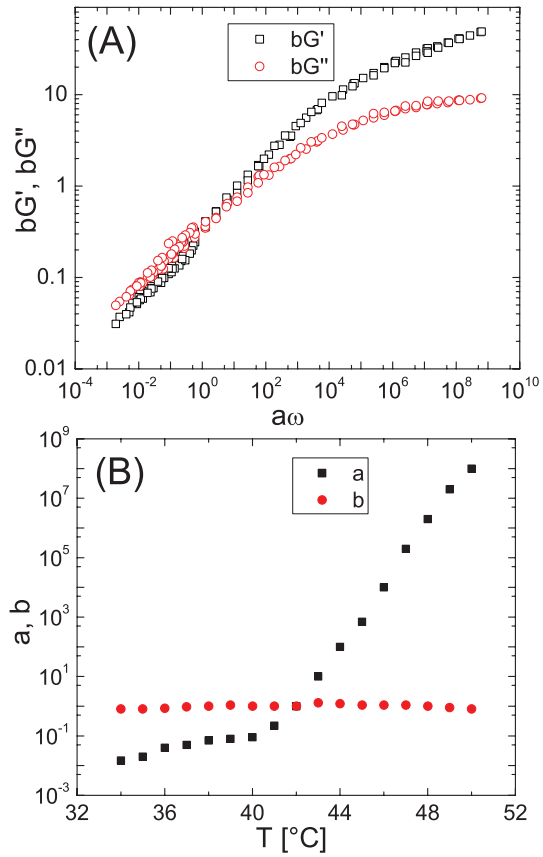


Figure 2.7: (A) Master curve showing scaled moduli as functions of scaled frequency. (B) Relationship between shift factors and temperature. a: frequency shift factor. b: modulus shift factor.

As a check for the gel point, dynamic light scattering is performed on the fd-PNIPAM suspensions as shown in Fig. 2.5. The onsets of aggregation for the low and high ionic strengths occur at 41°C and 36°C, respectively. Gelation occurs at the same temperatures as determined by light scattering and rheology. This ionic strength dependence of the gelation temperature arises from the fact that lowering solution ionic strength increases the electrostatic repulsion between the rods, and therefore a larger attraction from the PNIPAM is required to induce aggregation. The influence of ionic strength on the LCST of PNIPAM is rather small in the concentration range of monovalent salt used in this study [87], therefore it is not considered here.

A recent study by Zhang et al. [88] reports an investigation of aqueous solutions of fd-PNIPAM with comparable grafting density and molecular weights of polymers to this study. The $I$-$N$ coexistence concentration and the gelling temperature obtained in the above paper are close to our results. Zhang et al. characterized the structure of the nematic gel, whereas we focus on the viscoelasticity of fd-PNIPAM solution in the isotropic phase.

To test the reversibility of the temperature-induced sol-gel transition, measurements are carried out on $G'$ at a constant frequency of 1 Hz with increasing and decreasing temperature (Fig. 2.6). A slight hysteresis is found during the temperature sweep.

The storage and loss moduli curves at different temperatures can be scaled onto master curves. Through a procedure called time-temperature superposition [23], the frequency dependent $G'$ and $G''$ curves measured at different temperatures can be superposed by shifting along the logarithmic frequency and modulus axes. Specifically we shift data at lower temperatures towards lower frequencies with respect to data at higher temperatures. Time-temperature superposition enables one to probe viscoelasticity for a much larger frequency range than that experimentally accessible. The master curve as shown in Fig. 2.7(A) reveals that fd-PNIPAM suspensions behave as a thermo-rheologically simple fluid, which means a variation in temperature corresponds to a shift in time scale [23]. The rheological behaviors of fd-PNIPAM are reminiscent of those of polymer melts [46]. At high frequencies, or times shorter than the reptation time, melts behave as solids, while at low frequency the melt can flow. In Figure 2.7 similar behavior is observed. At high frequency, which corresponds to high temperature, $G'$ approaches a plateau value and is much larger than $G''$; thus the material behaves as a solid. In the low frequency limit, the suspension behaves more like a fluid. $G'$ and $G''$ cross at an intermediate frequency with the slope of $G''$ equal

to 0.36. The temperature-dependent shift factors are plotted in Fig. 2.7(B). Notably, the frequency shift factor exhibits a break of slope, signifying a phase transition, whereas there is only a minor shift along the logarithmic modulus axis.

Materials that are solid at high frequency and liquid like at low frequency are thixotropic [8]. This is in stark contrast to colloidal gels of precipitated silica particles [72], carbon nanotubes [56, 57, 33], and carbon black [80], whose fractal-like microscopic structure leads to the opposite rheological behavior; fluid like at high frequency and solid like at low frequency. We hypothesize that the difference in rheological properties between the colloidal gels and our attractive rods is in the nature of the contact between the particles. For bare colloids, such as silica, the interparticle bond is rigid, whereas for the fd-PNIPAM the contact is between two polymers and the interaction is the same as in a polymer melt. At the long time scale of the rheological observation, grafted polymers from one rod that are in contact with those on another rod can sufficiently rearrange their configurations allowing the rods to move with respect to each other, and therefore the suspension flows like a viscous liquid. On a shorter time scale, the polymers are unable to relax and thus the network of rods behaves like a soft solid.

For practical applications it may be desirable to create nematic gels of sticky rods such as carbon nanotubes or biological filaments. The implication of our work is that the system has to be repulsively stabilized in order for a nematic to form, in spite of what is predicted theoretically. This is because a gel phase supersedes the $I$-$N$ coexistence as attraction is increased. In the case that a nematic gel is desired, one approach would be to start with a repulsion dominated nematic, such as the low temperature fd-PNIPAM nematic in our work, and then increase attraction so that a nematic gel is formed.

## 2.4 Conclusion

We have presented studies of a system of colloidal rods (fd) coated with the temperature-sensitive polymer (PNIPAM). At room temperature and high ionic strength, quantitative measurements of the $I$-$N$ transition show fd-PNIPAM behaves as a sterically stabilized suspension. An increase in temperature, or equivalently, strength of attraction, does not lead to a widening of the coexistence concentration as expected. Instead a sol-gel transition arises, which we attribute to the collapse of the grafted PNIPAM polymers. Dynamic light scattering and rheometry demonstrate that the gelling process is reversible and ionic strength dependant. Furthermore, the rheological master curves for samples of different temperatures show that the fd-PNIPAM suspensions are rheologically similar to simple polymeric melts.

# Chapter 3

# The Pair Potential of Colloidal Stars

## 3.1 Introduction

Polyelectrolyte brushes of flexible polymers have been the subject of many theoretical [62, 67, 6] and experimental [6] studies. Recently focus has shifted to semiflexible brushes [41] for which the persistence length $P$ is large compared to the monomer separation, but small compared to their contour length $L$, or $P << L$. In contrast, here we investigate brushes with $P \sim L$. The grafted brushes consist of bacteriophage M13 viruses, which are rodlike, semiflexible charged polymers of length $L = 880$ nm, diameter $D = 6.6$ nm, and persistence length $\sim 2$ $\mu$m [43, 75]. The bare, linear charge density of M13 is high; $\sim 7$ $e^-$/nm.

In this chapter, we describe "colloidal stars", which are analogous to star polymers [62, 40, 20, 39, 6], constructed by grafting genetically engineered M13 viruses [53] to polystyrene spheres. These stiff brushes represent a new class of stars. The M13 are rigid enough to form liquid crystals [18], but when grafted to a sphere remain

flexible enough to be distorted by the director field, as shown in Fig. 3.1. These colloidal structures are characterized by fluorescent microscopy, transmission electron microscopy (TEM) and fluorometry. The interaction potential is probed using laser tweezers. To extract the steeply varying pair-potential we develop a new experimental protocol based on the computer simulation method known as umbrella sampling [79], but modified to increase the protocol's efficiency under experimental constraints. This new method allows the measurement of potentials much greater in magnitude than done perviously with line traps [14, 50]. We find that the measured potential of the colloidal stars can be modeled as arising from the osmotic pressure of the counter-ions, which is in several fold excess of the repulsion due to rod excluded volume.

## 3.2 Materials and Methods

We carried out experiments to demonstrate the expression and unimpaired functionalities of the cysteine groups on pIII proteins. Approximately 10 $\mu$l of 1 mg/ml M13-C7C solution was incubated with 0.6 $\mu$M TCEP (Tris(2-carboxyethyl)phosphine) for 5 min in 20 mM phosphate buffer at $p$H = 7 to cleave the disulfide bridge formed between cysteine residues. Then, the mixture was reacted with 10 $\mu$l 10-nm colloidal Au (Ted Pella, Redding, CA) for about 2 h, allowing the free thiol groups on pIII proteins to bind to the Au nanoparticles. The resulting mesogen units of 10-nm Au nanopaticle-bound phages were visualized using transmission electron microscopy (TEM) after stained with 2% uranyl acetate (Fig. 3.1(a)). In another assay, 10 $\mu$l phage solution after being reduced with TCEP was reacted with 1.4-nm monomaleimido-nanogold® (Nanoprobes, Yaphank, NY) for 2 h. Au ions were then catalytically deposited on the Au nanoparticles by using a gold enhancement kit

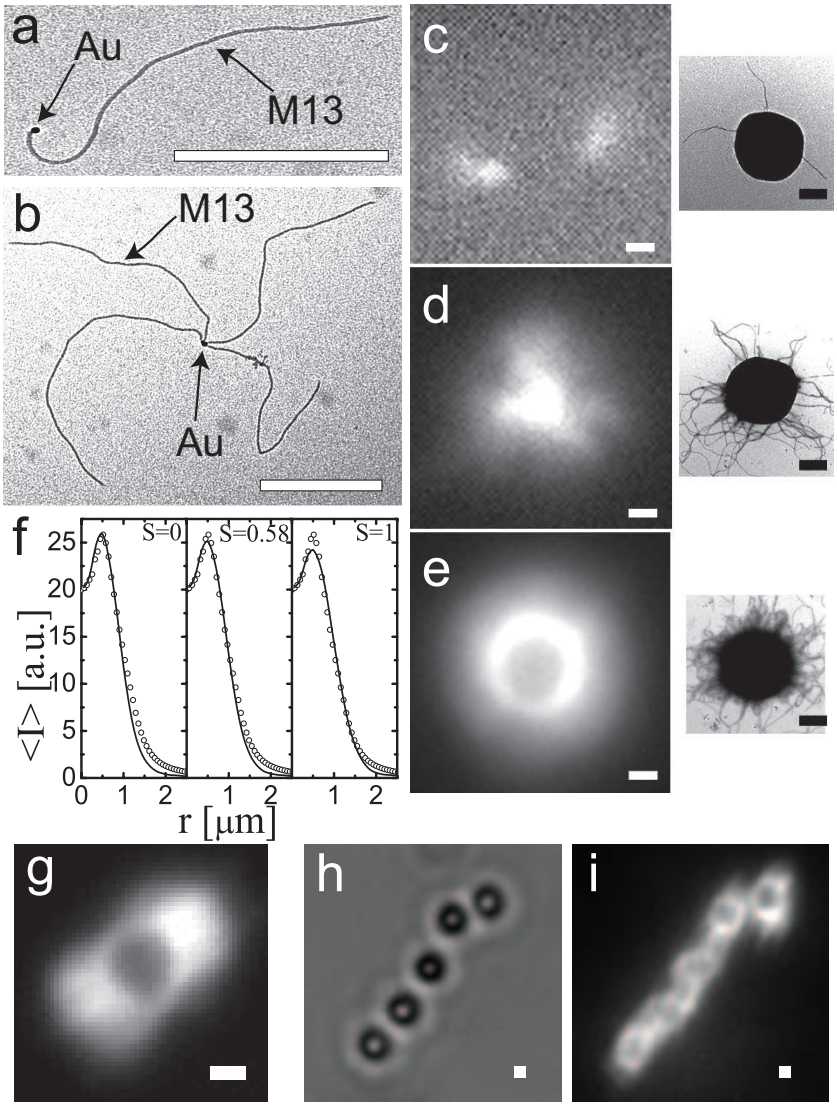


Figure 3.1: (a) and (b): TEM images of 10 nm Au-bound M13 viruses of different nanoarchitectures. (c)-(e): TEM (right panel) and fluorescence (left panel) images of labeled phage grafted to unlabeled 1 $\mu$m PS beads with varying grafting densities. (c) 3 phages/bead. (d) 38 phages/bead. (e) 135 phages/bead. (f): Radially-averaged fluorescent intensity profiles of the phage-grafted bead. Symbols: experiment; Solid curve: theoretical calculation with varying orientational order parameters ($S$) of anchored rods. (g): Fluorescent image of colloidal star in a M13 nematic (in contrast to (e) where the solvent is isotropic). The "hair" grafted to the bead is "combed" parallel to the director by the nematic. (h): Brightfield image of colloidal stars associating end-to-end in a M13 nematic. (i): Fluorescent image of (h). The combed stars associate in chains aligned parallel to the nematic director with surfaces separated by a micron. Bare spheres in a nematic also assemble into chains, but with surfaces in contact. The scale bars are 500 nm.

(Nanoprobes). After about 5 min of development, Au-phage star complexes form as shown in Fig. 3.1(b). More than 80% viruses observed had Au particles attached to their pIII ends.

However, the above two conjugation schemes suffer from their respective drawbacks. For the reaction of conjugating Au nanoparticles to thiols on pIII of phages, The efficiency is very low (less than 5% phages were seen to have Au bound to their pIII ends). Non-specific binding of Au particles to the major coat proteins (pVIII) was observed on 20% phages. Although the reaction of monomaleimido-nanogold® to viruses has better efficiency and is highly specific, it's difficult to grow Au nanoparticles on the ends of viruses in a controllable fashion: nanoAu nuclei would either grow into particles with a high polydispersity in sizes or simply aggregate during gold enhancement.

In what follows, we focus on the colloidal star constructed by attaching the engineered phages to a 1 micron diameter polystyrene sphere. This was done using the following procedure: First, 230 $\mu$l of 8.8 mg/ml M13-C7C was reduced with 2 $\mu$l of 0.18 mg/ml TCEP (Tris(2-carboxyethyl)phosphine) for 15 min. This M13-C7C solution was mixed with 2 $\mu$l of 19 mM maleimide-$PEO_2$-biotin (Pierce, Rockford, IL) for 1 h in 20 mM phosphate buffer at $p$H = 7.0. At this $p$H, the maleimide group is $\sim 1000$ times more reactive towards a free thiol group than an amine. At $p$H $> 7.5$, reactivity towards primary amines and hydrolysis of the maleimide group can occur. Considering the number ratio of major coat proteins pVIII to free thiol groups after reduction on a phage particle is about 270, biotinylation of the pVIII is still possible. The phage solution was dialyzed extensively against phosphate buffer to remove excess biotin and the $p$H was readjusted to 8.0. Subsequently, the phages were mixed for 1 h with 1 mg/ml Alexa Fluor® 488 carboxylic acid succinimidyl ester (Molecular Probes, Eugene, OR), and centrifuged four times at $170,000g$ for 1 h to remove free

dye molecules. 0.5 mg/ml of the fluorescently-labelled viruses were then incubated with 0.5%(w/v) straptavidin-coated polystyrene beads of diameter $d = 0.97 \pm 0.02$ $\mu$m (Bangs Laboratories, Fishers, IN) for 24 hours at room temperature. To the suspension 0.05 mg/ml $\alpha$-casein (Sigma, St. Louis, MO) was added and the whole mixture was centrifuged twice at $20,000g$ for 10 min. Finally, the pellet was resuspended in 100 $\mu$l of phosphate buffer (5 mM, $p$H 8.0) and stored at 4°C. The number of the sphere-bound viruses was determined using a fluorescence spectrophotometer (F-2000, Hitachi, Tokyo, Japan). By varying the stoichiometric ratio of biotinylated viruses to straptavidin-coated beads we created star polymers of different grafting densities as revealed by both fluorescence and TEM images (Fig. 3.1(c-e)). Fluorescent images were taken on a fluorescence microscope (TE2000-U, Nikon) equipped with a 100× oil-immersion objective and a cooled CCD camera (CoolSnap HQ, Roper Scientific). The TEM samples, stained with 2% uranyl acetate, were imaged with a 268 microscope (Morgagni, FEI Company, Hillsboro, OR), operating at 80 kV. Many of polystyrene spheres observed assume nonspherical shapes probably due to the fact that polystyrene collapses under electron beams.

Streptavidin is a homotetrameric protein with a biotin binding site in each subunit. The streptavidin-biotin interaction is the strongest known non-covalent binding with a dissociation constant estimated to be at $4 \times 10^{-14}$M [30]. Nonetheless, we have observed significant detachments of grafted phages two weeks after the conjugation of straptavidin-coated beads and biotinylated viruses. Therefore all microscopic observations and interaction measurements were made within a week of the preparation of star polymers.

At the grafting density of 135 phages/bead (Fig. 3.1e), the anchored dye-labelled rods form a spherically symmetric corona around the bead with a radially-averaged intensity (RAI) profile shown in Fig. 3.1(f). We model the phage-grafted bead as hard

rods anchored to the sphere with a Gaussian angle distribution, which is centered around the surface normal. The diffraction-limited fluorescent image of the colloidal star was computed by convolving the distribution of the rod's segments with the theoretical 3D point spread function (PSF) of the microscope [11]. As can be seen from Fig. 3.1(f) the calculated RAI profiles are insensitive to the orientational order parameter of the anchored rods $S = \frac{1}{2}\langle 3\cos^2\theta - 1\rangle$, where $\theta$ is the angle between the rod and the surface normal. However, the best fits were for intermediate order parameters.

The free energy as a function of separation between two colloidal particles $W_{\text{int}}(r)$ (the potential of mean force) can be determined up to an additive offset by the Boltzmann relation, $P(r) \sim \exp[-W_{\text{int}}(r)/k_{\text{B}}T]$. Experimentally this is accomplished by measuring the probability $P(r)$ of finding the particles at a separation $r$. However, for states of even moderate repulsive interaction energies $P(r)$ becomes very small. As a result, infrequent visitation of improbable states leads to poor statistics and errors in the determination of $P(r)$ which limited the magnitude of measured potentials in previous implementations of line traps, or single bias potentials to about $6\ k_{\text{B}}T$ [14, 50]. In this paper the maximum measured potential is $40\ k_{\text{B}}T$, but we estimate that potentials several times this value are feasible with the laser power and optical resolution of our instrument.

We achieve these measurements by employing the method of umbrella sampling, in which a biasing force is used to enhance sampling of rare configurations; results are then re-weighted to obtain the physical probability distribution [79]. Specifically, we place two colloidal stars (Fig. 3.2b) in separate laser traps and measure the histogram of separation distances between the colloids. The measurement is performed in a series of windows, each of which uses a different separation distance between the minima of the two laser traps. In each window the stars fluctuate about the

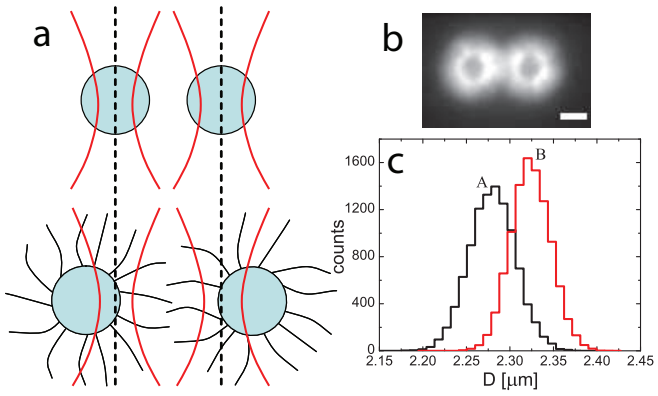


Figure 3.2: (color online). Excluded volume interaction of anchored rods. (a) the schematic and (b) the fluorescence image of phage-grafted beads in optical traps. (c) separation histograms of (A) bare beads and (B) phage-grafted beads for the same trap locations. The scale bar in (b) is 1 $\mu$m.

minimum of a total potential resulting from a combination of the dual traps and interparticle star potential. Only 6 $k_{\mathrm{B}}T$ of each of the total potentials is sampled and each minimum has a different energy, but here we show how the total potentials from overlapping windows can be combined to produce a single interparticle pair-potential of large range and magnitude. For the protocol typically used in simulations, results from different windows would be simultaneously re-weighted and stitched together to obtain a continuous function for the probability $P(r)$ using the weighted histogram analysis method (WHAM) [22, 45, 66]. However, the biasing potential is a function of two coordinates because the position of each bead is controlled by a separate trap. The number of independent measurements required for a particular level of statistical accuracy using WHAM rises exponentially with the number of dimensions of the biasing potential (even if the probability is projected onto a single coordinate). We overcome this limitation as follows.

Our goal is to measure the interaction potential, $W_{\mathrm{int}}(r)$ with $r \equiv x_2 - x_1$, between a pair of functionalized particles sitting at positions $(x_1, x_2)$ in a bias potential (laser trap) of strength $U_{\mathrm{bias}}(x_1, x_2)$. We achieve this goal by performing two experiments

(Fig. 2a). In one experiment we place two colloidal stars in two separate laser traps and in the other experiment we place two bare colloids in the same two traps. For both experiments we measure the separation histogram of the colloids as a function of the trap separation. The potential of mean force, $W_{\rm sub}$, is then obtained by subtracting the results from each experiment.

$$W_{\rm sub}(\hat{r})/k_{\rm B}T = -\log[f_{\rm f}(\hat{r})] + \log[f_{\rm nf}(\hat{r})] \tag{3.1}$$

with $f_{\rm f}(\hat{r})$ and $f_{\rm nf}(\hat{r})$ the fraction of measured displacements that fall within the histogram bin associated with the displacement value $\hat{r}$ for functionalized and non-functionalized beads, respectively. While this subtraction method has been used in previous experiments [14, 50], we rigorously prove its validity here and show how to implement it over multiple windows.

The fractions of measured displacements are governed by the Boltzmann distribution and given by

$$f_{\rm nf}(\hat{r}) = Z_{\rm nf}^{-1} \int dx_1 \int dx_2 e^{-U_{\rm bias}(x_1,x_2)/k_{\rm B}T} \delta(x_1 - x_2 - \hat{r}) \tag{3.2}$$

and

$$\begin{aligned} f_{\rm f}(\hat{r}) &= Z_{\rm f}^{-1} \int dx_1 \int dx_2 e^{-U_{\rm bias}(x_1,x_2)/k_{\rm B}T} \\ &\quad \times e^{-W_{\rm int}(x_2-x_1)/k_{\rm B}T} \delta(x_1 - x_2 - \hat{r}) \end{aligned} \tag{3.3}$$

with $\delta(r)$ the Dirac delta function and the normalization factors are given by

$$\begin{aligned} Z_{\rm nf} &= \int dx_1 \int dx_2 e^{-U_{\rm bias}(x_1,x_2)/k_{\rm B}T} \\ Z_{\rm f} &= \int dx_1 \int dx_2 e^{-U_{\rm bias}(x_1,x_2)/k_{\rm B}T} e^{-W_{\rm int}(x_2-x_1)/k_{\rm B}T} \end{aligned} \tag{3.4}$$

We change the integration variables to $x_1$ and $r \equiv x_2 - x_1$ and integrate over $r$ to obtain

$$\begin{aligned} f_{\rm nf}(\hat{r}) &= Z_{\rm nf}^{-1} \int dx_1 e^{-U_{\rm bias}(x_1,\hat{r})/k_{\rm B}T} \\ f_{\rm f}(\hat{r}) &= Z_{\rm f}^{-1} e^{-W_{\rm int}(\hat{r})/k_{\rm B}T} \int dx_1 e^{-U_{\rm bias}(x_1,\hat{r})/k_{\rm B}T}. \end{aligned} \tag{3.5}$$

Inserting this result into Eq. 3.1 gives the calculated potential of mean force:

$$W_{\rm sub}(\hat{r}) = W_{\rm int}(\hat{r}) + k_{\rm B}T \log(Z_{\rm f}/Z_{\rm nf}). \tag{3.6}$$

We see that $W_{\rm sub}(\hat{r}) = W_{\rm int}(\hat{r})$ plus a constant. As discussed above, the strength of the laser traps, $U_{\rm bias}(x_1, x_2)$, is such that the colloids sample only a small range and therefore only a small piece of the interaction potential $W_{\rm int}(\hat{r})$ is obtained. To determine a wider range of $W_{\rm int}(\hat{r})$ the laser trap separation is varied and $W_{\rm sub}(\hat{r})$ is obtained anew. Although the constant term is different for each separation of the traps, the entire potential can be stitched together to within a single additive constant by assuming that $W_{\rm int}(\hat{r})$ is continuous.

As a check of this implementation of the umbrella sampling algorithm, we used computer simulations to model the experiment. The results validating this method are shown in Fig. 3.3d.

The experimental system is shown schematically in Fig. 3.2a. The fluorescence image of trapped beads is shown in Fig. 3.2b. Optical tweezer setup is built around the inverted fluorescence microscope. A single laser beam is time-shared between two points via a pair of orthogonally oriented paratellurite ($TeO_2$) acousto-optic deflectors (AOD, Intra-Action, Bellwood, IL). About 30 mW of a 1064-nm laser (Laser Quantum, Cheshire, UK) is projected onto the back focal plane of an oil-immersion objective (100×, N.A.=1.3, Nikon) and subsequently focused into the sample cham-

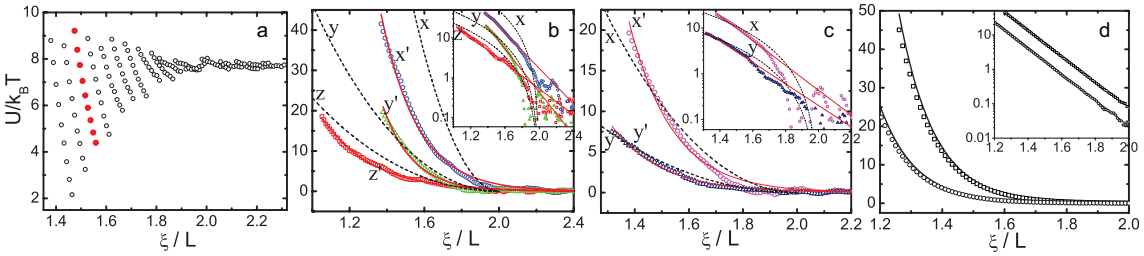


Figure 3.3: (color online). (a) A set of interaction potentials of M13-grafted micron-sized polystyrene spheres acquired from each umbrella window, with the ionic strength $I = 14$ mM and the grafting density $\sigma = 135$ phages/bead. The solid symbols indicate the potential extracted from the histograms shown in Fig. 3.2c. (b) Pair interaction potentials of colloidal stars at varying solution ionic strengths with $\sigma = 135$ phages/bead. Symbols: experiment; dashed lines: theory; solid lines: single exponential fits. (∘,x') and (x): 2.8 mM; (△,y') and (y): 14 mM; (□,z') and (z): 28 mM. (c) Pair potentials at different grafting densities with $I = 14$ mM. (∘,x') and (x): 135 phages/bead; (△,y') and (y): 80 phages/bead. (d) Interaction potentials $U/k_{\rm B}T = Be^{-10(r-2.2)}$ employed in the Langevin dynamics simulation (Solid lines) and bias potential $U_{\rm bias}(\mathbf{r}_1, \mathbf{r}_2) = \frac{1}{2}k_1|\mathbf{r}_1 - \mathbf{r}_{c1}|^2 + \frac{1}{2}k_2|\mathbf{r}_2 - \mathbf{r}_{c2}|^2$. Pair potentials extracted using the umbrella sampling (empty symbols). $B = 6$ (circle) and 20 (square). Insets: data replotted to facilitate comparison. $\xi$ is the separation between the surfaces of spheres and $L$ the virus length.

ber. Spheres are trapped 5 $\mu$m away from the surface to minimize possible wall effects. We choose a set of umbrella window potentials by systematically varying the locations of the traps' centers $\mathbf{r}_{c1}$ and $\mathbf{r}_{c2}$. For each window potential, six minutes of video are recorded for a pair of phage-grafted beads, and the separation probability distribution, $f_{\rm f}(\hat{r})$ is obtained. It is a simple Gaussian if the separation is large and the beads are not interacting. The distances between trap positions are selected so that there are sufficient overlaps between adjacent positions. We collected data for $\sim$ 30 different trap positions with 50 nm increments in separation to cover a wide range of the interparticle potential. Under identical conditions (microscope illumination, laser power, sample buffer, etc.), the experiment was repeated immediately for a pair of streptavidin-coated PS beads without attached virus to measure $f_{\rm nf}(\hat{r})$. For all experiments, statistically independent configurations of beads were sampled at 30 frames/sec. We analyzed the video images using a custom program written in the language IDL [13]. By constructing a histogram of center-center separations on $10^4$ images in each window, we found clear differences between the separation probability distributions of virus-grafted beads $f_{\rm f}(\hat{r})$ and bare beads $f_{\rm nf}(\hat{r})$ (Fig. 3.2c).

## 3.3 Theory of Interactions between Star Polymers

In this section we describe two theoretical models, developed by Dr. Michael Hagan, to understand our experimental results. It is shown that the pair potential between colloidal stars is dominated by the entropic interaction arising from the trapped counterions, whereas the excluded volume interaction of grafted rods plays only a minor role.

### 3.3.1 Excluded Volume Interaction between Rod-Grafted Spheres

In this section, we consider spheres uniformly grafted with rod-like particles. As the spheres approach each other, the positional and orientational configurations of the grafted rods become increasingly constrained, giving rise to a reduction of total entropy and hence an increase in the Helmholtz free energy. Following the second virial expansion of free energy (see section1.2.1), we solve the pair potential caused by mutually avoiding rods as a function of the separation between spheres. The computational procedure is discussed as follows. We first find the potential of mean force between two infinite parallel planes, assuming a uniform orientational distribution of rods (excluding orientations that would overlap with the plane); the potential between two spheres then follows by the Derjaguin approximation [36].

$$f_s(D) \approx \int_D^\infty 2\pi \frac{R_1 R_2}{R_1 + R_2} f_p(Z) dZ = \pi R W_p(D) \tag{3.7}$$

Here we have set the radii of spheres to be equal, $R_1 = R_2 = R$. The potential energy between spheres is obtained by a further integration and takes the form

$$W_s = \int_D^\infty f_s(D') dD' \tag{3.8}$$

Fig. 3.4 demonstrates the geometry of the excluded volume calculation for two rods attached to parallel plates. Consider rod 1 at $(\theta_1, \phi_1)$ and rod 2 at $(\theta_2, \phi_2)$ attached to plated 1 and plate 2 respectively. We fix the orientations of both rods and slide rod 2 along plate 2. From elementary geometry and vector analysis, the excluded area on plate 2 by rod 1 to the contact point of rod 2 is indicated as the shaded part

$$A_{\text{exc}}(\theta_1, \theta_2, \phi) = 2 D_{\text{eff}} l \tag{3.9}$$

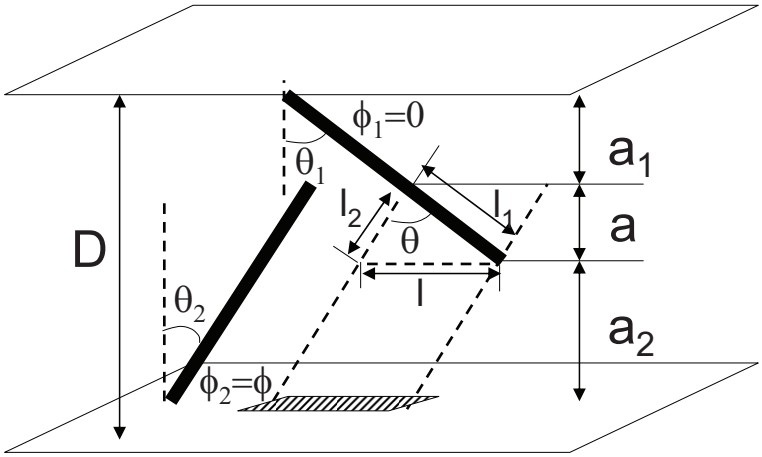


Figure 3.4: A sketch of the excluded volume interactions between rods grafted to parallel plates.

where

$$l^2 = l_1^2 + l_2^2 - 2l_1 l_2 \cos\theta \tag{3.10}$$

$$l_1 = L - a_1/\cos\theta_1 = L - (D_s - L\cos\theta_2)/\cos\theta_1 \tag{3.11}$$

$$l_2 = L - a_2/\cos\theta_2 = L - (D_s - L\cos\theta_1)/\cos\theta_2 \tag{3.12}$$

$$\cos\theta = -\sin\theta_1 \sin\theta_2 \cos\phi + \cos\theta_1 \cos\theta_2 \tag{3.13}$$

Here $D_{\text{eff}}$ and $L$ are the effective diameter and the length of the rod, respectively.

Assuming a uniform orientational distribution, we have for the average of Eq. 3.9 over all directions

$$\bar{A}_{\text{exc}} = 2D_{eff}\frac{1}{2\pi}\int_0^{\pi/2} d\theta_1 \sin\theta_1 \int_0^{\pi/2} d\theta_2 \sin\theta_2 \int_0^{2\pi} d\phi H[a(\theta 1, \theta 2, \phi)] \cdot l(\theta 1, \theta 2, \phi \tag{3.14}$$

where H is the heavyside step function, that eliminates orientational configurations in which rods are not touching each other irrespective of their relative positions.

To the second order of rod concentration, the interaction potential per unit area

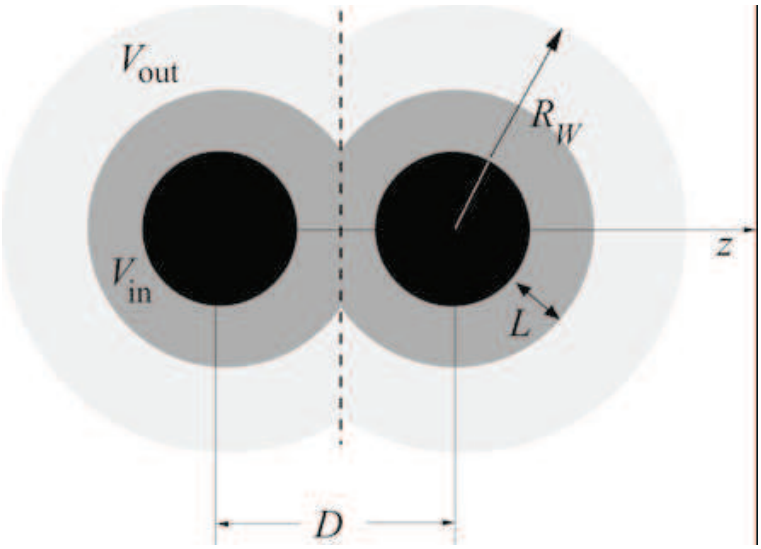


Figure 3.5: A sketch of two polyelectrolyte-brushes of core radius Rc (black center spheres) each, held at center-to-center separation D. The dark fused spheres denote the brush regime of thickness L and have a total volume Vin. The light eight-shaped hollow region of volume Vout denotes the region in which the free counterions can move. The graph is taken from Ref. [39].

between parallel plates is given by

$$\frac{W_p}{Ak_BT} = \sigma^2 A_{exc} \tag{3.15}$$

This interaction energy can be related to the force between spheres by the Derjaguin approximation (Eq. 3.7). One further integration over distance would lead to the pair potential between the rod-grafted spheres

$$W_s(D_s) = -\pi R \int_{\infty}^{D_s} W_p(D')dD' \tag{3.16}$$

### 3.3.2 Counterion-Induced Entropic Interaction between Polyelectrolyte Stars

In the seminal paper by Pincus [62], he presented a theory on interactions of polyelectrolyte (PE) stars, based on scaling ideas. One of the key points of that work is that the force acting between PE stars is dominated by the entropic contribution of the trapped conterions. Jusufi et al.[40, 39] put forward an analytical theory for the conformations and interactions of PE stars and compared its predictions with results from molecular dynamics (MD) simulations. In what follows an outline of Jusufi's theory is given.

Isolated PE stars

In the model, the star is envisioned as a sphere of radius $R$. The counterions, $N_c$, are partitioned into three states: $N_1$ condensed counterions within $f$ tubes around the branches of the star; $N_2$ trapped counterions inside the star; $N_3$ free counterions that move into the bulk of the solution. The equilibrium values for $R$ and $N_i$ are obtained by minimization of a variational free energy, which we write as

$$F(R, N_i) = U_{\mathrm{H}} + F_{\mathrm{el}} + F_{\mathrm{sa}} + \sum_{i=1}^{3} S_i \tag{3.17}$$

where $U_{\mathrm{H}}$ is the Hartree-type, mean-field electrostatic energy of the whole star with $\rho(\mathbf{r})$ the local charge density.

$$U_{\mathrm{H}} = \frac{1}{2\epsilon} \int \int d^3r d^3r' \frac{\rho(\mathbf{r})\rho(\mathbf{r}')}{|\rho(\mathbf{r}) - \rho(\mathbf{r}')|} \tag{3.18}$$

For the nonelectrostatic contributions, we have the elastic contribution of the chains $\frac{F_{\rm el}}{k_{\rm B}T} = \frac{3fR^2}{2N\sigma^2}$, where $\sigma$ and $N$ are the size and number of monomers, respectively. It's a Gaussian approximation of the conformational entropy of the arms of the star. To account for self-avoidance we employ the Flory-type expression, $\frac{F_{\rm sa}}{k_{\rm B}T} = \frac{3v(fN)^2}{8\pi R^3}$, where $v$ is the excluded volume parameter.

The ideal entropic contributions $S_i$ from counterions are of the form

$$\frac{S_i}{k_{\rm B}T} = \int_{V_i} d^3r \rho_i(\mathbf{r})[\ln(\rho_i(\mathbf{r})\sigma^3) - 1] + 3N_i \ln(\Lambda/\sigma) \tag{3.19}$$

where $\rho_i(\mathbf{r}) = N_i/V_i$ are the number densities of the counterions in the three different states. $\Lambda$ is the thermal de Broglie wavelength of the counterions. The last term of the entropic contributions only adds up to a constant $3N_c \ln(\Lambda/\sigma)$ and therefore will be dropped in what follows.

Interaction between two PE stars

The effective interaction between two PE stars, at a center-to-center distance $D$, is defined as

$$V_{\rm eff} = F_2(D) - F_2(\infty) \tag{3.20}$$

where $F_2(z)$ is the Helmholtz free energy of two PE stars at center-to-center separation $z$ [48]. $F_2(\infty)$ is simply twice the free energy of an isolated star as calculated in the preceding section. Since the $F_{\rm el}$ and $F_{\rm sa}$ are independent of $D$ they will not affect $V_{\rm eff}$. The electrostatic contribution $U_{\rm H}$ is neglected since the PE stars are almost electroneutral. Now the effective interaction arises from the entropic contribution of

the counterions inside the brushes, which is written as

$$V_{\text{eff}} = S(D) - S(\infty) \tag{3.21}$$

The geometry of calculation is sketched in Fig. 3.5. Under the condition that the charge density distribution falls off as $r^{-2}$ inside the star but is uniform outside, the final result assumes the following expression,

$$\frac{V_{\text{eff}}(D)}{k_{\text{B}}T} = \frac{Q}{|e|}\left[\frac{1}{2RK}\left(D\ln^2(\frac{D}{2R}) + 8R_c\ln(\frac{R_c}{R})\right) + \ln(\frac{2L}{RK}) - 2\frac{R_c}{L}\ln(\frac{R_c}{R})\right] \tag{3.22}$$

where $K$ is a dimensionless $D$-dependant parameter, $K = 1 - 2\frac{R_c}{R} + \frac{D}{2R}\left[1 - \ln(\frac{D}{2R})\right]$.

## 3.4 Results and Discussions

Fig. 3.3b shows the interaction potentials measured between two M13-grafted microspheres with varying solution ionic strengths. The interactions are all purely repulsive. The potential decays to zero as the distance between sphere surfaces increases beyond twice the virus length. There is a strong dependence of the pair potential on the ionic strength of the surrounding medium. A decrease in the solution ionic strength leads to increased interaction between spheres grafted with charged rods. We compare the interaction potential between microspheres at grafting densities of 80 and 135 viruses per sphere (Fig. 3.3c). The increase in density by 68% increases the pair-potential by a factor of 2.6, but does not change its functional form.

We calculated the interaction potential arising from the osmotic pressure of counterions trapped within the grafted layers based on the mean field calculation theory of Jusufi [40, 20, 39], except modified for the case where the density of fixed charges on the grafted rods is small compared to the salt concentration. In particular, the

densities of positive and negative ions within the grafted layer $\rho\pm(r)$ are given by $\rho\pm \approx \rho_{\rm s} \pm 0.5\rho_{\rm f}(r)$, with $\rho_{\rm s}$ the salt concentration and $\rho_{\rm f}(r) = \lambda_{\rm f} N_{\rm f}/(4\pi r^2)$ the fixed concentration of negative charges on the grafted rods, with $N_{\rm f}$ the number of rods per colloid and $\lambda_{\rm f} = 1.7e^-/\text{nm}$ an adjustable parameter for the linear charge density renormalized by condensation. The counterion excess free energy is calculated by integrating over the volume of the grafted layer $\int_0^\pi d\theta \sin\theta \int_{R_{\rm c}}^{R_{\rm c}+L_{\rm g}(\theta,\xi_{\rm c})} dr r^2 \rho_{\rm f}(r)^2/(2\rho_{\rm s})$ with $R_{\rm c} = 0.5$ $\mu$m the core radius, $\theta$ the angle with the center to center vector for the pair of colloids, and $\xi_{\rm c} = \xi + 2R_{\rm c}$ the center to center distance. Following the interaction geometry depicted in Fig. 5 of Ref. [39], the height of the grafted layer is $L_{\rm g} = L$ for $\theta \geq \theta_0$ and $L_{\rm g} = \xi_{\rm c}/(2\cos\theta) - R_{\rm c}$ for $\theta < \theta_0$ with $\cos\theta_0 = 0.5\xi_{\rm c}/(L + R_{\rm c})$. We have assumed $\rho_{\rm f} \ll \rho_{\rm s}$ and that the height of the unperturbed grafted layer is equal to the length of a virus, $L = 880$ nm (i.e. we neglect rod orientational fluctuations). Theory and experiment are compared in Figs. 3.3b & c; the agreement is rather good considering five measured potentials are fit with one value of the effective charge.

We also calculated the interaction due to the excluded volume of grafted rods based on the Onsager second virial expansion of the free energy [61]. For two rods, each with a specified orientation, we find the pairwise excluded area, or the space of relative grafting locations for which the rods overlap. The calculated interaction potential due to rod excluded volume was significantly smaller compared to the interaction due to counterion osmotic pressure; the latter interaction agrees well with the measured interaction potentials.

In conclusion, the umbrella sampling method is applied to extract the pair potential of the colloidal stars which are trapped with optical tweezers. The method allows for measurement of potentials of the order of 100 $k_{\rm B}T$, an energy much greater than previously measured with line traps. The large measured repulsive energy between colloidal stars is consistent with the osmotic pressure of counter-ions between

the charged brush, while a second virial theory based on the Onsager approximation significantly underestimates the pair potential. The construction of colloidal star polymers from genetically engineered viruses opens the possibility of a systematic study of hybrid colloidal materials exhibiting complex phase behaviors.

## 3.5 Appendix: Optical Tweezers

In this section, I briefly outline the principles of optical trapping theory and follow with a description of our experimental setup. At the end, video microscopy tracking is introduced for position detection. A more extensive discussion can be found in the review articles by Block and colleagues on the instrumentation [58] and the biological application [77] of optical trapping.

### 3.5.1 Optical Trapping Theory

It was first demonstrated by Arthur Ashkin [4] that the basic forces of radiation pressure could levitate and displace micron-sized dielectric particles in both air and water. For the sake of simplicity, one could consider two extreme cases in the theoretical treatment of optical forces. When the dielectric particle is large compared to the wavelength of the incident light (the diameter $d \gg \lambda$), one could use geometric optics to solve for the radiation pressure force on the particle. This is called ray optics regime. For dielectric particles much smaller than the light wavelength (the diameter $d \ll \lambda$), one is in the Rayleigh regime and the particle acts as a point dipole.

1. The ray optics regime ($d \gg \lambda$)

Each photon carries a momentum $p = \frac{E}{c} = \frac{h}{\lambda}$ where $E = h\upsilon$ is the energy of the photon with frequency $\upsilon$ and wavelength $\lambda$. Upon collision with a sphere, the photon's momentum changes. Due to the conservation of momentum, the sphere has to change

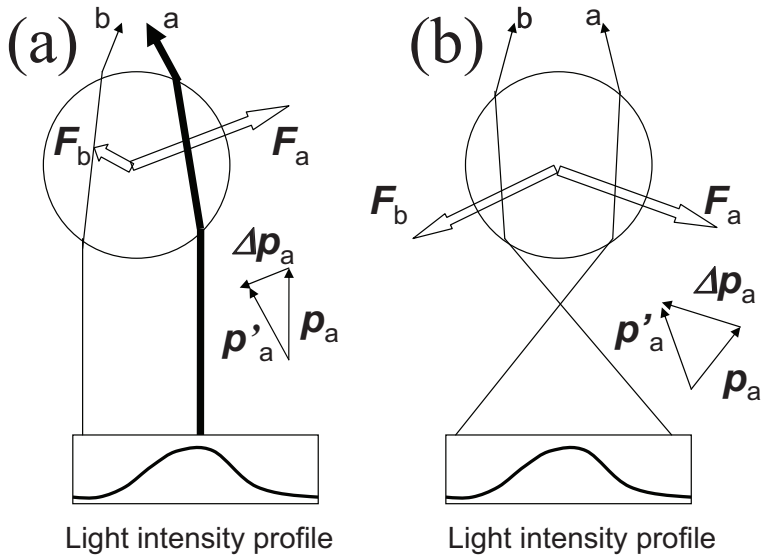


Figure 3.6: Sketch of the trapping of dielectric beads. A typical pair of rays a and b of the trapping beam get refracted and generate forces $F_a$ and $F_b$, which sum up to the restoring force $F$ in the transverse direction (a) and the axial direction (b).

its momentum by a equal but opposite amount, which result in a force imparted on the sphere. This force is in the direction of the sphere's momentum change, with a amplitude given by the rate of the momentum change. A simplified description of the trapping of dielectric particles is shown in Fig. 3.6. A typical pair of rays are refracted by a dielectric sphere, giving rise to a restoring force on the sphere directed back to the focus. The momentum change of the ray is proportional to the change in the direction of the entry and exit ray. Since no surface reflection is taken into account, the scattering force is not indicated. Roosen and coworkers have worked out the net force on a trapped sphere due to a single ray. [65]. It consists of the scattering force component $F_{scatt}$ and the gradient force component $F_{grad}$.

$$\mathbf{F}_{scatt} = \frac{n_1 P}{c}\left\{1 + R\cos 2\theta - \frac{T^2[\cos(2\theta - 2r) + R\cos 2\theta]}{1 + R^2 + 2R\cos 2r}\right\}\hat{\mathbf{k}} \tag{3.23}$$

$$\mathbf{F}_{grad} = \frac{n_1 P}{c}\left\{R\sin 2\theta - \frac{T^2[\sin(2\theta - 2r) + R\sin 2\theta]}{1 + R^2 + 2R\cos 2r}\right\}\hat{\mathbf{n}} \tag{3.24}$$

where $R$ and $T$ are the Fresnel reflection and transmission coefficients of the sphere surface [32], $\theta$ and $r$ are the angles of incidence and refraction, $\hat{\mathbf{k}}$ and $\hat{\mathbf{n}}$ are the unit vectors parallel and perpendicular to the direction of the incident ray respectively, and $P$ is power of the ray. The quantity $\frac{n_1 P}{c}$ is the incident momentum per second of a ray in a medium of refractive index $n_1$.

To obtain the total force by a highly converging beam of complex shape, one would need to carry out a vectorial summation of the scattering and gradient forces from the individual rays of the beam. Ashkin calculated the force on a sphere by a converging beam with Gaussian profile ($TEM_{00}$ mode) and with 'Donut' profile ($TEM_{01}$ mode) [5].

2. The Rayleigh regime ($d \ll \lambda$)

In this approximation, the sphere behaves like a point dipole and thus absorb and reradiate electromagnetic waves, giving rise to the scattering force [42].

$$\mathbf{F}_{scatt} = n_m \frac{\langle \mathbf{S} \rangle \sigma}{c} \tag{3.25}$$

Where

$$\sigma = \frac{8}{3}\pi (ka)^4 a^2 \left(\frac{m^2 - 1}{m^2 + 2}\right)^2 \tag{3.26}$$

is the scattering cross section of a sphere of radius $a$, $\langle \mathbf{S} \rangle$ is the time-averaged Poynting vector, $c$ is the speed of light in vacuum, $k = 2\pi n_m/\lambda$ is the wavenumber of the light, $n_m$ is the index of refraction of the medium and $m = n_p/n_m$ is the ratio of the

index of refraction of the sphere to the index of the medium. The scattering force is proportional to the light intensity and in the direction of the propagation of the beam.

When a dielectric sphere is placed in an inhomogeneous electric field, it feels a force due to the interaction of the induced dipole with the field intensity gradient. This force is denoted as the gradient force.

$$F_{grad} = \frac{\alpha}{2} \bigtriangledown \langle E^2 \rangle \tag{3.27}$$

where

$$\alpha = n_m^2 a^3 \left( \frac{m^2 - 1}{m^2 + 2} \right) \tag{3.28}$$

is the polarizability of the dielectric sphere [29]. The gradient force is proportional to the intensity gradient, and is directed towards the region of higher field strength (up the gradient) for $m > 1$.

For trapped objects of sizes comparable to the wavelength ($d \sim \lambda$), the two approaches mentioned above are not valid. Unfortunately, most biologically interesting samples, e.g., blood cell, yeast and bacteria as well as microspheres used in our interaction measurements fall into the intermediate size range ($0.1\lambda < d < 10\lambda$), which requires a complete theoretical treatment for their optical trapping. Nevertheless, the ray optic and simple dipole approach have revealed significant physical insights into the mechanisms of optical trapping.

From the above discussion, the optical force can be decomposed into a scattering force component and a gradient force component. The scattering force is in the propagation direction of the beam, pushing the sphere out of the objective focus, whereas the gradient force is directed up the light intensity gradient, pulling the

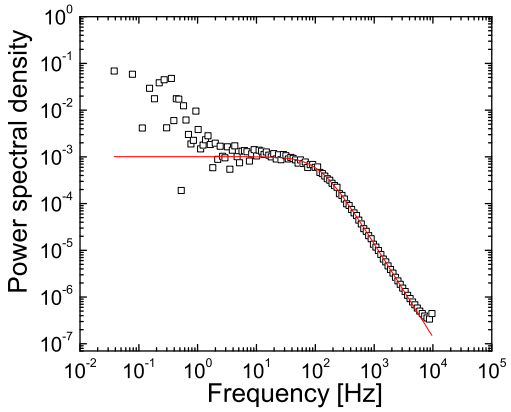


Figure 3.7: Power spectral density of a micron-sized colloidal bead trapped by laser tweezers in aqueous buffer.

sphere into the focal region. As a result of the balance between these two forces, the equilibrium position of the trapped sphere is slightly outside the focus on the optical axis. An efficient optical trapping requires the dominance of the gradient force over the scattering force. Since the extremal rays contribute more to the the gradient force than to the scattering force, the beam is usually expended to overfill the entrance pupil of the objective in order to increase the ratio of the gradient force to the scattering force. In our experiment, stable trapping of micron-sized beads is achieved when the position of 60% intensity of the Gaussian beam matches the edge of the objective entrance pupil.

### 3.5.2 Data Analysis

#### Stiffness Determination

In order to perform umbrella sampling, the biasing potential, or the trap stiffness, needs to be determined for all separation windows. A straightforward way to extract the trap stiffness is to determine the probability distribution of particle displacement,

which is related to the trapping potential by a Boltzmann relation

$$P(r) \propto \exp\left[\frac{-U(r)}{k_B T}\right] = \exp\left[\frac{-kr^2}{2k_B T}\right] \tag{3.29}$$

where $k_B$ is Boltzmann's constant, $T$ is the absolute temperature and $U(r)$ is the potential energy. For a harmonically bound particle, the distribution is a simple Gaussian. In practice, we construct the histograms of the displacements of two straptavidin-coated PS beads in their respective optical traps, and fit them to Gaussian distributions

$$g(x) = A_0 \exp\left[-\frac{(x - A_1)^2}{2A_2^2}\right] \tag{3.30}$$

The fitting parameters yield the trap stiffness $k$

$$k = \frac{k_B T}{A_2^2} \tag{3.31}$$

The assumption here is that the interaction between the plain beads is negligible.

Although experimentally convenient, using the method above is risky because the probability distribution of particle displacement can be influenced by noises from drifts, vibrations and insufficient statistics especially at the wings of histograms where counts are low. The other approach for force calibration is based on the power spectrum density (PSD) of the motion of a particle in an optical trap, which has a Lorentzian form

$$S_x(f) = \frac{k_B T}{\gamma \pi^2 (f_c^2 + f^2)} \tag{3.32}$$

where $\gamma = 6\pi\eta a$ is the friction coefficient of a sphere of radius $a$ in a medium of viscosity $\eta$, and $f_c$ is the corner frequency, related to the trap stiffness $k$ through $k = 2\pi\gamma f_c$. Fig. 3.7 is a typical power spectrum of a trapped bead. The PSD can be divided into three regimes. At higher frequencies (i.e. $f \gg f_c$), $S_x(f)$ falls off like

$1/f^2$, which indicates free diffusion. At intermediate frequencies (i.e. $10\,\text{Hz} \ll f \ll f_c$), the PSD levels off, which is characteristic of the confinement of the particle. At frequencies lower than 10 Hz, noises from drifts and vibrations are evident.

We trapped a PS bead in an optical trap and compare the trap stiffness obtained using both methods described above. From the probability distribution of the trapped bead, we have $k = \frac{k_B T}{A_2^2} = \frac{4.1\times10^{-21} N\cdot m}{0.50^2\times46.5^2\times10^{-18} m^2} = 7.58\times10^{-6} N/m$, where the calibration for the camera is 46.5 nm/pixel. Using the PSD method, the trap stiffness is calculated as $k = 2\pi\gamma f_c = 7.08\times10^{-6} N/m$, where the corner frequency $f_c = 117.4$ Hz. Thus the trap stiffness obtained from the probability distribution of the trapped bead is about 7% larger than the value measured with the PSD method.

### Digital Video Microscopy Tracking of Colloids

Detailed tracking procedure is described in [13] as well as at http://www.physics.emory.edu/∼weeks/idl/. Tracking routines written in IDL also can be found on the above website. Here we summarize the four main steps in locating colloidal particles in a time sequence of video images.

1. Convolving an image $A(x, y)$ with Gaussian kernels of support $2w + 1$ reduces noise and corrects for uneven illumination. The convolution kernel is

$$K(i,j) = \frac{1}{K_0}\left[\frac{1}{B}\exp\left(-\frac{i^2+j^2}{4\lambda_n^2}\right) - \frac{1}{(2w+1)^2}\right] \tag{3.33}$$

where the normalization constant $K_0 = \frac{1}{B}\left[\sum_{i=-w}^{w}\exp\left(-\frac{i^2}{2\lambda_n^2}\right)\right]^2 - \frac{B}{(2w+1)^2}$

2. Locate particles to within half a pixel by regional maximum selection.

3. A spatial resolution of 1/10 pixel can readily be achieved by calculating the brightness-weighted centroid of the pixels in a region around the locally brightest

pixel $(x, y)$ . The offset from $(x, y)$ to the brightness-weighted centroid is

$$\begin{pmatrix} \varepsilon_x \\ \varepsilon_y \end{pmatrix} = \frac{1}{m_0} \sum_{i^2+j^2 \leq w^2} \begin{pmatrix} i \\ j \end{pmatrix} A(x+i, y+j) \tag{3.34}$$

where $m_0 = \sum_{i^2+j^2 \leq w^2} A(x+i, y+j)$ is the integrated brightness of the sphere's image. The refined particle location is $(x_0, y_0) = (x+\varepsilon_x, y+\varepsilon_y)$. The refining process reiterate until both $|\varepsilon_x|$ and $|\varepsilon_y|$ are less than 0.5.

4. Check pixel-biasing by plotting a histogram of the fractional part of the x-coords of the particles. The histogram will be flat if the particles are randomly distributed. If there're two peaks in the histogram near 0 and 1, set the size parameter in 'feature' routine a little bigger. The brightness-radius plot is useful in distinguishing particles from noise. The artifacts can easily be eliminated by setting a brightness cutoff.

**On the Measurement of Center-to-Center Separation**

In the experiment, we equate the in-plane distance between the sphere images' brightness-weighted centroids to the center-center separation of the spheres. This approximation is valid for reasons below. The half-width of the Gaussian distribution 3.5.2 in the x-y plane is $\Delta x = \sqrt{2}A_2 = 33$ nm. The displacement out of the focal plane can be estimated to be $\Delta z = 3\Delta x = 99$ nm. Since the closest separation between spheres' centroid is about 2000 nm in our experiment, the ratio of the center-center separation and the in-plane distance can be estimated to be

$$\frac{\Delta r}{2000} = \sqrt{1 + (\frac{\Delta Z}{2000})^2} = 1.001 \tag{3.35}$$

The overlap of diffraction-broadened images of spheres can make it difficult to accurately measure their separation. The following tests were carried out to determine if such effects need to be taken into account in our analysis. The incident laser beam

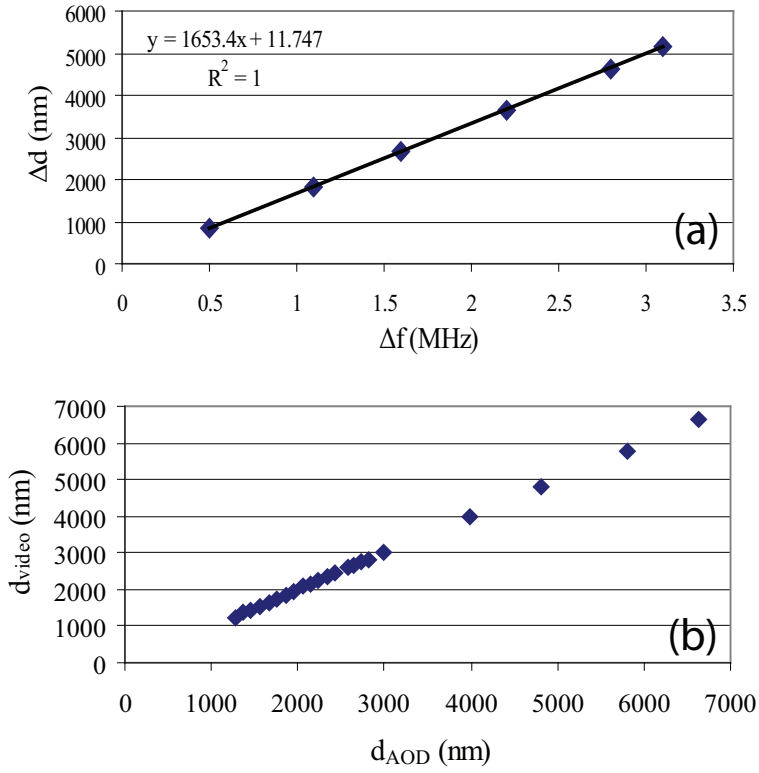


Figure 3.8: (a) Relation between the displacement of bead and the frequency of AOD. (b) Center-to-center separation between beads determined by video microcopy tracking and AOD. The linear relationship indicates that for the separation distances we are probing, the diffraction-broadened images of beads do not skew center-to-center separation measurements using video tracking.

experiences a Bragg diffraction at acoustic wavefronts in an acousto-optic device. The first order diffracted beam leaves the sound field at the Bragg angle

$$\theta_B = \frac{\lambda}{2\Lambda} = \frac{\lambda}{2v} f = \frac{\Delta d}{r} \tag{3.36}$$

$$\Delta d = \frac{r\lambda}{2v} f = Cf \tag{3.37}$$

where $\theta_B$ is the Bragg angle, $\Lambda$, v and f are the acoustic wavelength, velocity and frequency respectively. The displacement of a bead in the focal plane $\Delta d$ is plotted as a function of AOD frequency $f$ in Fig. 3.8(a). The calibration factor for the AOD was determined to be 1658.5 nm/Mhz. We then trapped two beads and varied their separation by moving one of the beads towards the other which is fixed. The separation between the beads determined by video microscopy tracking and AOD frequency are linear with each other Fig. 3.8(b), which implies the diffraction effect can be ignored in the separation measurements.

# Chapter 4

# On the Biochemical Synthesis of Rod-Coil Particles

## 4.1 Introduction

Hard rod-like particles are shown to transition from isotropic phase to nematic phase as the number density of rods increases [61]. In the mixtures of hard spheres and rods the spheres stabilize the smectic phase of rods by intercalating between smectic layers [51]. In this chapter we propose to modify the hard rod by attaching a polymeric coil to one end of the rod, creating a rod-coil particle. Such rod-like particles are the hard-particle analogs of molecular amphiphiles. Several theories [21, 82] and simulations [60, 54, 34, 28] have been developed for rod-coils whose interactions are purely entropic. In the limit of vanishing rod diameter, the pure rod solution shows isotropic, nematic and smectic phases. It is predicted that as the size of coil increases the nematic phase becomes destabilized and the smectic phase gets enhanced.

We select the M13 virus as the rod component of rod-coil for two reasons. Firstly, filamentous phages, fd and M13, are model systems of hard colloidal rods, whose

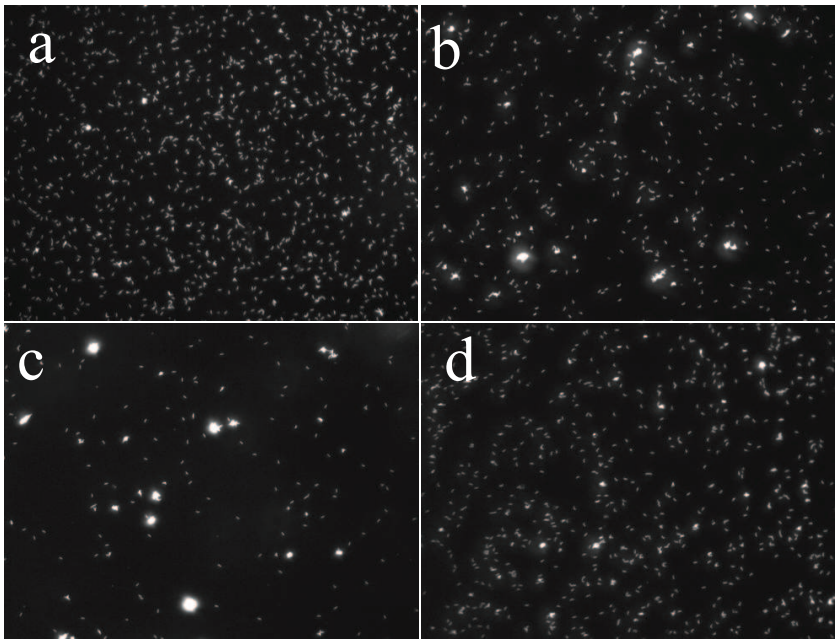


Figure 4.1: Reaction of streptavidin (SA) and M13-C7C at varying stoichiometric ratios, $n_{\mathrm{SA}}/n_{\mathrm{M13}}$ = (a) 0; (b) 1/6; (c) 10/6; (d) 1000/6; The majority of phage particles are crosslinked by streptavidin when the molar ratio of SA to M13 is close to one.

phase behavior have been mapped out experimentally [18]. Secondly, the Belcher group demonstrated that using phage display technique M13 virus can be genetically engineered to specifically bind to inorganic materials [53]. In what follows, we describe our efforts in attaching streptavidin-coated beads and plasmid DNA to genetically engineered M13 phage.

## 4.2 Materials and Methods

### 4.2.1 A Simple Assay to Verify the Display of Cysteines on M13-C7C

M13-C7C bacteriophage is produced and labeled with Alexa Fluor® 488 carboxylic acid succinimidyl ester (Molecular Probes) following the protocols presented in appendix A.4.1. A simple assay is carried out to verify the unimpaired functionalities of the cysteine groups on pIII proteins. 230 $\mu$l of 8.8 mg/ml M13-C7C was reduced with 2 $\mu$l of 0.18 mg/ml TCEP (Tris(2-carboxyethyl)phosphine) for 5 minutes, and then mixed with 2 $\mu$l of 19 mM maleimide-$PEO_2$-biotin (Pierce, Rockford, IL) for 1 h in 20 mM phosphate buffer at $p$H = 7.0. The phage solution was dialyzed extensively against phosphate buffer to remove excess biotin, and subsequently incubated with 10 mg/ml solutions of streptavidin (Pierce) in varying molar ratios for 30 minutes. Samples from each reaction are observed on a fluorescent microscope. Since each streptavidin molecule has four active binding sites for biotin groups, the reaction product is dependant on the stoichiometry ratio of phages and streptavidin molecules. A small amount of streptavidin leads to multiple phages linked together, while a molar excess of streptavidin produces individual M13-SA complexes (Fig. 4.1).

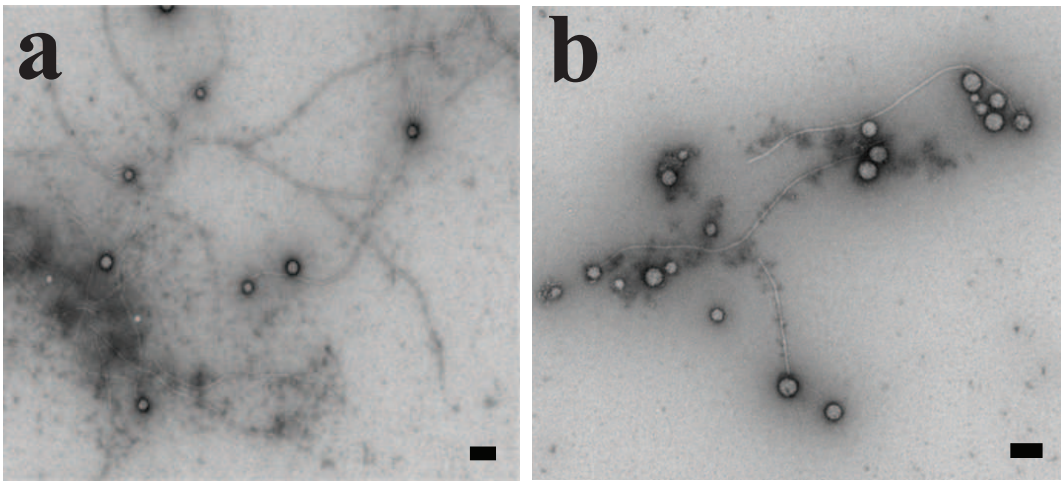


Figure 4.2: Electron micrograph of 40 nm SA-coated PS spheres attached to M13 viruses. The molar ratio of sphere and rod is (a) 1; (b) 10.

### 4.2.2 Creating Rod-Coil Using Streptavidin-Coated Beads

We attempt to create rod-sphere particle following protocols similar to those described in Chapter 3. To synthesize colloidal stars, the molar ratio of virus to PS sphere is approximately 1000, whereas we use molar excess amount of PS sphere relative to virus to create rod-coil particle. Biotinlyted M13 viruses are mixed with streptavidin-coated polystyrene beads of diameter $d = 40$ nm (Bangs Laboratories, Fishers, IN). As shown in Fig. 4.2, a significant number of rods are not bound to any spheres.

We speculate the failure of reaction could be due to the unbound streptavidin molecules, which are detached from the surfaces of SA-coated spheres. The SA-coated spheres are not subject to purification prior to conjugation with virus, because it's difficult to separate free streptavidin from SA-coated spheres. Therefore the biotin groups on phages could be saturated by free streptavidin before reacting with SA-coated spheres, which leads to the low efficiency of sphere-rod conjugation.

### 4.2.3 Creating Rod-Coil Using Plasmid DNA

There are two advantages in attaching dsDNA to the phage to create rod-coil particle. One is that DNA is highly charged macromolecule, much more stable than polystyrene beads in aqueous solution. The other is that the size of the coil can be tailored by selecting different combinations of plasmid DNA and restriction enzyme. While polymerase chain reaction (PCR) enables one to create dsDNA up to thousands of base pairs [41], it's a challenge to produce milligrams of dsDNA this way, which will be needed in our phase behavior studies. In what follows, we describe our efforts in conjugating plasmid DNA to M13 virus. Although it's straightforward to produce large quantities of plasmid DNA using standard molecular cloning technique, it's tricky to functionalize the DNA and link it to virus. We have only achieved limited success.

We start with solutions of 15 base-pair single-stranded DNA, one end of which is functionalized with an amine group (Integrated DNA Technologies, Coralville, IA). The sequence is designed to be 5'-GAGGGATTATTGTTA-3'. We mix 0.2 mM oligonucleotide with 6 mM Sulfo-SMCC (Sulfosuccinimidyl 4-[N-maleimidomethyl]-cyclohexane-1-carboxylate, Pierce, Rockford, IL) in 500 $\mu$l phosphate buffer at $p$H = 8.0 for 1h (reaction I in Fig. 4.3). The solution is analyzed with a mass spectrometer (Voyager, Applied Biosystems, Carlsbad, CA), operated in the linear mode, in order to estimate the efficiency of maleimide-activation. Fig. 4.4 shows that 65 % ssDNA is conjugated with maleimide group. The reaction mixture is run through a Sephadex G-25 column (NAP 5, Amersham Biosciences, Sweden) to eliminate the excess crosslinkers. Note that we use $p$H = 7.0 buffer to elute the column, in order to minimize the unwanted reaction of maleimide groups on ssDNA and amine groups on coat proteins of M13. In the mean time, 10 mg/ml solution of M13-C7C is reduced with 1.8 mg/ml TCEP in 1 ml phosphate buffer ($p$H = 7.0) for 5 minutes. We then

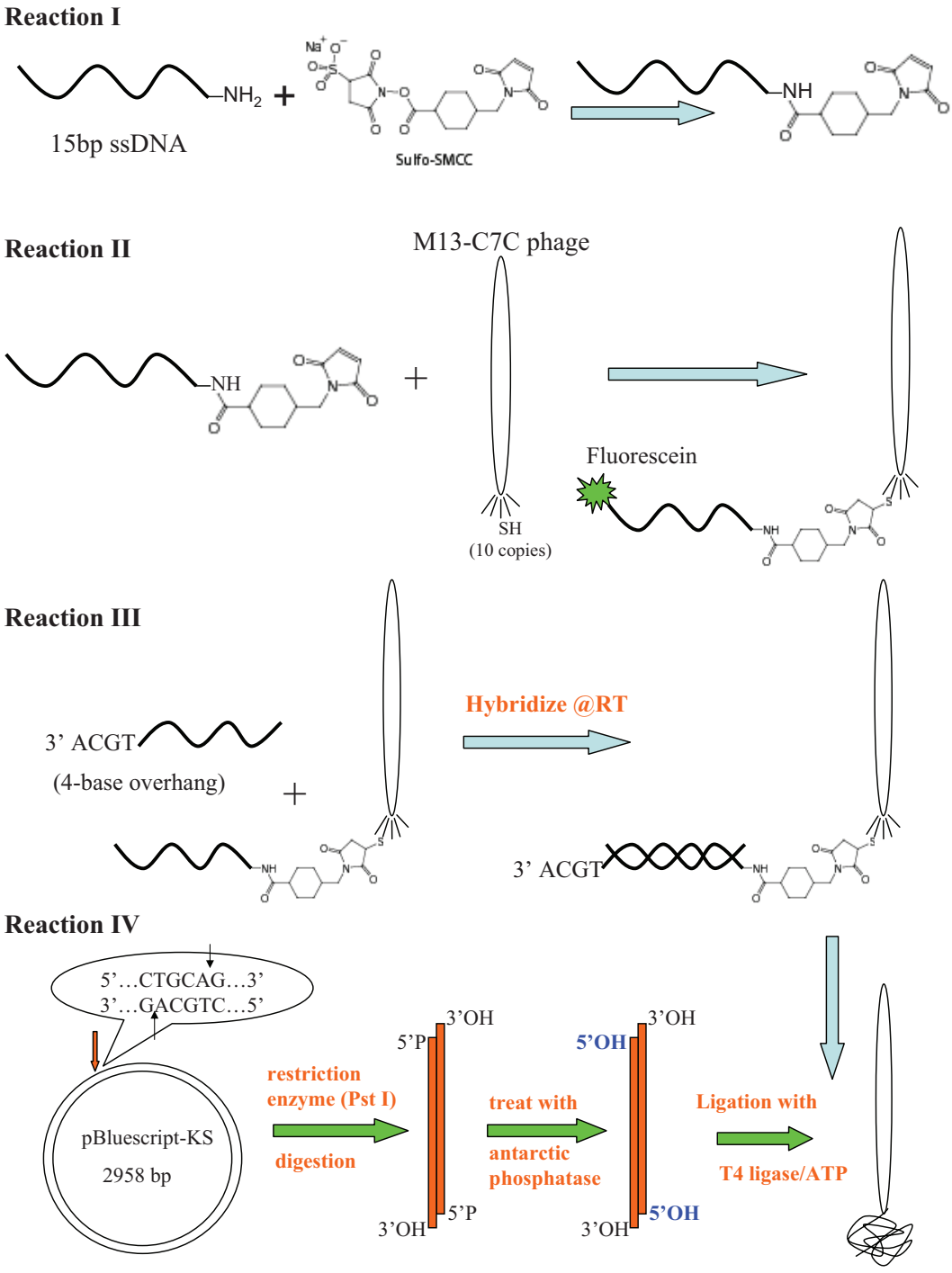


Figure 4.3: Schematic of synthesizing rod-coil particle from M13 phage and plasmid DNA.

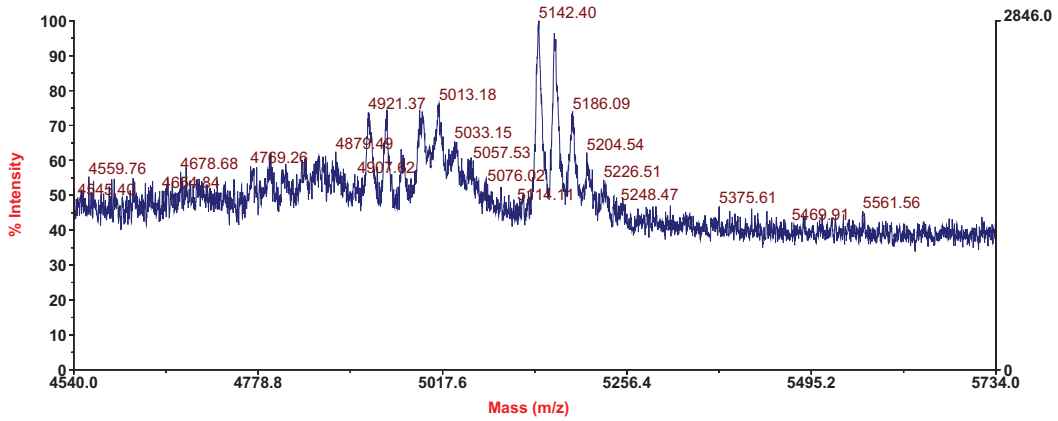


Figure 4.4: Mass Spectrum of the reaction after 2 hours. The left peaks correspond to the reactant ssDNA(15bp MW=4921). The right ones correspond to maleimide activated ssDNA. About 65% ssDNA have been activated. The periodic mass increases of 22 are due to sodium ion adducts.

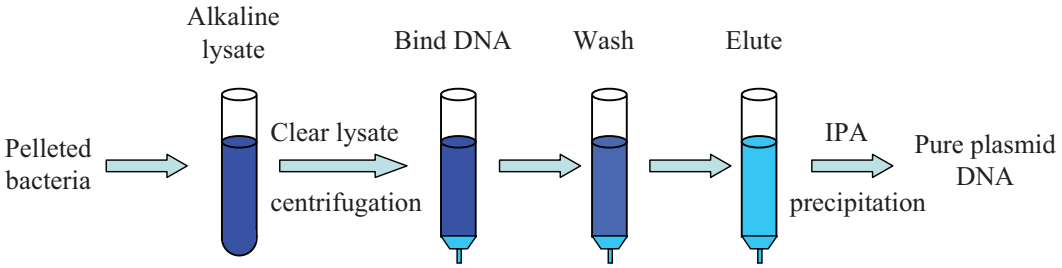


Figure 4.5: Schematic of the production and purification processes of plasmid DNA.

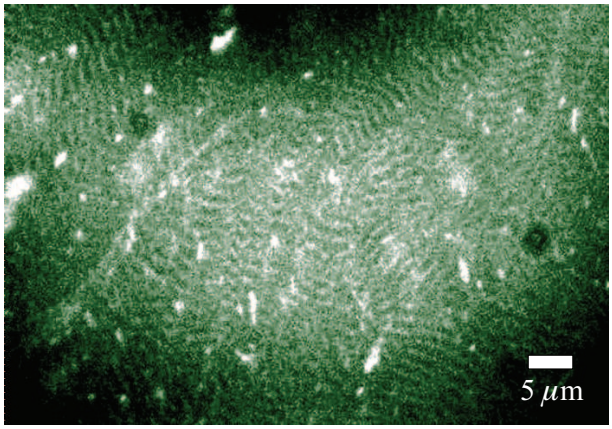


Figure 4.6: Fluorescent image of M13-oligo-dye solution in a smectic phase. The fluorescein molecules attached at the end of rods intercalate between smectic layers.

mix the maleimide-activated ssDNA with M13-C7C solution in $p$H = 7.0 phosphate buffer for 2 hours (reaction II in Fig. 4.3). The excess ssDNA can be removed from the virus solution by repeated ultracentrifugation at 170,000 g.

The successful linkage of DNA molecules to phages can be confirmed as follows. We start with solutions of 15-bp ssDNA with one end functionalized with amine and the other attached to a fluorescein molecule. Following the same procedure as outlined in the previous paragraph, we end up with DNA-M13 complex with fluorescent labeling on only one end of the rod. We then concentrate the phage solution by spinning at 250,000 g, and dissolve the pellet with 10 mM phosphate buffer. The sample is loaded into a chamber with a thickness of about 10 $\mu$m, and observed with fluorescent microscopy as shown in Fig. 4.6. The periodic stripes, corresponding to layers of fluorescein molecules, indicate there is little nonspecific binding of ssDNA to viruses.

The M13-ssDNA complexes are mixed with solutions of 19-bp ssDNA, the sequence of which is designed such that 15 bases are complimentary to the ssDNA on M13 and 4 bases are complimentary to the overhang of plasmid DNA, which will be added subsequently. The molar ratio of fd-ssDNA to complimentary ssDNA is one to three. The hybridization lasts for 30 minutes at 25°C. After removing the excess DNA molecules, we have M13 viruses linked to 15 bp dsDNA with 4 bp overhang (reaction III in Fig. 4.3).

In the final step of synthesis (reaction IV in Fig. 4.3), we need to link a dsDNA of several kilobases length to the oligo on the M13 virus. We have produced and purified dsDNA from pBluescript-KS, a 2958 bp plasmid (New England Biolabs, Beverly, MA), using a commercial plasmid purification kit (QIAGEN, Valencia, CA). The procedure is based on alkaline lysis of bacteria cells and binding of plasmid DNA to anion-exchange resin. It is shown schematically in Fig. 4.5.

The following is our failed attempt to attach the plasmid dsDNA to the oligo through ligation. The plasmid DNA is first linearized with restriction enzyme Pst I. The radius of gyration of dsDNA is $R_g \sim \sqrt{N_{\rm bp}} 2.5$ [nm], corresponding to a coil of about 100 nm in radius. The restriction enzyme digestion yields a linear strand of dsDNA with a four-base overhang (TGCA), and the reaction has a nearly 100% efficiency as can be monitored by gel electrophoresis. 200 units of Antarctic Phosphatase (NEB) is used to dephosphorylate 200 $\mu$g of the plasmid DNA. Since phosphatase-treated fragments lack the 5' phosphoryl termini required by ligases, they cannot self-ligate [52]. The dephosphorylated linear strand of plasmid is then joined by T4 Ligase (NEB) to oligo on the M13 virus. After purified with ultracentrifugation, the phage particles, metal-shadowed and negatively stained, are examined by a transmission electron microscope. No plasmid DNA is seen attached to the phage (EM pictures not shown).

## 4.3 Discussion

The failure of attaching plasmid DNA to M13 could be attributed to the following factors. First, ligation is inherently inefficient; Second, for a successful ligation to happen, the cohesive end termini have to hybridize first, in order for ligase to come in to seal up the phosphate backbone of dsDNA. However since there are only four complimentary base pairs present and the diffusion constants of phage and plasmid are both small, it would be difficult to establish linkage between cohesive ends in the first place.

To avoid the difficulty of joining two slowly diffusing objects by ligation, we propose a slight modification to the procedure used. After linearized by restriction enzyme Pst I, the plasmid, pBluescript-KS, is ligated to a 54-bp oligo to create kilobase pair length strand of dsDNA with 50-bp overhang. The sequence of the 54-mer will be checked for secondary structures using online tools. The oligos will be added a hundred fold in excess to boost the efficiency of the ligation. The unreacted oligos is separated from dsDNA by repeated centrifugation in a centrifugal filter with a molecular weight cutoff of 100,000 (Microcon YM-100, Millipore, MA). We carry out reaction I and II as mentioned before, except to replace the 15-bp ssDNA with a 50-bp ssDNA, which is complimentary to the overhang on the plasmid DNA. After the incubation of the dsDNA and M13-ssDNA at room temperature, hybridization occurs between oligo on the virus and overhang on the dsDNA, and rod-coil forms.

# Chapter 5

# Electric-Field-Induced Chaining of Colloidal Particles

**Note:** This project has been a collective effort in our lab for many years. For the sake of completeness, works by other people have been included in this thesis. The equilibrium theory was first proposed by Prof. Peter Jordan and later extended to account for mutual polarization by Prof. Seth Fraden. I further modified it by numerically solving the pair partition function. Part of the theory section was taken from Prof. Seth Fraden's thesis. San Lin made the measurements, and wrote most of the experimental section. Noah Ribeck calculated the E-field distribution in the sample layer using the finite element method. I constructed a Langevin dynamic simulation to compare with the theory and the experiment.

## 5.1 Introduction

Colloidal particles subjected to an applied electric field experience dipolar attraction due to particle polarization. In the presence of strong fields, dilute suspensions typically aggregated into chain-like structures, while concentrated suspensions form a dense complex network. Such concentrated suspensions, called electrorheological

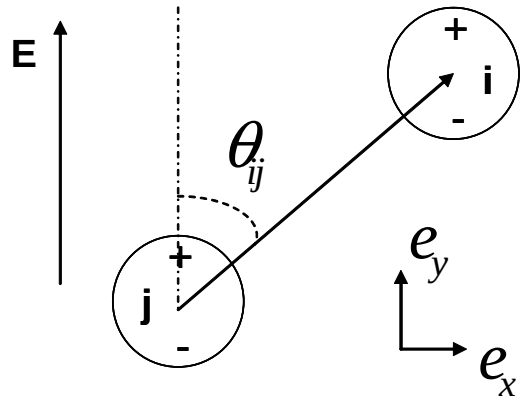


Figure 5.1: Computational geometry.

fluids, can produce drastic changes in rheological properties, which potentially can lead to industrial applications in clutches, brakes and vibration-control systems [74].

We present quantitative experimental studies of dilute, aqueous suspensions of mono-disperse, micrometer-size, polystyrene spheres, confined in a thin layer where uniform, weak high frequency AC electric fields are applied. Under these conditions, the spheres form isolated pearl chains, oriented along the field, and the aggregation is reversible in that the chains formed can break up because the thermal energy of the particles is comparable with the field-induced interparticle binding energy. After a transient period, a dynamic equilibrium among chains is reached with a time-independent chain length distribution. We compare the average chain size and chain length distribution to an equilibrium statistical mechanical theory for chain formation in dilute suspensions and a Langevin molecular dynamic simulation, in which the interaction potential includes dipole-dipole attraction and electrostatic repulsion. There is a reasonable agreement between the theory, simulation and experiment.

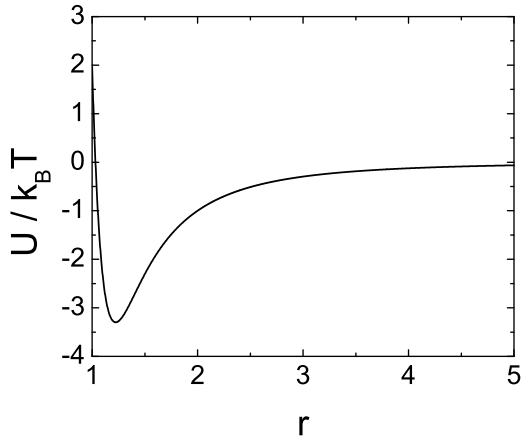


Figure 5.2: Theoretical pair potential for aligned dipoles ($\theta = 0$). $\frac{U}{k_B T} = \frac{-2\lambda}{r^3} + \eta e^{-\kappa(r-1)}$ where $\lambda = 4$, $\eta = 10$ and $\kappa = 10$.

## 5.2 Particle Interaction

A single sphere distorts a uniform applied electric field in such a way that the field outside the sphere can be described as the superposition of the nondistorted field and the field due to a point dipole located in the the center of the sphere with dipole moment

$$\boldsymbol{\mu} = \epsilon_w^{'} a^3 \left[ \frac{\epsilon_p - \epsilon_w}{\epsilon_p + 2\epsilon_w} \right] \mathbf{E} \tag{5.1}$$

with $\epsilon_w$, $\epsilon_p$ the complex dielectric constants of water and the particle, where $\epsilon = \epsilon^{'} + i\epsilon^{"}$, $a$ the radius of the sphere, and $E$ the electric field [69, 63]. All formulas, unless otherwise noted are in c.g.s unites. Two spheres separated at large distances interact primarily through a dipole-dipole potential with the interaction energy given by

$$U_{\text{dip}} = \frac{\mu^2(1 - 3\cos^2\theta)}{\epsilon_w^{'} r^3} \tag{5.2}$$

where $r$ is the distance between centers of the spheres and $\theta$ is the angle between the line connecting the centers and the external field. Thus two spheres attract each other when $\theta = 0°$ and repel each other when $\theta = 90°$.

The polystyrene is negatively charged with a surface charge density of $\sim 1\text{elec}/1000\text{Å}^2$ [7] and surface potential of $\sim 30\text{mV}$ [49]. The attractive dipole potential brings the particles close to each other, but even with the salt present in the solution, the short range repulsion is strong enough to prevent the spheres from irreversibly sticking. The potential energy of repulsion [83] is given by

$$U_{\text{rep}} = \frac{1}{4}\epsilon_w d\psi_0^2 e^{-\kappa d\xi} \tag{5.3}$$

with the Debye screening length, $\kappa^{-1} = 3\text{Å}/\sqrt{M}$, with M the molarity of a 1-1 electrolyte.

Combining the dipole attraction with the electrostatic repulsion yields

$$\frac{U(r,\theta)}{k_B T} = \lambda \frac{(1 - 3\cos^2\theta)}{(1+\xi)^3} + \eta e^{-\kappa d\xi} \tag{5.4}$$

where $r = d(1+\xi)$, $k_B T$ is the thermal energy, $\lambda = \mu^2/\epsilon_w d^3 k_{\text{B}} T$ and $\eta = \epsilon_w d\psi_0^2/4$. The potential energy is shown in Fig. 5.2. The minimum of the potential energy is no longer at hard-sphere contact with a magnitude significantly lower than the dipole contact energy, $-2\lambda k_{\text{B}} T$. Typically with $\eta = 10$, $\kappa d = 10$, and $\lambda$ ranging from 4 to 10, the potential energy minimum varies from $-3.3$ to $-11.4 k_{\text{B}} T$, while the dipole contact energy is $-8$ to $-20 k_{\text{B}} T$.

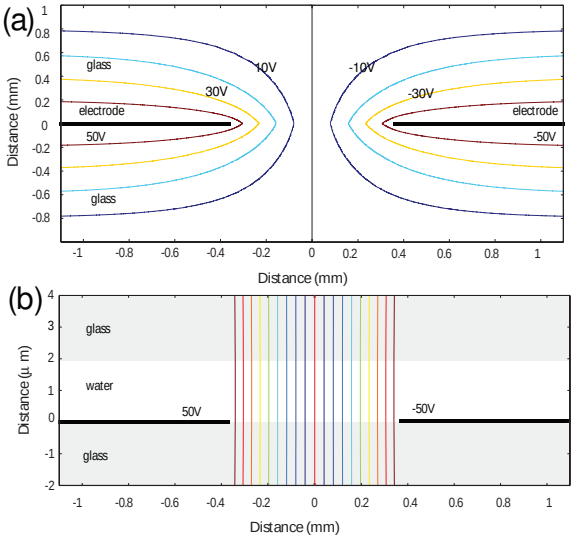


Figure 5.3: The equal-potential contours in the sample holder (a) and in the sample layer with a thickness of $1\mu m$ (b) at frequency 500kHz calculated using the finite element method.

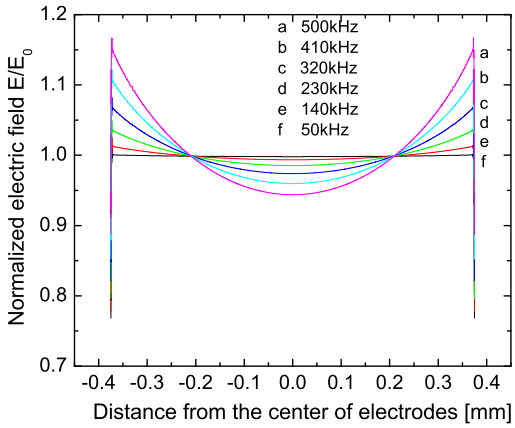


Figure 5.4: The electric field strength across the gap between electrodes at different frequencies.

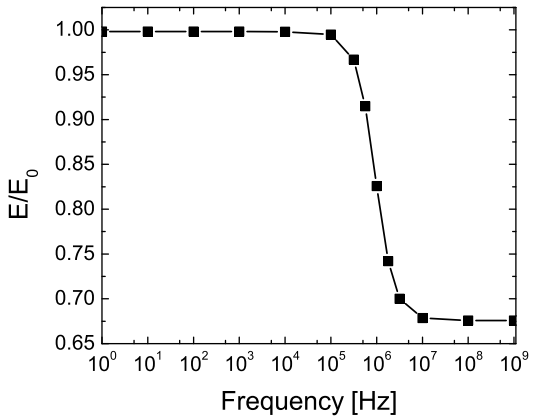


Figure 5.5: The electric field strength at the center of electrodes vs frequency.

## 5.3 Equilibrium Model for Chain Formation

As described above, at low external electric field strengths and high frequency, we observe the assembling of monomers into chains of particles that repeatedly break into shorter chains and reassemble, so that a dynamic equilibrium among chain lengths is reached. The energy of interaction between two spheres is of the order of 10 $k_BT$ before we observe significant clustering. Given this large energy difference between a chain of $n$ particles and a chain of $n+1$ particles, it was argued by Jordan [38] that it is reasonable to speak of each $n$-mer as being a chemically distinct species and to relate the number densities of $n$-mer by using the law of mass action

$$\frac{\rho_n}{\rho_1^n} = \frac{(q_n/V)}{(q_1/V)^n} \tag{5.5}$$

where $q_i$ and $\rho_i$ are the partition function and number density of a chain consisting of $i$ particles. The partition function of a single sphere is

$$q_1 = V/\Lambda^3 \tag{5.6}$$

with $\Lambda = h/\sqrt{2\pi m k_B T}$, the thermal wavelength. The conservation of total number of spheres is expressed by

$$\rho = \sum_{n=1}^{\infty} n\rho_n \tag{5.7}$$

The first step in calculating the partition function for a $n$-mer is to determine the intramolecular potential. The ratio of potential energy to thermal energy was introduced in Eq (5.4). In previous studies on strong dipolar interactions of hard particles[38], the relevant particle configurations are highly localized, and the pair interaction potential was approximated by expanding about the potential energy minimum. It was argued by Gast [1] that this expansion is not useful for the present interaction potential, since the energy minimum moves and becomes quite broad as $\lambda$ is varied. The potential energy minimum is given implicitly by

$$\frac{dU}{dr} \mid_{r=d_{\min}} = 0 \tag{5.8}$$

Detailed calculations of the chain partition function, $q_n$, have been carried out for hard spheres with dipoles[38]. In order to account for the electrostatic repulsive energy, the dimer partition function has been numerically solved to correct for $q_n$ with the substitution $\lambda \rightarrow \lambda' = \lambda/d_{\min}^3$, where $d_{\min}$ is determined from Eq. (5.8) [1]. The calculated partition functions yield the number density of all chain lengths.

Experimentally we measure the distribution of chain lengths, $\rho_n$. Examples of the theoretical distribution for several values of the electric field are shown in Fig. 5.12. From the distribution it is easy to calculate the average chain length, which is given by

$$\overline{n} = \frac{\sum n\rho_n}{\sum \rho_n} \tag{5.9}$$

To compare with the distribution function predicted from Jordan/Gast theory, we consider the linear aggregation model with constant binding energy. Derived from

the law of mass action, the distribution function is $X_n/n = \{X_1 \exp[(\mu_1^0 - \mu_n^0)/kT]\}^n$ [36], where $\mu_n^0$ is the mean interaction free energy per molecule in $n$-mers ,and $X_n$ the concentration of particles in $n$-mers.

In the linear aggregation model we consider two simple forms of binding energy. The first form of binding energy for each particle in a $n$-mer is from the nearest neighbors. Thus the mean interaction free energy per molecule in $n$-mers, $\mu_n^0$, is $-\frac{(n-1)}{n} 2\lambda' kT$. The second form of binding energy considers contributions from both the nearest and next nearest neighbors. In this case, the mean interaction free energy per molecule in $n$-mers is $-\frac{(n-1)}{n} 2\lambda' kT - \frac{(n-2)}{8n} 2\lambda' kT$. In a semi-log plot (Fig. 5.14), we fit the two forms of the linear aggregation model to the linear part of the experimental chain length distribution ($5 \leq n \leq 20$), and fit the Jordan model and the Jordan/Gast model to the entire experimental distribution ($1 \leq n \leq 20$). Experimentally, the distribution shows a gradual increase of slope for short chains, which is a consequence of the long range of the dipole-dipole interaction; each particle feels the attraction of all its neighbors so the binding per particle increases with chain length. Both the Jordan and Jordan/Gast models give better fits to the experiment than the linear aggregation model, because they include dipole-dipole interactions of all range. Moreover, the Jordan/Gast model fits the best due to its incorporation of short range electrostatic repulsion. As the chains grow longer, the binding energy for the addition of a monomer to a chain approaches a constant, and the distribution becomes exponential. We plot the slope of $\log(\rho_n/\rho)$ as a function of $\lambda$ in Fig. 5.15. In the Jordan model the slope was taken when the distribution becomes exponential.

The electric field produced by a single dipole in the radial direction is

$$E_r = \frac{2\mu \cos\theta}{\epsilon_w' r^3} = 2 \left[ \frac{\epsilon_p - \epsilon_w}{\epsilon_p + 2\epsilon_w} \right] \left( \frac{a}{r} \right)^3 E \cos\theta \tag{5.10}$$

At the point $r = 2a$, $\theta = 0$ the electric field due to one sphere, in the limit $\epsilon_w >> \epsilon_p$, is $-E/8$. A second sphere placed at this point will be exposed to a weaker field due to the presence of the first sphere. The energy of interaction [69] of two charged spheres in an uniform external electric field with a first order correction due to mutual polarization is given by

$$\frac{U(r,\theta)}{k_B T} = \lambda \left[ \frac{(1 - 3\cos^2\theta)}{(1+\xi)^3} - \delta \frac{(1 + 3\cos^2\theta)}{(1+\xi)^6} \right] + \eta e^{-\kappa d \xi} \tag{5.11}$$

with $\delta = \frac{1}{8} Re(\epsilon_p - \epsilon_w)/(\epsilon_p + 2\epsilon_w)$, where $Re$ is the real part of the quantity enclosed in the brackets.

To take into account the effect of mutual polarization, we consider the simple case where n spheres are touching each other in a rigid $n$-mer chain. We expand the dipolar energy term in Eq. (5.11)) about its equilibrium position to the first order terms in $\xi$ and $\theta^2$:

$$\frac{U_{i,i+1}}{k_B T} = -\lambda \left[ 2 + 4\delta - \xi_i(6 + 24\delta) - \theta_i^2(3 + 3\delta) \right] + \eta e^{-\kappa d \xi} \tag{5.12}$$

For monomer, there is no mutual polarization. For spheres at the two ends of a chain, this modification of electric field reduces the binding energy of a $n$-mer chain by a factor of $1 + 2\delta = 0.885$, and for spheres in the middle the reduction factor is 0.77. For short chains , *e.g.*, dimers, the effect of the end spheres is significant, and the reduction factor of the binding energy is not as much as that for longer chains. But for simplicity, we multiply a factor of 0.77 universally to $\lambda$ for all chains.

Using the finite element method from Matlab, we calculated the potential and electric field in the sample. The E-field is very well confined in the sample layer, $2\mu m$ in thickness (Fig. 5.3). At the center of the electrodes where the data was taken, the field strength decreases with increasing frequency (Fig. 5.4 and 5.5).

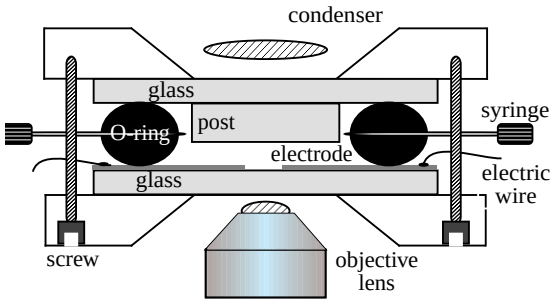


Figure 5.6: A sketch of the sample holder.

In order to compare theory and simulation to experiment, we made three corrections to the experimental $\lambda$ value calculated from the definition $\lambda = \mu^2/\epsilon_w d^3 k_{\rm B}T$ where $\boldsymbol{\mu} = \epsilon_w^{'} a^3 \left[\frac{\epsilon_p - \epsilon_w}{\epsilon_p + 2\epsilon_w}\right] \mathbf{E}$ to account for (1) the effect of short range repulsion, (2) the mutual polarization, and (3) the frequency dependence of E-field strength.

## 5.4 Experimental Conditions

In this experiment, we studied dilute aqueous suspension of monodisperse polystyrene spheres with diameter, $d = 1.27\,\mu$m. As sketched in Fig. 5.6, the sample was confined in a thin layer by two parallel glass plates, so that all the spheres were in the focal plane of the microscope. The distance between the glass plates is from $1.3\,\mu$m to $2.6\,\mu$m. On one of the glass plates, there were a pair of parallel electrodes with a separation of 0.75mm, etched out of a layer of indium-tin-oxide (ITO) coating on the glass plate. A non-uniform AC electric field was applied across the gap between the electrodes where the spheres were confined.

Polystyrene spheres are dielectric holes in water because the real dielectric constant of polystyrene, $\epsilon_p'$, is 2.5, much smaller than that of water. For water, the real dielectric constant, $\epsilon_w'$, is 78. The applied electric field induces a dipole moment in each sphere. When two spheres are close to each other, higher order moments appear

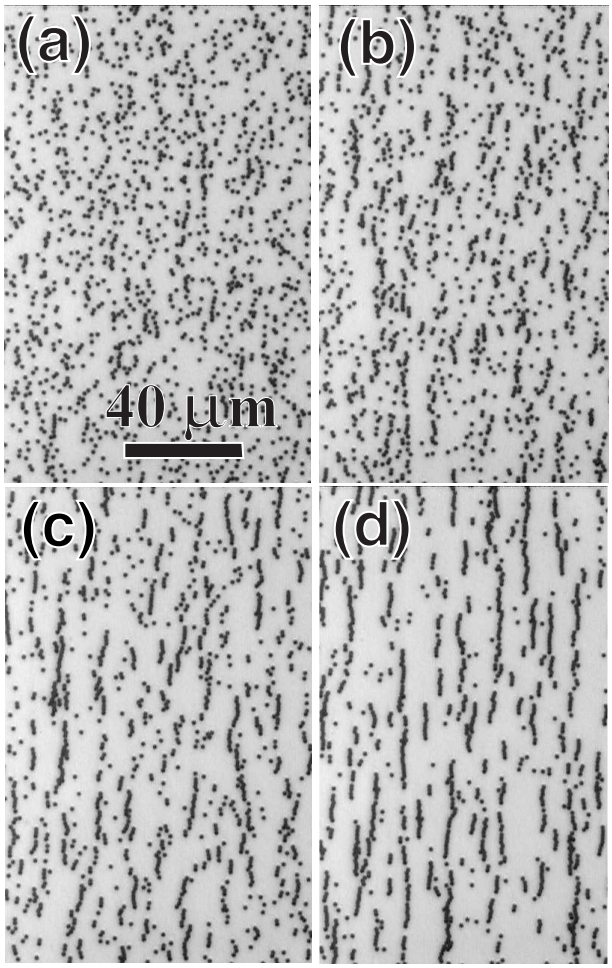


Figure 5.7: The digitized images (640 pixels(H) $\times$ 480 pixels(V), 256 gray levels) of aqueous suspension of polystyrene spheres confined in a thin layer with the rms of the applied electric field strength $E_0$ (a) $1.4 \times 10^4$ V/m (b) $1.9 \times 10^4$ V/m (c) $2.1 \times 10^4$ V/m (d) $2.4 \times 10^4$ V/m at frequency $f = 230$ kHz.

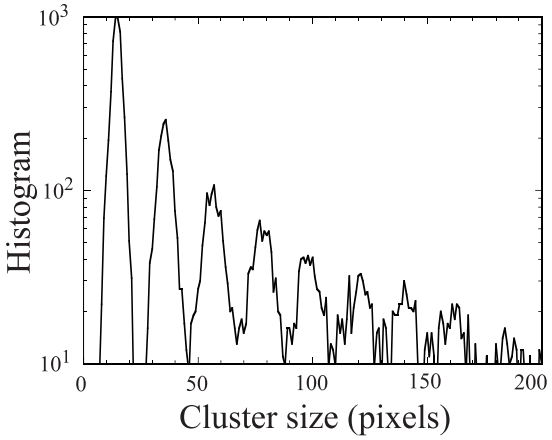


Figure 5.8: The histogram of cluster sizes obtained from analyzing 56 images.

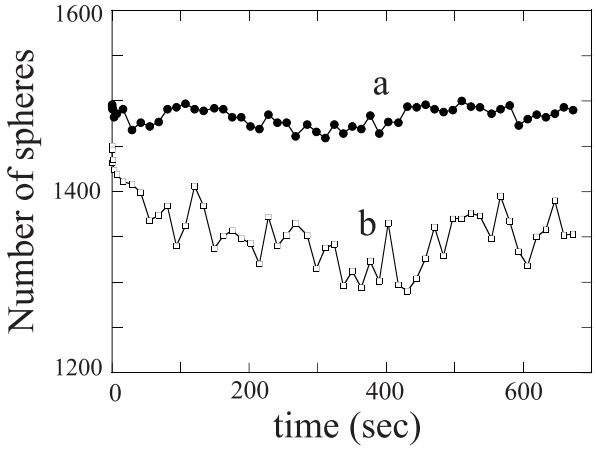


Figure 5.9: The total number of spheres in an image (•) and the number of spheres in chains that are completely inside an image (□).

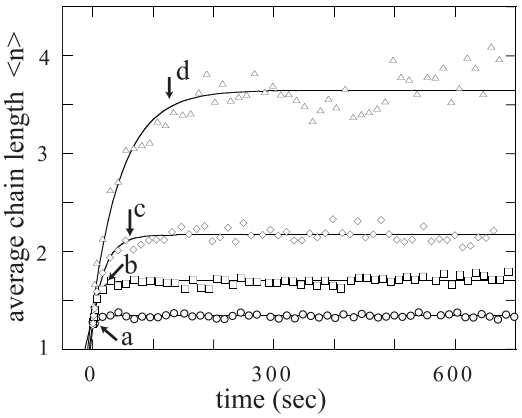


Figure 5.10: The average chain length in each video image evolves with time at different field strengths. The rms values of the field strengths are ($\circ$) $E_0 = 1.4 \times 10^4\,(\mathrm{V/m})$, ($\square$) $E_0 = 1.9 \times 10^4\,(\mathrm{V/m})$, ($\Diamond$) $E_0 = 2.1 \times 10^4\,(\mathrm{V/m})$, and ($\triangle$) $E_0 = 2.4 \times 10^4\,(\mathrm{V/m})$ respectively. The relaxation time constants, $\tau$, are obtained by fitting $\langle n(t)\rangle = \langle n(\infty)\rangle + (\langle n(0)\rangle - \langle n(\infty)\rangle)\exp(-t/\tau)$, indicated by the solid lines, to the data. The frequencies of the applied electric fields are all 230 kHz.

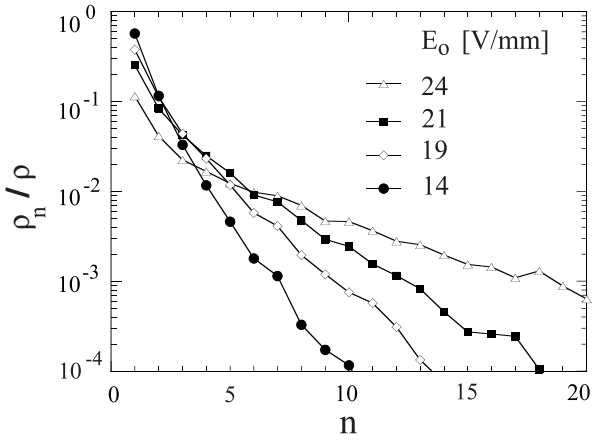


Figure 5.11: The chain length distribution at different field strengths. $\rho_n$ is the number density of $n$-mer, and $\rho$ is the number density of total spheres. The volume fractions $\phi$ are estimated to be 4%.

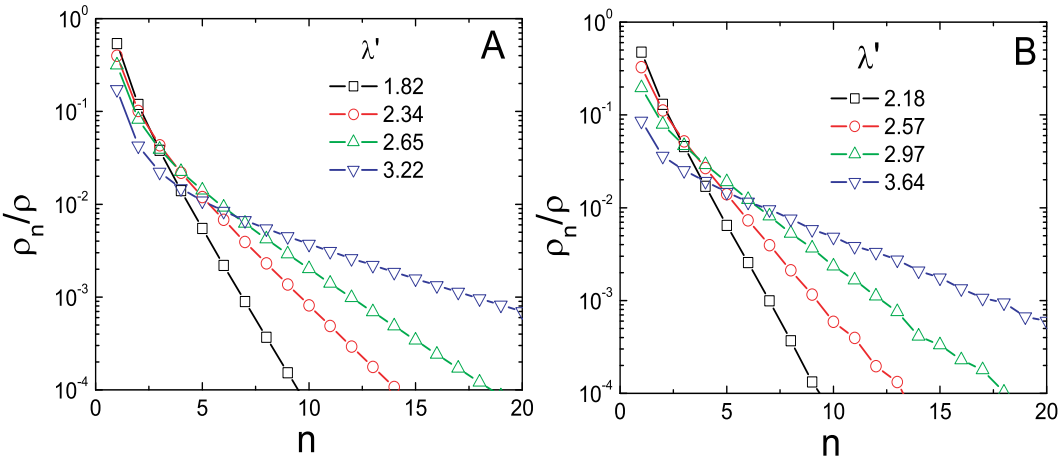


Figure 5.12: The chain length distribution at different electric field strengths, $\lambda'$, predicted by (A)Jordan/Gast theory and (B)MD simulation. The volume fractions are all 4.0%.

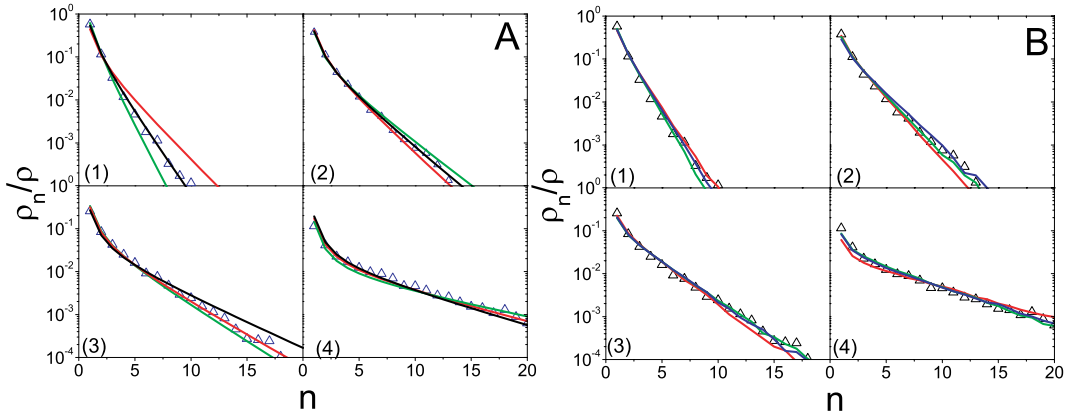


Figure 5.13: A detailed comparison of the chain length distributions between (A)the theory and experiment (B)the simulation and experiment at $E_0$ = (1)14V/mm (2)19V/mm (3)21V/mm (4)24V/mm.

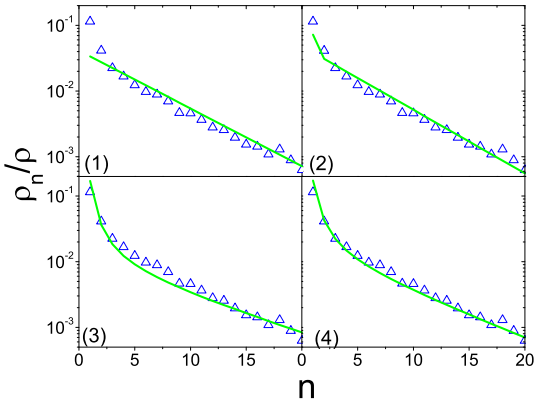


Figure 5.14: (△) the experimentally measured chain length distribution at $E_0$ =24V/mm. The solid lines are best fits from (1)linear aggregation model with binding energy from the nearest neighbors, $\lambda' = 3.2$ (2)linear aggregation model with binding energy from both the nearest and next nearest neighbors, $\lambda' = 2.5$ (3)Jordan model, $\lambda' = 3.6$ (4)Jordan/Gast model, $\lambda' = 3.2$

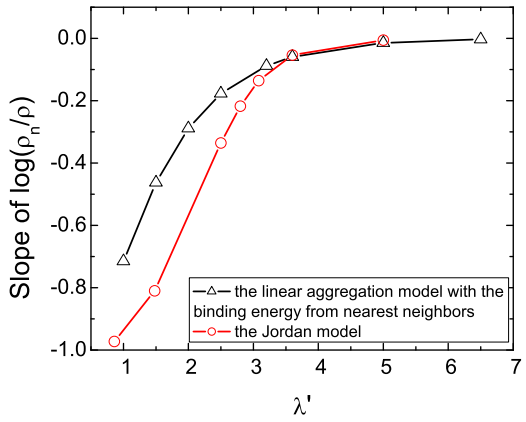


Figure 5.15: The slope of $\log(\rho_n/\rho)$ vs $\lambda'$

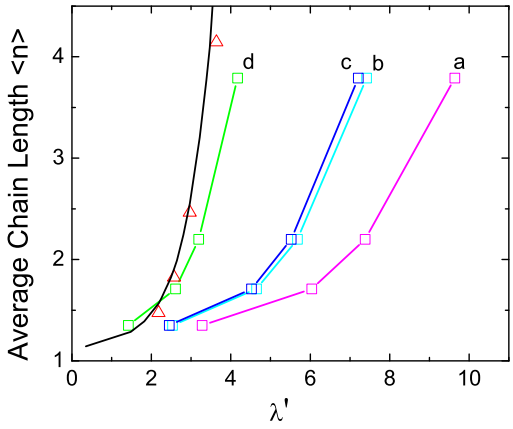


Figure 5.16: (-□-) the experimentally measured average chain length $\langle n \rangle$ vs $\lambda'$, where $\lambda'$ is (a)calculated from the definition $\lambda = \mu^2/\epsilon_w d^3 k_B T$ where $\boldsymbol{\mu} = \epsilon_w^{'} a^3 \left[\frac{\epsilon_p - \epsilon_w}{\epsilon_p + 2\epsilon_w}\right] \mathbf{E}$ , (b)corrected for the mutual polarization, (c)corrected for the frequency dependence of E-field strength, (d)corrected for the effective diameter of sphere (△) $\langle n \rangle$ vs $\lambda'$ obtained from the simulation. The solid line is the relation between $\langle n \rangle$ and $\lambda'$ predicted by the Jordan/Gast theory.

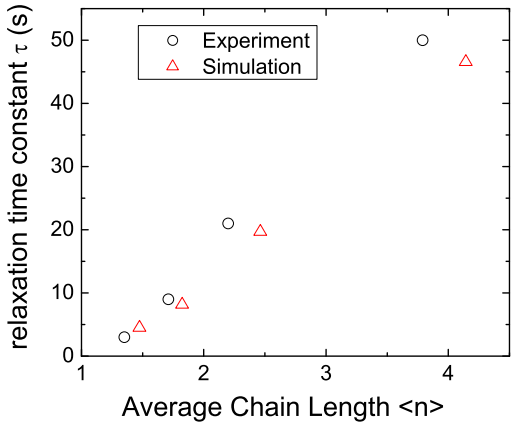


Figure 5.17: The relation between relaxation time constant $\tau$ and average chain length $\langle n \rangle$.

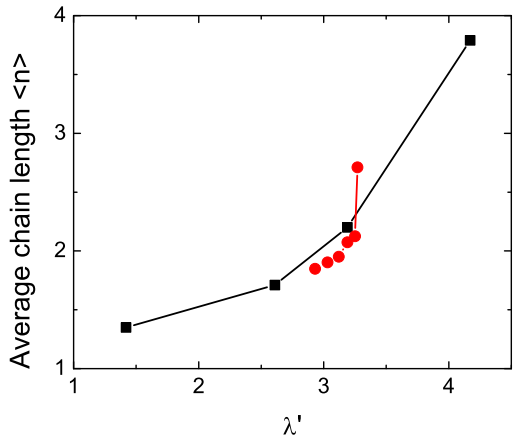


Figure 5.18: (●) the average chain length measured at $E_0 = 2.1 \times 10^4$(V/m) with varying frequencies (a)50kHz (b)140kHz (c)230kHz (d)320kHz (e)410kHz (f)500kHz. (■) the average chain length measured at $f = 230$kHz and different electric field strengths.

due to mutual polarization. However, as Jones and Miller pointed out [37], the higher order moments can be ignored in our case, because here $K = (\epsilon_p - \epsilon_w)/(\epsilon_p + 2\epsilon_w) \approx -0.5$, with $\epsilon_p$, $\epsilon_w$ the complex dielectric constants of the particle and water, where $\epsilon = \epsilon' + i\epsilon''$. Therefore, the interactions between the spheres are essentially dipole-dipole interactions.

At low frequency ($f < 50$kHz in our case), the interactions are more complicated because the double layer polarization cannot be ignored under this condition. The polystyrene spheres are negatively charged in water. The negative surface charge attracts positive ions and forms a double layer near the particle surface. The positive ions in the double layer undergo a random walk biased by the applied electric field. At low frequencies, the biased random walk induces a dipole moment of the double layer in the same direction of the applied electric field. Neighboring particles exert torques upon one another because the induced dipole moment of the double layer has

a phase lag behind the applied electric field. The torques make the spheres spin, and cause a hydrodynamic instability, with spheres associating into rotating bands [35].

At higher frequencies, the biased random walk cannot build up enough magnitude before changing direction. The polarization due to dielectric constants mismatch takes over. The hydrodynamic instability ceases, and spheres bind into chains along the direction of the electric field. The motion of the chains does not have long range correlation, as in low frequencies. The spheres wiggle within each chain, due to the Brownian motion of each individual sphere. At strong field strengths (the rms of field strength $E_0 > 30\,\mathrm{V/mm}$ in our case), spheres irreversibly associate into chains and the chains are never seen to break, as long as the field is on. The average chain length continues growing [26].

At high frequency and weak field strength, the association and dissociation of chains reach equilibrium at a field-dependent time after turning on the field, and the average chain length becomes time-independent. After the electric field is turned off, all the chains dissociate into monomers.

We used weak AC electric field at high frequency in the experiment. The field strengths, $E_0$, were lower than 25V/mm. The frequencies, $f$, were in the range $50\,\mathrm{kHz} \leq f \leq 500\,\mathrm{kHz}$. Under these conditions the spheres associate into chains along the direction of the electric field and the chains appear as dark clusters on a bright background in digitized video images as shown in Fig. 5.7. By choosing a suitable threshold and searching for the contiguous pixels below the threshold, one can find the dark clusters corresponding to the chains. The sizes of the clusters can be accurately measured by counting the number of pixels in them.

The histogram of cluster sizes in Fig. 5.8 shows well defined peaks, which indicate that the clusters are images of chains composed of monodisperse spheres. The area under the $n$-th peak corresponds to the counts of chains comprising $n$ spheres, *i.e.*,

$n$-mers. For longer chains, the peaks are broadened and the statistics are poor. We take the bins obtained from the well defined peaks of shorter chains and fit linearly to get the bins for longer chains. These bins allow us to find out how many spheres there are in a given cluster.

The volume fractions, $\phi$, of spheres in the sample are in the range $0.4\% < \phi < 10\%$. The upper limit is set to ensure the distance between neighboring chains is large enough for them to be resolved. The lower limit of $\phi$ is set to enable us to get enough statistics within a reasonable amount of time.

We use an inverted Nikon DIAPHOT 200 with 20× objective lens and 2.5× projection lens. The microscopic image is converted into video signal with a Hamamatsu XC-77 CCD video camera. A Rev 4 NuBus image board from NeoTech Ltd. was used to digitize the video signal and produce 480 pixel(h) × 640 pixel(v), 256 grey level digitized image. The image board was installed in a 50 MHz Macintosh II $fx$ computer with 8 MB RAM, on which the digital image analysis was done. The calibration shows that $1\mu$m is 3.977 pixels in the horizontal direction, and $1\mu$m is 3.851 pixels in the vertical direction. The image board does not have uniform gain across the whole image. For a uniform background, the top portion of the digitized image appeared about 10% brighter than the rest of the image. We correct this by saving a defocused image and dividing every image by it.

When the electric field is just turned on, the average chain length grows rapidly. After a while, the system reaches equilibrium, and the average chain length stops growing and starts to fluctuate around some fixed value (Fig. 5.10). The relaxation time constant of this process depends on the volume fraction and the applied field strength [1]. We store as many images as possible directly in the RAM when the electric field was just turned on without analyzing them. Then, as the system reaches equilibrium, we analyze each image grabbed and dispose it as soon as the analysis is

done. The number of images needed to be analyzed to get enough statistics depends on the volume fraction of spheres in the sample. For $\phi = 0.4\%$ 100 images are needed, and for $\phi = 10\%$, 50 images suffice. After the required number of images are analyzed, the images stored in the RAM at the beginning are analyzed. It takes $15 \sim 20$ minutes to complete one run.

In Fig. 5.10, we see that the average chain length, $\langle n \rangle$, with an initial value $\langle n(0) \rangle$ when the field was just turned on, approaches a field dependent final value $\langle n(\infty) \rangle$. The relaxation time constant $\tau$, which is also dependent on the field strength, was found by fitting the curve with

$$\langle n(t) \rangle = \langle n(\infty) \rangle + (\langle n(0) \rangle - \langle n(\infty) \rangle) \exp(-t/\tau). \tag{5.13}$$

The ions leaking out from the glass and the electrodes can strongly affect the outcome of the experiment. To offset the ion leakage and thus make the experimental results reproduceable, we added 1 mM NaCl to the suspension. The other benefit of adding electrolytes is to make the electric field uniform in large portions of our cell and enable dynamic equilibrium to be achieved in the system. In a non-uniform electric field, the spheres, which in the aqueous suspension are dielectric holes, drift toward where the field is weaker. The system cannot reach equilibrium if the electric field has a big gradient and drifting is not eliminated. For the field to be uniform it is necessary for the field to be confined to the thin aqueous layer. Confinement is enhanced by making the sample partially conducting since a totally conducting material completely confines an electric field.

Other than the electric field gradient under the post where the data was taken, the field gradient outside the post can also cause spheres to drift. The sample outside the post is thick (see Fig. 5.6), and therefore the field is not as well confined as that under

the post. Big field gradient exists outside the post and strong circulative movement of spheres can happen, so that the spheres under the post will be affected. We carefully design the pattern of the electrodes to minimize the exposure of the electrodes to the sample outside the post and use an o-ring that snugly fit the post to limit the volume outside the post where the strong circulative movement can happen. To ensure that there is no drifting in the system, we constantly check on the total number of spheres in the images as shown in Fig. 5.9.

If some part of a chain is outside an image, the total length of the chain cannot be determined. Excluding those chains that touch boundaries, however, is biased against longer chains, because the probability of touching boundaries is proportional to the chain length. To minimize bias, we maintain that no more than 10% of the spheres in a image would be rejected and make corrections to the chain length distribution accordingly. We see that the number of the spheres that have to be thrown away increases when the electric field is just turned on. After the system reaches equilibrium, that number stops increasing and becomes time independent as shown in Fig. 5.9.

## 5.5 Langevin Simulation Model

An ER fluid is modelled as a neutrally buoyant suspension of spherical particles with diameter $\sigma$ and dielectric constant $\epsilon_p$ in a solvent of dielectric constant $\epsilon_f$ and viscosity $\eta$. The computational geometry is summarized in Fig. 5.1, where $y$ is chosen as the direction of an applied electric field $E\mathbf{e}_y$, and $\theta_{ij}$ the angle between the line joining the two particles and the external field. The dynamic equation for the $i$th particle can be written as

$$md^2\mathbf{r}_i/dt^2 = \mathbf{F}_i^{\text{dip}} + \mathbf{F}_i^{\text{rep}} - 3\pi\sigma\eta d\mathbf{r}_i/dt + \mathbf{R}_i \tag{5.14}$$

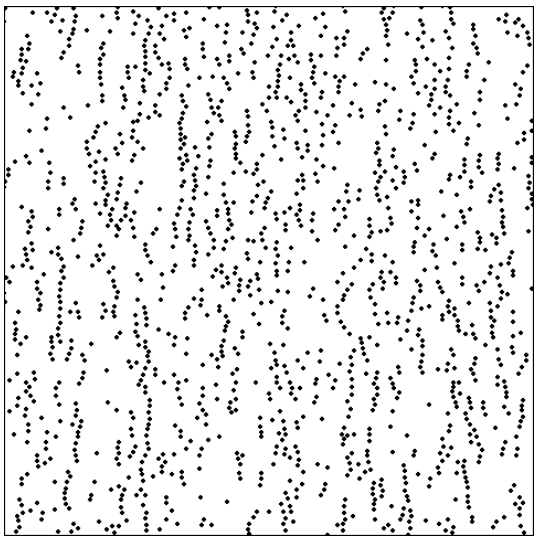

Figure 5.19: Simulation snapshot of equilibrium configuration at $\lambda = 3.85$. The particle volume fraction is 4.0%.

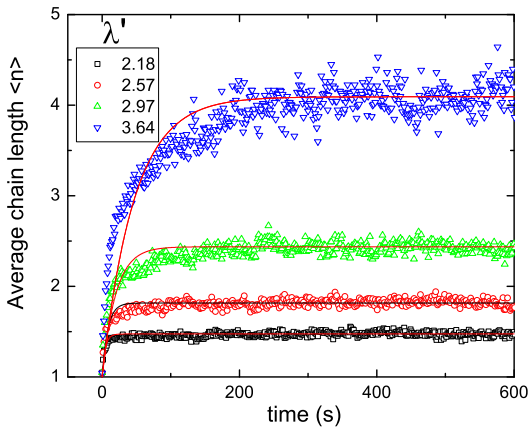


Figure 5.20: The time evolutions of the average chain length at different field strengths from MD simulation.

where $m$ is the mass of the $i$th particle and $\mathbf{r}_i$ its position at time $t$. $F_i^{\text{dip}}$ is the long-range dipolar force and $F_i^{\text{rep}}$ is the short-range repulsive force on the $i$th particle; $-3\pi\sigma\eta d\mathbf{r}_i/dt$ is the hydrodynamic drag force and $R_i$ is the Brownian force, both acting on it through the solvent. The dipolar force on the $i$th particle due to a particle at $\mathbf{r}_j$ is

$$\mathbf{F}_{ij}^{\text{dip}} = \mu^2/(\epsilon_f r_{ij}^4)[(3x/r_{ij} - 15xy^2/r_{ij}^3)\mathbf{e}_x + (9y/r_{ij} - 15y^3/r_{ij}^3)\mathbf{e}_y] \tag{5.15}$$

where $r_{ij} = [(x_i - x_j)^2 + (y_i - y_j)^2]^{1/2}$. We introduce an exponential short-range repulsive force between particles $i$ and $j$ due to the counterions.

$$\mathbf{F}_{ij}^{\text{rep}} = 100k_BT/\sigma \exp[-10(r/\sigma - 1)]\mathbf{e}_r \tag{5.16}$$

We scale Eq. (5.14) by defining dimensionless quantities: $\mathbf{r}_i^* = \frac{\mathbf{r}_i}{\sigma}$, $t^* = \frac{tk_BT}{3\pi\eta\sigma^3} = \frac{Dt}{\sigma^2}$, $\mathbf{R}_i^* = \frac{\sigma}{k_BT}\mathbf{R}_i$, $F_i^{\text{dip}*} = \frac{F_i^{\text{dip}}}{\mu^2/\epsilon_f\sigma^4}$, and $F_i^{\text{rep}*} = \frac{\sigma}{k_BT}F_i^{\text{rep}}$, so Eq. (5.14) becomes

$$\frac{mk_BT}{(3\pi\eta\sigma^2)^2}d^2\mathbf{r}_i^*/dt^{*2} = \lambda\mathbf{F}_i^{\text{dip}*} + \mathbf{F}_i^{\text{rep}*} - d\mathbf{r}_i^*/dt^* + \mathbf{R}_i^* \tag{5.17}$$

with dimensionless parameter $\lambda = \frac{\mu^2}{\epsilon_f\sigma^3k_BT}$. The $\lambda$ characterizes the ratio of the dipolar force to the Brownian force. For most real parameters, the coefficient of the inertia term in the square bracket of the above equation is on the order of $10^{-10}$. This is sufficiently small compared to the coefficients of other terms that the inertia term can be safely neglected.Then Eq. (5.17) is simplified as

$$\mathbf{r}_i^*(t^* + \Delta t^*) = \mathbf{r}_i^*(t^*) + \lambda\mathbf{F}_i^{\text{dip}*} \cdot \Delta t^* + \mathbf{F}_i^{\text{rep}*} \cdot \Delta t^* + \mathbf{R}_i^*(\Delta t^*) \tag{5.18}$$

where $\mathbf{R}_i^*(\Delta t^*)$ is a random displacement which is governed by a Gaussian probability distribution function with an average value of zero and a mean square value of $4D_0\Delta t$.

$D_0$ is the diffusion coefficient of the particle.

The boundary condition is made periodic. That is, the system consists of 1500 particles within a plane of side length $L^* = 120$ which is then periodically repeated throughout two-dimensional position space. If a particle travels out one side of the plane, an image enters the plane through the opposite side so that the number of particles in the plane remains constant. The particle volume fraction is 0.04. Because the dipole-dipole attraction is not long-ranged, the force on a particle can be summed over contributions from particles within $5d$, $d$ the particle diameter, of the particle center.

The computer experiment is conducted as following. The particles are all given an initial random position in the plane. During each time step, each particle undergoes a displacement according to Eq. (5.18), where the random displacement $\mathbf{R}^*$ is randomly chosen from 1000 equally probable values taken from a histogram approximation to the continuous Gaussian distribution. At the beginning, the system is given some time to equilibrate with no field applied. After turning on the electric field, we monitor the chain length distribution (Fig. 5.12). Fig. 5.19 is a snapshot of the simulation at equilibrium.

## 5.6 Results

The experimental chain length distributions, $\rho_n/\rho$, at different field strengths are plotted in Fig. 5.11, while those predicted by the Jordan/Gast theory and the MD simulation are shown in Fig. 5.12. The frequencies of the applied electric fields are all 230kHz and the field strengths are $2.4 \times 10^4$, $2.1 \times 10^4$, $1.9 \times 10^4$, and $1.4 \times 10^4$V/m, respectively. The average number of spheres in the images are 1483, 1453, 1542, and 1540, respectively. The height of the sample cell is measured to be 1.9$\mu$m, 1.5 times

the sphere diameter. Therefore, the volume fractions, $\phi$, of the spheres are calculated to be 4.2%, 4.1%, 4.3%, and 4.3%, respectively.

A more detailed comparison is shown in Fig. 5.13. At lower field strengths, the curves of experiment and Jordan/Gast theory fit very well. At higher field strengths, the experimental curves show less curvature than those of the Jordan/Gast theory. On the other hand, we found good agreements between the experiment and simulation at all field strengths.

Fig. 5.16 is a comparison of the average chain length $\langle n \rangle$ as a function of $\lambda'$ between experiment, theory and simulation. $\lambda'$ in the experimental measurement is reduced by 0.77 to correct for mutual polarization, by $0.985^2 \approx 0.97$ to correct for the frequency dependence of field strength, and further by $1/1.2^3 \approx 0.58$ to correct for the effective diameter of sphere.

We measured the frequency dependence of average chain length at a fixed E-field strength and plot it against $\lambda'$ modified to account for the frequency variation. (Fig. 5.18). There's a good agreement with the measured average chain length as a function of E-field strength at a fixed frequency.

Another aspect of this experiment is the measurement of the relaxation time constant $\tau$ for the system to approach equilibrium after the field is turned on. The relaxation time constant $\tau$ as a function of average chain length compares well to simulation results based on the measured particle diffusion coefficient, which is $D_{\text{exp}} = 0.308 \mu m^2/s$ (Fig. 5.17).

## 5.7 Conclusions

We have presented an experimental study of the electric field induced aggregation of colloidal particles using digitized video microscopy. The kinetics of reversible associ-

ation of colloids, measured by monitoring the cluster size distribution as a function of time after an alternating field was applied, agrees very well with a Langevin molecular dynamic simulation. The equilibrium distributions are qualitatively similar to what is predicted by Jordan/Gast and the MD simulation. The reduction of field strength due to frequency variation and mutual polarization of spheres has been taken into account. We also measured the relaxation time constant of the system approaching dynamic equilibrium, which compares favorably to the simulation.

## 5.8 Appendix: Theory

Defining a coordinate system oriented relative to the electric field, the vector separation between neighboring grains in a $n$-mer is

$$\mathbf{r}_{i,i+1} = d'(1+\xi_i)\left(\sin\theta_i\cos\phi_i, \sin\theta_i\sin\phi_i, \cos\theta_i\right) \tag{5.19}$$

in which $0 < \psi_i < \infty$, $0 < \theta_i < \pi$, and $0 < \phi_i < 2\pi$. The potential between nearest neighbors is

$$\frac{U_{i,i+1}}{k_B T} = \lambda\frac{(1-3\cos^2\theta_i)}{(1+\xi_i)^3} + \eta e^{-\kappa d\xi_i} \tag{5.20}$$

with $\lambda = \mu^2/\epsilon'_w d^3 k_{\mathrm{B}} T$, where $\mu$ is defined in Eq. (5.1) and $\eta = \epsilon_w d\psi_0^2/4$.

Before we calculate the energy of a chain of particles, we first have to define more precisely how we assign a particular set of particles to a particular chain. The concept that each $n$-mer is a chemically distinct species is only valid when each chain is composed of particles very close to each other and far away from any particles in another chain. Since we are also calculating an equilibrium distribution, we necessarily must allow the chains to break and reform which means that at these times the chains are not well defined. However as long as the lifetime of the chains is long

with respect to the time to recognize and as long as the chains are separated from each other, the chains will be well defined most of the time and thus experimentally (and theoretically) identifiable. We consider a particle to be part of a chain if its center is within a distance, small with respect to the particle diameter, of the center of another particle. When spheres are close to each other, the total energy of a chain is approximately given by assuming all the spheres are in end-to-end contact and summing the interaction energy of each particle with the rest particles in a chain. The partition function calculated from this total energy would describe fairly well the distribution of chain lengths among the particles, but could not say anything about the fluctuations within a chain.

Since the screened Coulombic repulsion decays exponentially making the electrostatic interactions negligible beyond nearest neighbors, we keep only first order terms in $\xi$ and $\theta^2$ to describe the fluctuations within a chain and we consider contributions to the interaction energy different from the lowest energy only from next nearest neighbors. For particles in a chain separated by more than next nearest neighbors distance, we keep only the zero order terms in $\xi$ and $\theta^2$. The vector separation between next nearest neighbors is $\mathbf{r}_{i,i+2} = \mathbf{r}_{i,i+1} + \mathbf{r}_{i+1,i+2}$. The magnitude of the separation $\mid \mathbf{r}_{i,i+2} \mid$ and $\cos^2\theta_{i,i+2}$ to lowest order in $\xi$ and $\theta^2$ is

$$r_{i,i+2} = 2d_{\min}\left[1 + \frac{\xi_i + \xi_{i+1}}{2} + \frac{\theta_i\theta_{i+1}\cos(\phi_i - \phi_{i+1})}{4} - \frac{\theta_i^2 + \theta_{i+1}^2}{8}\right] \quad (5.21)$$

$$\cos^2\theta_{i,i+2} = 1 - \frac{\theta_i\theta_{i+1}\cos(\phi_i - \phi_{i+1})}{2} - \frac{\theta_i^2 + \theta_{i+1}^2}{4} \quad (5.22)$$

With these results one obtains

$$\frac{U_{i,i+2}}{k_BT} = \frac{\lambda'}{8}\left[2 - 3(\xi_i + \xi_{i+1}) - 3\theta_i\theta_{i+1}\cos(\phi_i - \phi_{i+1})\right] \quad (5.23)$$

Here $\lambda' = \lambda/d_{\min}^3$, and $d_{\min}$ is determined from Eq. (5.8). In summary, the energies of interaction in our model are

$$\frac{U_{i,i+1}}{k_B T} = \lambda \frac{(1-3\cos^2\theta_i)}{(1+\xi_i)^3} + \eta e^{-\kappa d \xi_i} \tag{5.24}$$

$$\frac{U_{i,i+2}}{k_B T} = \frac{\lambda'}{8}\left[2 - 3(\xi_i + \xi_{i+1}) - 3\theta_i\theta_{i+1}\cos(\phi_i - \phi_{i+1})\right] \tag{5.25}$$

$$\frac{U_{i,i+n}}{k_B T} = \frac{2\lambda'}{n^3} \qquad \text{for} \quad n > 2 \tag{5.26}$$

The total potential energy for a chain of $n$ particles are

$$-\frac{U_n}{k_B T} = \lambda' \left\{ \sum_{j=1}^{n-1} \frac{2(n-j)}{j^3} - \sum_{j=1}^{n-2} \frac{3}{8}\left[\xi_j + \xi_{j+1} + \theta_j\theta_{j+1}\cos(\phi_j - \phi_{j+1})\right] \right\} \tag{5.27}$$

$$- \sum_{j=1}^{n-1} \left[ \lambda \frac{(1-3\cos^2\theta_j)}{(1+\xi_j)^3} + \eta e^{-\kappa d \xi_j} \right] \tag{5.28}$$

In the substitution $\lambda \to \lambda' = \lambda/d_{\min}^3$, where $d_{min}$ is determined from Eq. (5.8).

### 5.8.1 Partition Function

The classical partition function for a chain of $n$ particles is

$$q_n = \frac{1}{h^{3n}} \int e^{\frac{-\beta p_1^2}{2m}} d^3p_1 \cdots \int e^{\frac{-\beta p_1^2}{2m}} d^3p_n \int e^{-\beta U_n(r_1,\cdots,r_n)} d^3r_1 \cdots d^3r_n \tag{5.29}$$

We treat the particles as distinguishable, because we know precisely where each particle is located in a chain and can track the center of each particle at all times using digital video microscopy.

The dimer partition function is proportional to the configuration integral over all bonded states of a particular pair. Because of symmetry, we only need to integrate

over a hemisphere to give

$$q_2 = \frac{V}{\Lambda^6}\int_{r_1}^{r_2}\int_0^{\pi/2}\int_0^{2\pi}\exp[-u(\mathbf{r})/k_{\mathrm{B}}T]\mathrm{d}\phi\sin\theta\mathrm{d}\theta r^2\mathrm{d}r \tag{5.30}$$

Here $\sin\theta \approx \theta$ when $\theta$ is small. Like Gast [1], the upper limit on $\theta$ is chosen to be $\sqrt{2}$ to preserve the correct form in the absence of a dipole. With the substitution of the pair potential Eq. (5.4), we thus obtain

$$\begin{aligned} q_2 &= \frac{VB_\infty}{\Lambda^6} \\ B_\infty &= 2\pi d^3\int_{r_1}^{r_2}\exp[-u_{\mathrm{rep}}(r)/k_{\mathrm{B}}T]\exp(2\lambda/r^3)\frac{r^3}{6\lambda}[1-\exp(-6\lambda/r^3)]r^2\mathrm{d}r \end{aligned} \tag{5.31}$$

where $u_{\mathrm{rep}}(r)$ is the electrostatic repulsion energy, and $r$ is dimensionless on $d$. In the limit of large $\lambda$ and a hard-sphere repulsion, the form of Eq. (5.31) reduces to previous results for $B_\infty$ [38]. The limits of integration, $r_1$ and $r_2$, correspond to the definition of a dimer. The dimer partition function is not sensitive to these limits unless the attractions become very weak. Our definition of a dimer includes those particles falling within the nearest neighbor shell $1 < r < 2$, which also corresponds to our criterion for counting chains in the molecular dynamics simulation described above.

Next we find the partition function for a $n$-mer where $n \geq 3$

$$q_n = \frac{V}{\Lambda^{3n}}\left(\frac{8}{9}\right)^{n-2}(B_\infty)^{n-1}\prod_{j=1}^{n-2}\frac{1}{a_j}\left(\frac{8}{9}\right)\left(\frac{54}{51}\right)^2\cdot \exp\left[\lambda'\sum_{j=1}^{n-2}\frac{2(n-j-1)}{(j+1)^3}\right] \tag{5.32}$$

where

$$a_j = 1 - \frac{1}{256a_{j-1}}, a_0 \equiv 1 \tag{5.33}$$

In view of the approximations made up to this point a small error is introduced by the following simplifications of $q_n$ which will hold for $n \geq 2$:

$$q_n = \frac{V}{\Lambda^{3n}} \left(\frac{8}{9a_1}\right)^{n-2} (B_\infty)^{n-1} \exp[-2\lambda'(n-1)] \cdot \tag{5.34}$$

$$\exp\left[\lambda' \sum_{j=0}^{n-2} \frac{2(n-j-1)}{(j+1)^3}\right] \tag{5.35}$$

The sums over $j$ in the equation above can be rewritten as

$$\sum_{j=0}^{n-2} \frac{(n-j-1)}{(j+1)^3} = n\zeta(3) - \zeta(2) - \sum_{j=n+1}^{\infty} \left(\frac{n}{j^3} - \frac{1}{j^2}\right) \tag{5.36}$$

$$\tag{5.37}$$

Eq. (5.34) can also be rewritten as

$$q_n = \frac{V}{\Lambda^{3n}} \frac{9a_1}{8} C^{n-1} \exp(-2\lambda' \mu_n) \tag{5.38}$$

with

$$\mu_n = \zeta(2) - \zeta(3) + \sum_{j=n+1}^{\infty} \left(\frac{n}{j^3} - \frac{1}{j^2}\right) \tag{5.39}$$

$$\tag{5.40}$$

and where

$$C = \frac{8}{9a_1} B_\infty \exp[2\lambda'(\zeta(3) - 1)] \tag{5.41}$$

The coefficients $\mu_n$ varies monotonically from $\mu_2 = \zeta(3) - 1 = 0.2020$ to $\mu_\infty = \zeta(2) - \zeta(3) = 0.4428$ and Using Eqs. (5.5) and (5.6) we can relate the number density of a $n$-mer to the monomer concentration:

$$\rho_n = \frac{9a_1}{8} \frac{x^n}{C} e^{-2\lambda' \mu_n}, \quad \rho_1 = \frac{x}{C} \tag{5.42}$$

Conservation of mass, expressed in Eq. (5.7), provides an equation for $x$:

$$\rho = \frac{x}{C} + \frac{9a_1}{8C} \sum_{n=2} n x^n e^{-2\lambda' \mu_n} \tag{5.43}$$

The same observations that Jordan made concerning the equivalent equation in his paper hold true here. The upper bound to $x$ is one, and as $x \to 1$ long chains are favored. The condition for chain formation is given by $\rho C \sim 1$.

# Appendix A

# Production of fd, M13 and Mutant M13-C7C Viruses

In this appendix we present protocols used to produce fd, M13, and M13-C7C virus discussed in this thesis. This condensed protocol was developed by Dr. Kirstin Purdy [64] and other members of the Fraden lab. Extensive descriptions of these protocols can be found in Ref. [52, 59]. The protocols also include the procedures for dialysis, DNA manipulation, modification of viral coat proteins, and sample preparation for transmission electron microscopy.

## A.1 Preparation of Wild-Type Bacteriophage fd and M13

### A.1.1 Recipes for LB Media and Agar Plates

**LB Media (from Maniatis p. A1)**

1. Add to 950ml filtered $H_2O$:

10 g bacto-tryptone

5 g bacto-yeast

7.5 g NaCl

2. Dissolve solutes by stirring. After dissolved, adjust volume to 1 L with more filtered water.

3. Sterilize by autoclaving for 20 minutes.

**Preparation of Agar Plates(from Maniatis p. A4)**

1. Prepare LB media and add the following agar before autoclaving:

    15 g/L bacto-agar (for plates)

2. Sterilize by autoclaving for 20 minutes.

3. Let solution cool after autoclaving, and then pour media solution into ∼20 sterile plates/L. After plates have cooled, invert them to prevent condensation from dripping on hardened agar.

4. Let plates sit out overnight. This will allow time for any plates that have been accidentally contaminated to begin to grow impurities. Discard any impure plates, and store the remaining plates inverted at 4°C. Plates are good for 1-2 months.

**Preparation of Stock Supply of Top Agar**

1. Prepare LB media and add the following agar:

   7 g/L bacto-agar (for top-agar)

2. Heat the solution until Agar is completely dissolved, then place 3 ml of the solution in a series of test-tubes.(For an easy way to heat and dissolve agar autoclave the solution for 20 min. Note, that you will still need to autoclave the solution again after placing solution into test tubes)

3. Sterilize by autoclaving test-tubes for 20 minutes.

4. After the agar solution has cooled, the test tubes can be stored indefinitely in the refrigerator.

### A.1.2 Step 1: Plating Bacteria: JM101 or XL1-Blue

Bulk bacteria JM101 and XL1-Blue are located in the deep freezer of Prof. Azadeh Samadani's lab. JM101 grows quickly, but could lead to a high level of polydispersity in the virus population. fd and M13 produced by XL1-Blue are more monodisperse. However, since the growth of XL1-Blue is much slower, the viral yield is only one third to one half of that from JM101 strain. If all of the plates of bacteria within the lab are old (ie. single colony does not grow in 3mL sterile LB media when incubated overnight at 37$^o$C) or infected, new plates of bacteria must be streaked.

1 Prepare Plates of LB media A.1.1.

2. Using sterile wooden sticks, touch bulk frozen bacteria. Gently streak this bacteria onto sterile plate in a zig-zag motion, filling $\sim$1/3 of the plate. Using a different sterile stick, zig-zag through the first set of streaks into the second 1/3 of the plate. Zig-zag through the second set of streaks with a new sterile stick to fill the third 1/3 of the plate. Make 2 or 3 new plates.

3. Incubate overnight at 37$^o$C. These plates are good for about a month, after which the percent of living cells decreases rapidly. Be sure to label plates with date and type of bacteria. To prevent evaporation seal the edges of the plates with parafilm.

### A.1.3 Step 2: Plating Virus-Infected Bacteria (JM101 or XL1-Blue infected with fd/M13)

If there is no fresh stock solution of virus (M13, fd) (Preparation of this stock solution is described in A.1.4). The technique described in this section will provide you with plaques of bacteria which have been infected with the virus you added. These plaques can then be used for amplification (ie. in creation of the stock solution described in (A.1.4)). If a fresh stock solution exists it can be used for large scale virus growth or new plates and new infecting batches of virus can be made using this technique. If there is no stock solution at all it must be obtained from an outside source.

**1.(AM) Grow a Small Quantity of Bacteria in Solution**

1. Prepare 1-2 test tubes of 3 mL of sterile LB media.(Flame mouth of LB container before pipetting liquid from bulk. Flame vial mouth before and after LB is added, to ensure sterility.)

2. Inoculate each test tube with a colony of bacteria from previously prepared plates (section A.1.2) by touching the colony with a sterile wooden stick. Swirl tip of infected stick in the test tube briefly, then flame mouth of the test tube and recap.

3. Incubate in an agitator at 37$^o$C for 6-10 hours until turbid.

**2. Titrate Existing Virus Solution**

If bulk solution of wild-type virus as described in A.1.4 exists, prepare a series of tenfold dilutions of the bacteriophage to $10^{-11}$ of the original concentration. Dilute 100$\mu$l of the stock solution with 900 $\mu$l $H_2O$, mix and repeat dilution. You should

end up with a series of solutions of concentrations $10^{-1}, 10^{-2}...10^{-11}$. Use one of these for each plate. If this bulk solution does not exist or is too old to trust, titrate from stock located in freezer (stock labeled in pfu's, titrate down to $\sim$1 pfu). *pfu=Plaque forming unit.

**3. (PM) Mix Bacteria and Virus in Top Agar and Plate**

1. Prepare top agar fresh in test-tubes(A.1.1), or thaw pre-made test tubes of agar in beaker of water which is brought to boil. Keep agar warm (45-50$^o$ C) in temperature controlled environment (typically a heating block with a test-tube holding rack installed).

2. Into one test-tube of melted top agar add 100 $\mu$l of a virus solution and 300 $\mu$l of the bacteria solution. Gently swirl mixture, and then quickly pour mixture onto media plates which have been brought to room temperature. Repeat this for each of the different concentrations of titrated virus. Be sure to flame all test tubes every time they are opened and closed. The only exception being after you add the last component to the top agar do not flame the test tube. Occasionally flaming immediately before you pour the top agar onto the plates will kill the bacteria as you pour out the agar because the glass is still too hot.

3. Incubate plates overnight. Keep plates containing small single plaques. These plates should contain $\sim$1 pfu. The plaques of virus infected bacteria are used when making large quantities of virus.

### A.1.4 Step 3: Small Scale Amplification, Making the "Infecting Batch" of Virus from a Plaque

1. Take 50 ml of sterile LB and inoculate it with 1 or 2 plaques of bacteria infected with the virus from plates made in section A.1.3. This is usually done by stabbing

plaque with a glass pipette tip which has been sterilized by dipping in alcohol and flaming and then releasing the clump of infected media into the LB.

2.Agitate in an incubator at $37^o$c overnight.

3.Remove turbid solution of infected bacteria from incubator and pour into sterile centrifuging vial. Spin at 3300 g (4000 rpm in Sorvall RT-7 with RT-750 rotor) for $>$ 30 minutes.

4. Pour supernate of virus solution into sterile vial with purple lid. Refrigerate at $4^o$C until needed for use.

### A.1.5 Step 4, Day 1: Large Scale Wild-type Virus (fd and M13) Amplification

**Day 1 AM: Prepare a Small Quantity of Bacteria in Solution**

1. Prepare 1 test tube of 3 mL of sterile LB media for each of the 3 L of LB media you plan to infect.(Flame mouth of LB container before pipetting liquid from bulk. Flame vial mouth before and after LB is added, to ensure sterility.)

2. Inoculate each test tube with a colony of bacteria from previously prepared plates (section A.1.2) by touching the colony with a sterile wooden stick. Be careful not to breathe on the open plates. Swirl tip of infected stick in the test tube briefly, then flame mouth of the test tube and recap.

3. Incubate in an agitator at $37^o$C for 6-10 hours until turbid.

4. Prepare 3 liters of sterile LB media(A.1.1) for each test tube of bacteria you are growing. Placing $\sim$700ml in in a 2L flask.

**Day 1 PM: Infect X liters of LB** 1. Infect each 2L flask with $\sim 0.7ml$ of bacteria. Incubate and agitate until slightly turbid,$\sim$3 hours.

2. After 3 hours, add 0.5ml infecting batch virus as prepared in A.1.4 to each 2L flask

and incubate for another 6-10 hours, or overnight.

### A.1.6 Step 5, Day 2: Purification of Virus

1. Pour turbid solution of bacteria and virus into large centrifuge jars. Centrifuge at 3300 g for >30min. Keep supernate.

2. Add 20 g/L PEG 8000 and 20 g/L NaCl to the supernate. The solution should become slightly turbid as it is mixed. This is due to the condensation of the virus particles from the depletion by the PEG. Respin this solution at 4000 rpm (3300 g) for another 30-45 minutes.

3. On the bottom of the centrifuge jars should be thick concentrated virus and polymer mixture. Dissolve it with ∼3 ml of distilled $H_2O$. Pipette off as much virus solution as possible and transfer it to the ∼ 50 ml Sorvall centrifuge containers (round bottom, purple lid).

4. Yield at this stage should be approximately 10-100mg/L depending on the freshness of the bacteria and virus solutions used.

5. To continue purification, spin concentrated virus solution at ∼20000 g (13000 rpm in Sorvall centrifuges on 3rd floor Rosenstiel) for > 45 minutes. Keep supernate, and check for virus in supernate by spectrophotometry. If virus is not present in large quantities sediment should be diluted and spun again. Otherwise the sediment can be discarded.

6. Spin virus solution again at 13000 rpm (20000 g) for > 45 minutes.

7. Spin virus at ∼250000 g for 3 hours (50000 rpm LE 80 or LE 70 Beckmann centrifuge using Ti 70.1 rotor). Carefully discard supernate (which should contain only polymer and other unwanted contaminants). Dilute virus with buffer or water(approximately 500 $\mu$l), and let resuspend overnight (vortex thoroughly to aid in resuspension).

8. At this point in the purification process virus should be dialized against a buffer (see A.4.4) before continuing on to the final step.

9. Spin virus down again at ∼250000 g for >2 hours, and remove the supernate afterwards. Add just enough buffer to resuspend virus to concentration of a smectic ($\sim 200\mu$l).

## A.2 Preparation of P3 Phage-Display M13-C7C Virus

M13-C7C is a M13-structured virus which has been modified to display 9 extra amino acids on the end of the P3 infective protein. It is available from New England Biolabs as the C7C Phage Display Peptide Library. The "7" refers to a random sequence of 7 amino acids. These can be specifically selected for using phage display techniques, however as we are only interested in the Cysteines flanking the random amino acids this protocol is for simple amplification of any phage from the supplied library.

### A.2.1 Solution Recipes

-LB Media: 1L distilled $H_2O$, 10g bacto-tryptone, 5g bacto-yeast, 7.5g NaCl. Autoclave for 20 minutes.

-LB Plates: LB Media, 15g/L Bacto-agar. Autoclave for 20 minutes. After autoclaving, pour warm media solution into ∼20 sterile plates/L. After plates have cooled, invert and let sit out overnight to check for accidental contamination. Discard any impure plates, and store the remaining plates inverted at $4^oC$. Plates are good for 1-2 months.

-LB-TET solution: LB with 1mL/L Tetracycline added after autoclaving.

-LB-TET plates: LB Media, 15g/L Bacto-Agar, Autoclave. When warm, add 1mL/L Tetracycline stock (20mg/mL in ethanol, stored at -20$^o$C). Pour cool solution into $\sim$20 sterile plates/L. After plates have cooled, invert and let sit out overnight to check for accidental contamination. Store inverted at 4$^o$C.

-Top Agar: LB Media, 7g/L bacto-agar. Heat the solution until Agar is completely dissolved, then place 3ml of the solution in a series of test-tubes. Sterilize by autoclaving test-tubes for 20 minutes. Store in the refrigerator.

-Xgal solution: 20mg/mL Xgal in Dimethylformamide (DMF). Store in -20$^o$C freezer. ($^*$ Xgal= 5-bromo-4-chloro-3-indolyl-bD-galactoside)

-IPTG solution: 200mg/mL IPTG in dH2O; sterilize by passing IPTG through 0.22 mm filter. Aliquot to 1 ml, store -20$^o$C freezer. ($^*$ IPTG= Isopropyl-beta-D-thiogalactopyranoside)

-Sodium acetate buffer: 3M, pH 5.2

Glassware should be washed, rinsed, rinsed with ethanol, dried and then autoclaved before use!

### A.2.2 Step 1: Grow ER2738 on LB-TET or LB plates

1. Prepare Plates of LB media.(LB-TET plates are recommended by New England Biolabs but we have found that this produces an abnormally large amount of impure plates and foreign growth. Growth of ER2738 on plain LB plates has shown to drastically reduce foreign grown making the plates much more stable for long periods of time)

2. Using sterile wooden sticks, touch bulk frozen bacteria ER2738. Gently streak this bacteria onto sterile plate in a zig-zag motion, filling $\sim$1/3 of the plate. Using a different sterile stick, zig-zag through the first set of streaks into the second 1/3 of the plate. Zig-zag through 2nd third to fill the third 1/3 of the plate. Make 2 or 3

new plates.

3. Incubate overnight at 37$^o$C. These plates are good for about a month. Be sure to label plates with date and type of bacteria.

### A.2.3 Step 2: Plating M13-C7C-Infected Bacteria

**1.(AM) Grow a Small Quantity of Bacteria in Solution**

1. Prepare 1-2 test tubes of 3mL of sterile LB media.(Flame mouth of LB container before pipetting liquid from bulk. Flame vial mouth before and after LB is added, to ensure sterility.)

2. Inoculate each test tube with a colony of ER2738 from previously prepared plates (section A.2.2) by touching the colony with a sterile wooden stick. Swirl tip of infected stick in the test tube briefly, then flame mouth of the test tube and recap.

3. Incubate in an agitator at 37$^o$C for 6-8 hours until turbid.

**2. Titration of M13-C7C library**

Prepare tenfold dilution series of M13-C7C in LB; Initial library concentration = 1x10$^{13}$. Dilute to 1x10$^3$ and plate as desired, though only concentrations ¡ 1x10$^6$ produce individual plaques suitable for amplification.

**3. (PM) Mix and Plate ER2738 and M13-C7C**

1. Prepare top agar fresh in test-tubes(A.1.1), or thaw pre-made test tubes of agar in beaker of water which is brought to boil. Keep agar warm (45-50$^o$C) in temperature controlled environment.

2. To each top agar, add 100 $\mu$L ER2738 culture (grown for 6 - 8 hrs), 10 $\mu$L virus dilution, 40 $\mu$L Xgal, 4 $\mu$L IPTG. Be certain to pre-warm the plates. Mix by swirling. Pour top agar onto plate. After top agar has solidified incubate overnight (18 hrs **MAXIMUM**), then refrigerate. Useful plates have clearly defined blue plaques that are not in contact with each other.

### A.2.4 Step 2: Small Scale Amplification of M13-C7C Plaque ("Infecting Batch")

**1.(Day 1 PM) Grow a Small Quantity of Bacteria in Solution**

Prepare 1-2 test tubes of 3 mL of sterile LB media. Inoculate each test tube with a colony of ER2738 from previously prepared plates (A.2.2) by touching the colony with a sterile wooden stick. Swirl tip of infected stick in the test tube briefly, then flame mouth of the test tube and recap. Incubate overnight.

**2. (Day 2 AM) Prepare 20 ml Infecting Batch**

Use 20 mL sterile LB media, and add 200 $\mu$L (overnight) ER2738 culture and 1 blue plaque from the plate. Incubate 5 hours on the shaker. Centrifuge at 4000 rpm for 30 min to sediment bacteria. Keep supernate by decanting into a fresh tube.

### A.2.5 Step 3: DNA sequencing

1. Before bulk amplification, the virus solution must be DNA sequenced to ensure that it is C7C. To precipitate the DNA, take 400 $\mu$L of each plaque amplification solution. Add 200 $\mu$L phenol(!), vortex for 1 minute, and centrifuge for 10 min. Pipette the aqueous layer to a fresh microcentrifuge tube. Add 400 $\mu$L chloroform(!) to the aqueous layer, vortex for 1 minute, and centrifuge for 10 min. Pipette aqueous layer to a new centrifuge tube. Add 40 $\mu$L sodium acetate buffer. Add 1200 $\mu$L cold ethanol, vortex 1 minute. Place in freezer 20 min. to precipitate DNA, then centrifuge 20 min. to pellet DNA. Pipette off supernate, and allow to dry overnight in the hood. Resuspend the following day in 20 $\mu$L $dH_2O$.

2. To measure concentration and purity, absorption must be measured. Dilute 3 $\mu$L of DNA with 400 $\mu$L $dH_2O$. Measure absorption at 260 nm and 280 nm; $A^{260}/A^{280}$ must be greater than 1.5 to obtain a useful sequence. If $A^{260} = 1$, then [solution]

= 50 $\mu$g/mL. Determine concentration of stock DNA solution by multiplying [diluted solution] by (400/3). For sequencing we Fed-Ex our DNA samples to Elim Biopharmaceuticals and follow their recommended sample preparation protocol. For sequencing, approximately 1 $\mu$g of DNA is required, along with 8 pmols of primer (from NEB, -96gIIIp), in a final volume of 15 $\mu$L.

3. Upon receiving the sequence, compare it to the NEB C7C kit booklet page 12; the region between restriction sites Eag I and Kpn I must exist for the sequence to be correct. Ensure that the sequence is being read in the proper direction!

**Purity of M13-C7C by Agarose Gel Electrophoresis**

Prepare gel for electrophoresis as in A.3.1. To run the DNA, dilute 2 $\mu$L of DNA solution to 20 $\mu$L, and add 4 $\mu$L of loading buffer for thick lane comb. If using the thin lane comb, dilute the DNA 1:10, and add 2 $\mu$L of loading buffer. Run and stain gel as described in A.3.1.

The band of M13-C7C should be slightly higher than the band for M13, as the size difference is very small, but M13-C7C is longer and should run slower. It is best to run M13, Fd, and a known sample of M13-C7C as standards for comparison.

### A.2.6 Step 4: Large Scale Amplification of M13-C7C to 700mL

**Day 1 PM: Grow a Small Quantity of Bacteria in Solution**

Prepare 1-2 test tubes of 3 mL of sterile LB media. Inoculate each test tube with a colony of ER2738 from previously prepared plates (A.2.2) by touching the colony with a sterile wooden stick. Swirl tip of infected stick in the test tube briefly, then flame mouth of the test tube and recap. Incubate overnight.

**Day 2 AM: Amplification**

Once a stock solution known to contain M13-C7C is obtained, bulk amplification can begin. Prepare 700 mL of sterile LB media and add 10 mL (overnight) ER2738

solution with 500 $\mu$L virus solution. Incubate **5 hours** on the shaker. Do not incubate longer as the probability of wild-type viral growth increases with time.

**Day 2 PM: Purification**

Follow the same purification steps in A.1.6, but be sure to keep all virus samples separate ( from each 700 mL growth), as there is no guarantee that the virus in each growth is the same (wild type or M13-C7C mutant). After virus is centrifuged at $\sim$20000 g (13000 rpm), and the majority of the bacteria has been removed by precipitation, **the viral DNA should be sequenced again (A.2.5)**. Contamination of the M13-C7C solution by miniscule amounts of wild type M13 or fd is quite common and happens 2/3 of the time. The growth of these wild type phages is exponentially faster as the P3 (infecting protein) is not damaged. If the M13-C7C virus has grown the yield will not be very large, perhaps 20 mg/700 mL at best.

## A.3 Techniques for Purification and Analysis of Viral DNA

**Phenol-Choroform Extraction of DNA**

Cautions: Phenol, Chloroform and Ethidium bromide are toxic! Work in the hood, wearing gloves. Dispose of waste in proper bins.

For 100 $\mu$l of fd at 1mg/ml add 50 $\mu$l Phenol (very toxic!), vortex for 1 minute. Centrifuge (max speed on microcentrifuge $\sim$ 14000 g) to separate solution. Transfer top (aqueous part containing DNA) to new microcentrifuge tube. Add 100 $\mu$l Chloroform. Vortex for 1 minute. Centrifuge to separate solution. Transfer top to new microcentrifuge tube.

**Ethanol Precipitation of DNA**

To DNA solution prepared above add 10% by volume Na-Acetate buffer. Then add 3x this volume ice cold 100% Ethanol. Place the sample in the freezer for 20 min to allow DNA precipitate to form. Centrifuge max power for 10-20 minutes in the table-top centrifuge. Remove the supernate. Dry the sample COMPLETELY in air/vacuum (20 min-overnight). Resuspend in 20 $\mu$l $H_2O$ or TE buffer (use 100 $\mu$l if purifying for electrophoresis). DNA concentration is measured at 260 nm 1. OD=50 $\mu$g/ml. Pure DNA has $\text{Absorption}^{260}/\text{Absorption}^{280} > 1.8$.

### A.3.1 Agarose Gel Electrophoresis

**Solutions:**

6x Loading Buffer: 0.25% bromophenol blue and 40% (w/v) sucrose in water.

TAE Buffer (50x): 242 g Tris Base, 57.1 ml glacial acetic acid, 100 ml 0.5 M EDTA (pH 8.0)

**Procedure:**

Cautions: Phenol, Chloroform and Ethidium bromide are toxic! Work in the hood, wearing gloves. Dispose of waste in proper bins.

1. Prepare 1 L $H_2O$ + 20 ml/L TAE buffer solution (1x).

2. Dissolve 1.0 g Agarose (SeaKem LE, Cambrex) and 3 $\mu$l Ethidium bromide in 100 ml of solution prepared above by heating.

3. Tape sides of plastic gel holder so that liquid doesn't leak out, and insert comb.

4. Cool solution and pour into plastic gel holder. When gel is solid remove tape and comb. Put gel with holder into electrophoresis machine and fill with the rest of the buffer solution.

5. Phenol-Chloroform extract and ethanol purify DNA from 100 $\mu$l of fd at 3 mg/ml

(about 10 $\mu$g DNA per lane). Use DNA ladder (BstEII, New England Biolabs) for comparison. Add 4 $\mu$l 6x loading buffer to 20 $\mu$L aliquot of DNA solution.

6. Run for 0.5 h or longer (for better resolution) at 120 V.

7. After electrophoresis is complete, take pictures of DNA bands under UV light.

## A.4 Preparation of Virus Samples for Fluorescent and Electron Microscopy

### A.4.1 Fluorescent Labeling of Virus Coat Proteins

**Solutions:**

Phosphate buffer ($NaH_2PO_4$): 20 mM $p$H = 8.0.

**Procedure:**

1. Dissolve 1 mg Alexa 488 dye in 100 $\mu$l DMSO, and make 10 aliquots of solution, 10 $\mu$l each at 10 mg/ml.

2. Dialize virus against phosphate buffer $p$H 8.0.

3. Use each aliquot of dye (0.1 mg) to label 0.1 mg virus, so that there're about 10 dye molecules per binding site. The final volume needs to be 10 times the volume of DMSO used. (e.g. use 100 $\mu$l of virus at 1 mg/ml)

4. mix virus with dye/DMSO for approximately 1 hour at room temperature.

5. After reaction is complete, dialysis against 1 L phosphate buffer and 3 times centrifugation are sufficient to remove the excess dye in soluion.

### A.4.2 Oxygen Scavenging

**100× stock solution:**

- Glucose: 300 mg/ml in $ddH_2O$ ($\sim$2.25M)

- Glucose Oxidase: 20 mg/ml (Sigma G-2133)

- Catalase: 3.5 mg/ml (Sigma C-40)

- 2-Mercaptoethanol: 50% (∼7.15 M; dilute from stock) toxic! or DTT: 0.5 M (dilute from 1 M stock)

- Phosphate buffer: 20 mM, *p*H 7.5

The glucose, glucose oxidase, and catalase are made up in phosphate buffer, frozen in 20 $\mu$l aliquots in liquid nitrogen and stored at -80C.

**Using OS Mix**

1. Thaw 100× stocks of glucose, glucose oxidase and catalase with your hands, and store on ice. Prepare a 50% (v/v) 2-mercaptoethanol or DTT stock solution on ice.

2. Make a 10× OS Mix on ice.

- 10 $\mu$l of glucose, glucose oxidase, and catalase and 2-mercaptoethanol or DTT

- 60 $\mu$l phosphate buffer

Mix all the components (add glucose last), and store the 10× OS Mix in a sealed tube on ice. Prepare a fresh 10× stock after 2-3 hours for optimal results. Add 1/9 volume of the 10× OS Mix to the sample solution prior to observation.

### A.4.3 Sample Prep for TEM

1. Prepare in advance carbon-coated copper grids following the protocol developed by Dr. Chen Xu (EM lab manager) and store at 4C. Each prep yields 100 $\sim$ 200 C-coated grids, which could last for more than a year if properly stored. If the grids are too old, the carbon film can become brittle and easily peel off from the substrate under the beam. Then fresh C-coated grids need to be made.

2. Use oxygen plasma to clean and render the grids hydrophilic. Current: 20 mA. Time: 45 seconds.

3. Make proper dilutions of samples. 1/10× for 1% micron-sized bead, and 1/100× for 1 mg/ml fd virus.

4. Load the sample onto the grid. Wait 10 seconds. During this time I usually prepare drops of staining and washing solution on a sheet of parafilm.

5. Wash with milliQ water or phosphage buffer twice, and then stain with 2% Uranyl acetate **ONCE**. Overstaining will result in inhomogeneous stain on virus and aggregated chunks of UA on grids.

6. Wait until the grid totally dries before feeding it into EM for observation.

The carbon films serve as electron-transparent substrate, which provide support for samples on the open spaces of grids. The heavy metal stain of UA covers the grid surface, but is excluded from the biological materials due to surface tension, which allows the beam to pass through and thus makes the specimen appear lighter. The stain penetration of open irregularities in the particle surface further increases the contrast between the specimen and the background.

### A.4.4 Dialysis of Virus

1. Prepare buffer to dialyze virus against. Example: To make a 1.01 M Tris-NaCl buffer:

Add 1 M NaCl and 20 mL of 1 M Trisma to 950 ml $H_20$ and stir until dissolved. Adjust pH to 8.15 with 1 N HCl. Ionic strength is 1.01 M (1 M from NaCl and 10 mM from 20 mM Tris).

2. Using snake skin 10000 MWCO (from Pierce), fill about 4 inches of snake skin with virus solution which is in the isotropic phase. Make sure bottom is closed with dialysis clip. Leaving room at top of snake skin for air ($\sim$1/2 inch), close snake skin.

3. Put dialysis bag in 300-500 ml buffer and stir for at least 3 hours. Pour off buffer and fill beaker with fresh buffer. Repeat two or three times, until dialysis is

completed.

### A.4.5 Coating Virus with Amine-binding PEG

**Solutions:**

Phosphate buffer: 100 mM NaCl,100 mM $Na_2HPO_4$(Sodium Phosphate, Di-Basic) at pH 7.8 (adjust pH with HCL)

**Procedure:**

1. Dialyze virus in Phosphate buffer. Do not use Tris buffer as it contains reactive amines.

2. add Polymer: 5,000 MW, SSA-PEG-5000, or 20,000 MW, SSA-PEG-20000 (stored in freezer, highly reactive with $H_2O$). Use an amount of PEG equal to approximately 2 polymers/ binding site ($\sim$ 2 mg-peg/mg-fd for 5K PEG and 8 mg-peg/mg-fd for 20K PEG )($\sim$3000 sites/fd). Add polymer quickly to *fd* solution as it will quickly bond with water and NOT with the virus. Let polymer mix with virus for about 1 hour.

3. While virus and PEG are reacting unused PEG should be vacuum dried. Release vacuum by filling chamber with Argon gas. Seal PEG container while it is submerged in the Argon gas, seal container with parafilm and dessicate in freezer.

4. Centrifuge virus+ polymer mixture twice at 55,000 rpm (300,000 g). Beware that resulting pellet will be very soft if polymer is attached because the polymer prevents tight pelleting.

# Bibliography


[1] P. M. Adriani and A. P. Gast. Electric-field-induced aggregation in dilute colloidal suspensions. *Faraday Discuss. Chem. Soc.*, 90:17–29, 1990.

[2] A. M. Alsayed, Z. Dogic, and A. G. Yodh. Melting of lamellar phases in temperature sensitive colloid-polymer suspensions. *Phys. Rev. Lett.*, 93(5):057801, 2004.

[3] S. Asakura and F. Oosawa. Interaction between particles suspended in solutions of macromolecules. *J. Polym. Sci.*, 33(126):183, 1958.

[4] A. Ashkin. Acceleration and trapping of particles by radiation pressure. *Phys. Rev. Lett.*, 24:156, 1970.

[5] A. Ashkin. Forces of a single-beam gradient laser trap on a dielectric sphere in the ray optics regime. *Biophys. J.*, 61:569, 1992.

[6] M. Ballauff and O. Borisov. Polyelectrolyte brushes. *Curr. Opin. Colloid Interface Sci.*, 11(6):316, DEC 2006.

[7] L. B. Bangs. Uniform latex particles. *Seragen Diagnostic Inc., Indianapolis, IN*, 1984.

[8] H. A. Barnes. Thixotropy - A review. *J. Non-Newtonian Fluid Mech.*, 70(1-2):1, 1997.

[9] J. B. Berne and R. Pecora. *Dynamic Light Scattering.* Wiley, New York, 1976.

[10] P. G. Bolhuis, A. Stroobants, D. Frenkel, and H. N. W. Lekkerkerker. Numerical study of the phase behavior of rodlike colloids with attractive interactions. *J. Chem. Phys.*, 107(5):1551, 1997.

[11] M. Born and E. Wolf. *Principles of Optics: Electromagnetic Theory of Propagation, Interference and Diffraction of Light.* Cambridge University Press, Cambridge, 6 edition, 1997.

[12] J. Buitenhuis, L. N. Donselaar, P. A. Buining, A. Stroobants, and H. N. W. Lekkerkerker. Phase-separation of mixtures of colloidal boehmite rods and flexible polymer. *J. Colloid Interface Sci.*, 175(1):46, 1995.

[13] J. C. Crocker and D. G. Grier. Methods of digital video microscopy for colloid studies. *J. Colloid Interface Sci.*, 179:298, 1996.

[14] J. C. Crocker, J. A. Matteo, A. D. Dinsmore, and A. G. Yodh. Entropic attraction and repulsion in binary colloids probed with a line optical tweezer. *Phys. Rev. Lett.*, 82:4352, 1999.

[15] P. Davidson and J. C. P. Gabriel. Mineral liquid crystals. *Curr. Opin. Colloid Interface Sci.*, 9(6):377, 2005.

[16] P. G. de Gennes. *Scaling Concepts In Polymer Physics*. Cornell University Press, Ithaca, New York, 1979.

[17] Z. Dogic and S. Fraden. Development of model colloidal liquid crystals and the kinetics of the isotropic-smectic transition. *Philos. Trans. R. Soc. London, Ser. A*, 359(1782):997, 2001.

[18] Z. Dogic and S. Fraden. Ordered phases of filamentous viruses. *Curr. Opin. Colloid Interface Sci.*, 11(1):47, APR 2006.

[19] Z. Dogic, K. Purdy, E. Grelet, M. Adams, and S. Fraden. Isotropic-nematic phase transition in suspensions of filamentous virus and the neutral polymer Dextran. *Phys. Rev. E*, 69(5, Part 1), 2004.

[20] G. Dominguez-Espinosa et al. Optical tweezers to measure the interaction between poly(acrylic acid) brushes. *Polymer*, 49(22):4802, OCT 17 2008.

[21] D. Duchs and D. Sullivan. Entropy-induced smectic phases in rod-coil copolymers. *J. Phys.-Condensed Matter*, 14(46):12189, NOV 25 2002.

[22] A. M. Ferrenberg and R. H. Swendsen. Optimized monte-carlo data-analysis. *Phys. Rev. Lett.*, 63(12):1195, SEP 18 1989.

[23] J. D. Ferry. *Viscoelastic Properties of Polymers*. Wiley, New York, 3 edition, 1980.

[24] P. J. Flory. Phase equilibria in solutions of rod-like particles. *Proc. R. Soc. London Ser. A*, 234(1196):73, 1956.

[25] S. Fraden. in *Observation, Prediction, and Simulation of Phase Transitions in Complex Fluids*. edited by M. Baus, L.F. Rull, and J.P. Ryckaert. Kluwer Academic, Dordrecht, 1995. pp. 113-164.

[26] S. Fraden, A. J. Hurd, and R. B. Meyer. Electric-field-induced association of colloidal particles. *Phys. Rev. Lett.*, 63:2373–2376, 1989.

[27] S. Fujishige, K. Kubota, and I. Ando. Phase-transition of aqueous-solutions of poly(n-isopropylacrylamide) and poly(n-isopropylmethacrylamide). *J. Phys. Chem.*, 93(8):3311, 1989.

[28] S. C. Glotzer and M. J. Solomon. Anisotropy of building blocks and their assembly into complex structures. *Nature Materials*, 6(8):557, AUG 2007.

[29] J. P. Gordon. Radiation forces and momenta in dielectric media. *Phys. Rev. A*, 8:14, 1973.

[30] N. M. Green. Avidin and streptavidin. *Methods Enzymol.*, 184:51, 1990.

[31] E. Grelet and S. Fraden. What is the origin of chirality in the cholesteric phase of virus suspensions? *Phys. Rev. Lett.*, 90(19):198302, 2003.

[32] E. Hecht and A. Zajac. *Optics*. Addison-Wesley Publishing Inc., Reading, MA, 2 edition, 1987.

[33] E. K. Hobbie and D. J. Fry. Rheology of concentrated carbon nanotube suspensions. *J. Chem. Phys.*, 126(12), 2007.

[34] M. A. Horsch, Z. Zhang, and S. C. Glotzer. Simulation studies of self-assembly of end-tethered nanorods in solution and role of rod aspect ratio and tether length. *J. Chem. Phys.*, 125(18), NOV 14 2006.

[35] Y. Hu, J. Glass, A.E.Griffith, and S. Fraden. Observation and simulation of electrohydrodynamics instabilities in aqueous colloidal suspensions. *J. Chem. Phys.*, 100:4674–4682, 1994.

[36] J. N. Israelachvili. *Intermolecular and surface forces*. Academic Press, New York, 1992.

[37] T. Jones and R. Miller. Multipolar interactions of dielectric spheres. *J. Electrostatics*, 22:231–244, 1989.

[38] P. C. Jordan. Association phenomena in a ferromagnetic colloid. *Molec. Phys.*, 25:961, 1973.

[39] A. Jusufi, C. N. Likos, and M. Ballauff. Counterion distributions and effective interactions of spherical polyelectrolyte brushes. *Colloid Polym. Sci.*, 282(8):910, JUN 2004.

[40] A. Jusufi, C. N. Likos, and H. Löwen. Counterion-induced entropic interactions in solutions of strongly stretched, osmotic polyelectrolyte stars. *J. Chem. Phys.*, 116(24):11011, JUN 22 2002.

[41] K. Kegler, M. Salomo, and F. Kremer. Forces of interaction between DNA-grafted colloids: An optical tweezer measurement. *Phys. Rev. Lett.*, 98:058304, 2007.

[42] M. Kerker. *The scattering of light and other electromagnetic radiation*. Academic, New York, 1969.

[43] A. S. Khalil, J. M. Ferrer, R. R. Brau, S. T. Kottmann, C. J. Noren, M. J. Lang, and A. M. Belcher. Single M13 bacteriophage tethering and stretching. *Proc. Natl. Acad. Sci.*, 104(12):4892, 2007.

[44] K. Kubota, S. Fujishige, and I. Ando. Solution properties of poly(n-isopropylacrylamide) in water. *Polym. J.*, 22(1):15, 1990.

[45] S. Kumar et al. The weighted histogram analysis method for free-energy calculations on biomolecules .1. the method. *J. Comput. Chem.*, 13(8):1011, OCT 1992.

[46] H. M. Laun. Description of nonlinear shear behavior of a low-density polyethylene melt by means of an experimentally determined strain dependent memory function. *Rheol. Acta*, 17(1):1, 1978.

[47] H. N. W. Lekkerkerker and A. Stroobants. Phase-behavior of rod-like colloid plus flexible polymer mixtures. *Nuovo Cimento D*, 16(8):949, 1994.

[48] C. N. Likos. Effective interactions in soft condensed matter physics. *Phys. Rep.* , 348(4-5), JUL 2001.

[49] K.-H. Lim and E. I. Franses. Electrical properties of aqueous dispersions of polymer microspheres. *J. Colloid Interface Sci.*, 201:1986, 110.

[50] K. H. Lin, J. C. Crocker, A. C. Zeri, and A. G. Yodh. Colloidal interactions in suspensions of rods. *Phys. Rev. Lett.*, 87:088301, 2001.

[51] S. K. M. Adams, Z. Dogic and S. Fraden. Entropically driven microphase transitions in mixtures of colloidal rods and spheres. *Nature*, 393(6683):349, MAY 28 1998.

[52] T. Maniatis, J. Sambrook, and E. F. Fritsch. *Molecular Cloning: A Laboratory Manual*. Cold Spring Harbor Laboratory Press, Plainview, NY, 2 edition, 1989.

[53] C. B. Mao, D. J. Solis, B. D. Reiss, S. T. Kottmann, R. Y. Sweeney, A. Hayhurst, G. Georgiou, B. Iverson, and A. M. Belcher. Virus-based toolkit for the directed synthesis of magnetic and semiconducting nanowires. *Science*, 303:213, 2004.

[54] M. Mazars, D. Levesque, and J. J. Weis. Monte Carlo study of a semiflexible liquid crystal model: The smectic phase. *J. Chem. Phys.*, 106(14):6107, APR 8 1997.

[55] W. G. Miller, C. C. Wu, E. L. Wee, G. L. Santee, J. H. Rai, and K. G. Goebel. Thermodynamics and dynamics of polypeptide liquid-crystals. *Pure Appl. Chem.*, 38(1-2):37, 1974.

[56] C. A. Mitchell, J. L. Bahr, S. Arepalli, J. M. Tour, and R. Krishnamoorti. Dispersion of functionalized carbon nanotubes in polystyrene. *Macromolecules*, 35(23):8825, 2002.

[57] C. A. Mitchell and R. Krishnamoorti. Dispersion of single-walled carbon nanotubes in poly(epsilon-caprolactone). *Macromolecules*, 40(5):1538, 2007.

[58] K. C. Neuman and S. M. Block. Optical trapping. *Rev. Sci. Instrum.*, 75:2787, 2004.

[59] New England Biolabs, Ipswich, MA. *Ph.D.-C7C™ Phage Display Peptide Library Kit Instruction Manual*, 2000.

[60] K. Nicklas, P. Bopp, and J. Brickmann. Computer-simulation studies of a model system for liquid-crystals consisting of semiflexible molecules. *J. Chem. Phys.*, 101(4):3157, AUG 15 1994.

[61] L. Onsager. The effects of shape on the interaction of colloidal particles. *Ann. N.Y. Acad. Sci*, 51:627, 1949.

[62] P. Pincus. Colloid stabilization with grafted polyelectrolytes. *Macromolecules*, 24(10):2912, MAY 13 1991.

[63] H. A. Pohl. *Dielectrophoresis*. Cambridge University Press, London, 1978.

[64] K. R. Purdy. *Ph.D. thesis*. Brandeis University, MA, 2004.

[65] G. Roosen and C. Imbert. Optical levitation by means of 2 horizontal laser beamstheoretical and experimental study. *Phys. Lett.*, 59A:6, 1976.

[66] B. Roux. The calculation of the potential of mean force using computer-simulations. *Comput. Phys. Commun.*, 91(1-3):275, SEP 1995.

[67] W. B. Russel, D. A. Saville, and W. R. Schowalter. *Colloidal Dispersions*. Cambridge University Press, Cambridge, 1989.

[68] V. A. P. S. L. Brenner. Physical method for deriving electrostatic interaction between rod-like polyions at all mutual angles. *Biophys. J.*, 14:327, 1974.

[69] F. A. Sauer. *Interactions between electromagnetic fields and cells*. Plenum Press, New York, 1985.

[70] H. G. Schild. Poly (n-isopropylacrylamide) - experiment, theory and application. *Prog. Polym. Sci.*, 17(2):163, 1992.

[71] F. G. Schmidt, B. Hinner, E. Sackmann, and J. X. Tang. Viscoelastic properties of semiflexible filamentous bacteriophage fd. *Phys. Rev. E*, 62(4, Part B):5509, 2000.

[72] S. Selimovic, S. M. Maynard, and Y. Hu. Aging effects of precipitated silica in poly(dimethylsiloxane). *J. Rheol.*, 51(3):325, 2007.

[73] A. N. Semenov and A. R. Khokhlov. Statistical physics of liquid-crystalline polymers. *Sov. Phys. Usp.*, 31(3):988, 1988.

[74] Z. P. Shulman, R. G. Gorodkin, E. V. Korobko, and V. K. Gleb. *J. Non-Newtonian Fluid Mech.*, 8:29, 1981.

[75] L. Song et al. Dynamic light-scattering from weakly bending rods - estimation of the dynamic bending rigidity of the m13 virus. *Biopolymers*, 31(5):547, APR 1991.

[76] A. Stroobants, H. N. W. Lekkerkerker, and T. Odijk. Effect of electrostatic interaction on the liquid-crystal phase-transition in solutions of rodlike polyelectrolytes. *Macromolecules*, 19(8):2232, AUG 1986.

[77] K. Svoboda and S. M. Block. Biological applications of optical forces. *Annu. Rev. Biophys. Biomol. Struct.*, 23:247, 1994.

[78] J. X. Tang and S. Fraden. Isotropic-cholesteric phase-transition in colloidal suspensions of filamentous bacteriophage-fd. *Liq. Cryst.*, 19:459, 1995.

[79] G. M. Torrie and J. P. Valleau. Non-physical sampling distributions in monte-carlo free-energy estimation - umbrella sampling. *J. Comput. Phys.*, 23:187, 1977.

[80] V. Trappe and D. A. Weitz. Scaling of the viscoelasticity of weakly attractive particles. *Phys. Rev. Lett.*, 85(2):449, 2000.

[81] M. P. B. van Bruggen and H. N. W. Lekkerkerker. Tunable attractions directing nonequilibrium states in dispersions of hard rods. *Macromolecules*, 33(15):5532, 2000.

[82] S. Varga and S. Fraden. Smectic ordering in athermal systems of rodlike triblock copolymers. *J. Chem. Phys.*, 127(15), OCT 21 2007.

[83] E. J. W. Verwey and J. T. G. Overbeek. Theory of the stability of lyophobic colloids. *Elsevier Publishing Co.*, 1948.

[84] P. B. Warren. Depletion effect in a model lyotropic liquid crystal-theory. *J. Phys. I*, 4(2):237, 1994.

[85] Q. Wen and J. X. Tang. Temperature effects on threshold counterion concentration to induce aggregation of fd virus. *Phys. Rev. Lett.*, 97(4):048101, 2006.

[86] H. H. Winter and F. Chambon. Analysis of linear viscoelasticity of a cross-linking polymer at the gel point. *J. Rheol.*, 30(2):367, 1986.

[87] Y. J. Zhang, S. Furyk, D. E. Bergbreiter, and P. S. Cremer. Specific ion effects on the water solubility of macromolecules: PNIPAM and the Hofmeister series. *J. Am. Chem. Soc.*, 127(41):14505, 2005.

[88] Z. Zhang, N. Krishna, M. P. Lettinga, J. Vermant, and E. Grelet. to be published in Langmuir.